

**DEVELOPMENT OF BIOMASS-DERIVED CELLULOSE FOR
PHOTOCATALYSIS APPLICATION**

TEH ZHI SHENG

**A project report submitted in partial fulfilment of the
requirements for the award of Bachelor of Engineering
(Honours) Chemical Engineering**

**Lee Kong Chian Faculty of Engineering and Science
Universiti Tunku Abdul Rahman**

May 2022

DECLARATION

I hereby declare that this project report is based on my original work except for citations and quotations which have been duly acknowledged. I also declare that it has not been previously and concurrently submitted for any other degree or award at UTAR or other institutions.

Signature :



Name : Teh Zhi Sheng

ID No. : 1802612

Date : 13 May 2022

The copyright of this report belongs to the author under the terms of the copyright Act 1987 as qualified by Intellectual Property Policy of Universiti Tunku Abdul Rahman. Due acknowledgement shall always be made of the use of any material contained in, or derived from, this report.

© 2022, Teh Zhi Sheng. All right reserved.

ACKNOWLEDGEMENTS

I would like to thank everyone who had provided assistance and support to me throughout my final year project. Most importantly, I would like to express my sincere gratitude to my supervisor, Dr Pang Yean Ling for her care, guidance, advice and patience throughout the project in this one-year time.

Next, I would also like to express my gratitude to my beloved family who had given me strength and encouragement throughout the project. Lastly, I would also like to thank my fellow friends for their advice and aids in completing the project.

ABSTRACT

Biomass-derived cellulose is the most abundant renewable polymer on earth. Cellulose is also increasingly being researched in wastewater treatment due to its outstanding structural features, wide availability, non-toxicity and biodegradability. In usual wastewater treatments, pollutants such as phenolic compounds, organic dyes and heavy metals cannot be treated effectively. Hence, cellulose-derived composites are gaining attention in photocatalytic degradation of these pollutants. In this study, the recently developed cellulose-derived photocatalysts were reviewed. This study was conducted in four steps: i) planning; ii) searching; iii) screening; iv) reporting. The characteristics and properties of cellulose-derived photocatalysts were studied using scanning electron microscopy (SEM), field emission scanning electron microscopy (FESEM), Fourier transform infrared (FTIR) spectroscopy, X-ray photoelectron spectroscopy (XPS), X-ray diffraction (XRD) and thermogravimetric analysis (TGA). This study also reviewed the parameters affecting the photocatalytic performances such as amount of cellulose and semiconductor in composite materials, dosage of cellulose-derived photocatalysts, initial pollutant concentration and solution pH. The mechanisms of photodegradations were also studied. The characterisation results revealed that cellulose-derived photocatalysts such as cellulose-acetate-supported titanium dioxide (TiO_2/CA) and cellulose-supported cerium oxide (cellulose/ CeO_2) possessed high surface area with well-dispersed semiconductors. The cellulose-derived photocatalysts also possessed a wide variety of functional groups and types of bonds, different chemical states and crystallinities. Besides, the cellulose-derived photocatalysts had high thermal stability and the thermal decomposing started above $100\text{ }^\circ\text{C}$, which was much higher than the photocatalysis temperature. The cellulose-derived photocatalytic activities were enhanced when the ratio of cellulose-derived materials in composites, ratio of metal oxides in composites, dosage of cellulose-derived photocatalysts and solution pH were at optimum values and initial pollutant concentrations were at low values. The cellulose-derived photocatalysis experimental data also fitted the pseudo-first order (PFO) kinetic model well. Methylene blue (MB), rhodamine B (RhB) and bisphenol A (BPA)

were degraded similarly through the attack of hydroxyl radicals (OH^*) and superoxide anions ($\text{O}_2^{\cdot -}$). Meanwhile, nitrophenol was photocatalytic degraded by photo-generated electrons with the addition of sodium borohydride (NaBH_4). Hexavalent chromium (Cr (VI)) was reduced by hydrogen ions (H^+) in acidic solutions. Most of the studied cellulose-derived photocatalysts had very high efficiency in degrading phenolic compounds, organic dyes and heavy metals. Hence, cellulose-derived composites had been proven to be promising photocatalysts for the removal of water pollutants.

TABLE OF CONTENTS

DECLARATION		i
APPROVAL FOR SUBMISSION		ii
ACKNOWLEDGEMENTS		iv
ABSTRACT		v
TABLE OF CONTENTS		vii
LIST OF TABLES		x
LIST OF FIGURES		xi
LIST OF SYMBOLS / ABBREVIATIONS		xiii
CHAPTER		
1	INTRODUCTION	1
1.1	Water Pollution	1
1.2	Water Pollution in Malaysia	2
1.3	Water Pollution Effects	3
1.4	Problem Statement	4
1.5	Research Objectives	5
1.6	Scope and Limitation of Study	5
2	LITERATURE REVIEW	7
2.1	Lignocellulosic Biomass	7
2.1.1	Cellulose	10
2.1.2	Hemicellulose	12
2.1.3	Lignin	13
2.2	Pre-treatment of Lignocellulosic Biomass	15
2.2.1	Physical	15
2.2.2	Chemical	16
2.2.3	Physiochemical	17
2.2.4	Biological	18
2.2.5	Advanced Technique	19
2.3	Extraction of Cellulose	20
2.3.1	Acid Hydrolysis	20
2.3.2	Ionic Liquid	24

2.4	Cellulose-Derived Catalysts	24
2.4.1	Metal Oxides/Cellulose	26
2.4.2	Carbon Materials/Cellulose	30
2.5	Photocatalysis	37
2.5.1	Principles	38
2.5.2	Mechanisms	40
2.6	Photocatalytic Degradation of Pollutants	41
2.6.1	Phenolic Compounds	42
2.6.2	Organic Dyes	45
2.6.3	Heavy Metals	49
3	METHODOLOGY AND WORK PLAN	52
3.1	Systematic Literature Review	52
3.2	Planning	52
3.3	Searching	53
3.4	Screening and Reporting	54
4	RESULTS AND DISCUSSION	55
4.1	Characterisation of Cellulose-derived Photocatalysts	55
4.1.1	Surface Morphology	55
4.1.2	Functional Group Analysis	58
4.1.3	Chemical State Analysis	64
4.1.4	Crystallinity Properties	68
4.1.5	Thermal Stability	69
4.2	Parameters Affecting the Photocatalytic Activities of Cellulose-derived Photocatalysts	72
4.2.1	Amount of Cellulose and Semiconductor in Composite Materials	72
4.2.2	Dosage of Cellulose-derived Photocatalysts	74
4.2.3	Initial Pollutant Concentration	75
4.2.4	Solution pH	76
4.2.5	Photocatalysis Kinetics	77
4.3	Mechanisms	82
5	CONCLUSIONS AND RECOMMENDATIONS	88
5.1	Conclusions	88

5.2	Recommendations for Future Work	89
	REFERENCES	91

LIST OF TABLES

Table 2.1:	Compositions of Lignocellulose in Plant Biomass.	8
Table 2.2:	Types of Monosaccharide in Hemicellulose.	12
Table 2.3:	Cellulose Extraction Utilising Acid Hydrolysis.	22
Table 2.4:	Cellulose Extraction Utilising Ionic Liquid.	25
Table 2.5:	Summary of Recently Developed Cellulose-Derived Metal Oxide Catalysts.	27
Table 2.6:	Summary of Recently Developed Cellulose-Derived Carbon Material Catalysts.	31
Table 2.7:	Recent Studies on Cellulose-Derived Photocatalytic Degradation of Phenols.	43
Table 2.8:	Recent Studies in Cellulose-Derived Photocatalytic Degradation of Organic Dyes.	46
Table 2.9:	Recent Studies on Cellulose-Derived Photocatalytic Degradation of Heavy Metal.	50
Table 4.1:	FTIR Spectra of Cellulose-Derived Photocatalysts.	59
Table 4.2:	XPS of Cellulose-derived Photocatalysts.	65
Table 4.3:	Oxidation States of Elements in Cellulose-derived Photocatalyst.	68
Table 4.4:	TGA and DTG Data for Cellulose-Derived Photocatalysts at Different Thermal Degradation Stages.	71
Table 4.5:	Kinetic Constants of Cellulose-derived Photocatalysis in Recent Studies.	79

LIST OF FIGURES

Figure 1.1:	Ways of Water from Different Sectors Returning to the Environment (UNESCO, 2017).	2
Figure 1.2:	Rivers' Water Quality in Malaysia from 2012 to 2017 (DOE, 2017).	3
Figure 2.1:	Crystalline and Amorphous Regions of Microfibrils (Borjesson and Westman, 2015).	10
Figure 2.2:	Atomic Force Microscopy Images of (a) NCC (b) NFC (Omran, et al., 2021).	12
Figure 2.3:	Hemicellulose Surrounding Cellulose Fibre (Gatenholm and Tenkanen, 2003).	13
Figure 2.4:	Structure of a Lignin (Glazer and Nikaido, 1995).	14
Figure 2.5:	Monomers of Lignin (Ashter, 2018).	14
Figure 2.6:	Band Gap Energy of Various Semiconductors (Saravanan, Francisco and Stephen, 2017).	38
Figure 2.7:	Photocatalysis and Redox Reaction (Zhang, et al., 2019).	39
Figure 2.8:	Band Gap Energy of Materials (Tanaka, et al., 2017).	40
Figure 4.1:	(a) SEM Micrograph of ZnS-NSDC (Al-Kahtani, et al., 2019), (b) FESEM Micrograph of Nanoflake Shaped TiO ₂ /CA Nanocomposite (Nair, et al., 2021) (c) SEM Micrograph of Cellulose/CeO ₂ Nanocomposite (Zhang, et al., 2017).	56
Figure 4.2:	SEM Micrographs of (a) BiOBr/RC (Li, et al., 2016) (b) NiMn ₂ O ₄ /CCF (Zhang, et al., 2017), (c) CuO@CS (Nagarajan and Venkatanarasimhan, 2019).	56
Figure 4.3:	SEM Micrographs of (a) Graphene, (b) Ag ₃ PO ₄ and (c) Ag ₃ PO ₄ /graphene (Mu, et al., 2017).	57
Figure 4.4:	Pathway of BPA Degradation by ZnS-NSDC (Al-Kahtani, et al., 2019).	84
Figure 4.5:	Degradation Mechanism of MB Using Cellulose/TiO ₂ (Morshed, et al., 2020).	86

Figure 4.6: Photocatalytic Reduction of Cr (VI) to Cr (III) using
CNF/ZnIn₂S₄ (Qiu, et al., 2019).

LIST OF SYMBOLS / ABBREVIATIONS

AC	activated carbon
Ag ₃ PO ₄	silver phosphate
Al ₂ O ₃	aluminium oxide
As (V)	pentavalent arsenic
BiOBr	bismuth oxybromide
BOD	biochemical oxygen demand
BPA	bisphenol A
C_0	initial concentration of pollutant (mg/L)
CaO	calcium oxide
CA	cellulose acetate
CMC	carboxymethyl cellulose
CB	cellulose bead
CCNF	cellulose derived carbon nanofibre
CeO ₂	cerium oxide
CFP	cellulose filter paper
CN	cellulose nanocrystal
CNF	cellulose nanofibre
CNNS	graphitic carbon nitride nanosheet
Co	cobalt
CoFe ₂ O ₄	cobalt ferrite
Cr (III)	trivalent chromium
CrO ₄ ²⁻	chromate ion
Cr(OH) ₃	chromium (III) hydroxide
Cr (VI)	hexavalent chromium
CS	cellulose sponge
C_t	concentration of pollutant at time, t (mg/L)
Cu	copper
CuO	copper (II) oxide
D	derived
DMAC	dimethyl ammonium chloride
Cr ₂ O ₇ ²⁻	dichromate ion

DOE	Department of Environment of Malaysia
DTG	Derivative thermograph
e_{cb}^-	electrons in conduction band
EDX	energy dispersive spectroscopy
Fe_2O_3	iron (III) oxide
Fe_3O_4	iron (II, III) oxide
FESEM	field emission scanning electron microscopy
FTIR	Fourier transform infrared
G	graphene
GH	graphene hydrogel
Gly	glycerol
GO	graphene oxide
H^+	hydrogen ion
HO_2^*	perhydroxyl radical
h_{vb}^+	holes in valence band
k	PFO rate constant (min^{-1})
MNP	magnetic nanoparticle
MB	methylene blue
MCC	microcrystalline cellulose
$MeImCl-XAlCl_3$	imidazolium chloroaluminate
MFC	microfibrillated cellulose
MO	methyl orange
MOF	metal organic framework
MoS_2	molybdenum disulfide
$NaBH_4$	sodium borohydride
NCC	nanocrystalline cellulose
NFC	nanofibrillated cellulose
NGC	nitrogen doped graphitic carbon
Ni	nickel
NiFe	nickel ferrite
$NiMn_2O_4$	nickel manganese oxide
NSDC	nitrogen/sulphur doped carbon
OH^-	hydroxyl ion

OH [*]	hydroxyl radical
O ₂	oxygen
O ₂ ^{·-}	superoxide anion
Pb ⁺²	lead (II) ion
PC	porous carbon
Pd	palladium
PFO	pseudo-first order
Pt	platinum
PVA	polyvinyl alcohol
R ²	coefficient of determination
rGO	reduced graphene oxide
RC	regenerated cellulose
RhB	rhodamine B
SEM	scanning electron microscopy
SnS ₂	tin sulfide
SWCNT	single walled carbon nanotubes
<i>t</i>	photodegradation time (min)
Tb ₂ CoMnO ₆	Tb ₂ CoMnO ₆ semiconductor
TGA	Thermogravimetric analysis
TiO ₂	titanium dioxide
UNESCO	United Nations' Department of Educational, Scientific and Cultural Organisation
UV	ultraviolet
H ₂ O	water
WHO	World Health Organisation
WQI	water quality index
XRD	X-ray diffraction
XPS	X-ray photoelectron spectroscopy
Zn ⁺²	zinc ion
ZnIn ₂ S ₄	zinc indium sulfide
ZnO	zinc oxide
ZnS	Zinc sulfide
ZrO ₂	zirconium dioxide

CHAPTER 1

INTRODUCTION

1.1 Water Pollution

Water is one of the basic requirements of lives and the anthropogenical water pollution has been occurring since the earliest civilisations. Till today, the access to clean fresh water is still one of the major challenges globally. According to United Nations' Department of Educational, Scientific and Cultural Organisation (UNESCO) (2017), 29 % of the global population did not have readily available and contaminant-free water in 2017. According to World Health Organisation (WHO) (2019), at least 2 billion worldwide was drinking from faeces-contaminated water sources in 2019. It was also projected that 50 % of the world's population will be living in water scarce area by 2025.

The inadequate treatment of wastewater before returning to the environment had been deteriorating the water quality in a rapid pace (Lu, Liu and Ge, 2021). The ways or final forms of water returning to the environment after a cycle of human's usages or activities around the globe is summarised in Figure 1.1. According to UNESCO (2017), the global uptake of freshwater was 3 928 km³ per year. The withdrawn water was used significantly in agriculture, domestic usages and industrial activities. Around 44 % of the water was returned to the atmosphere by evaporation in the irrigated farmlands. The other 56 % returned to the environment as various wastewater such as domestic effluent, industrial discharge and drainage from farmlands.

The major causes of water pollution around the globe were human activities such as industrial discharge, sewage discharge, agricultural waste (Lu, Liu and Ge, 2021), mining (Morodi and Mpofu, 2018), oil leakage (Keller, et al., 2018), usages of fertilisers and pesticides, landfills (Kapelewska, et al., 2019) and others. The discharge of chemicals, organics, and other pollutants from these sectors had been causing pollution and contamination of water bodies such as rivers, groundwaters, aquifers, lakes and ponds (Ivan, et al., 2021).

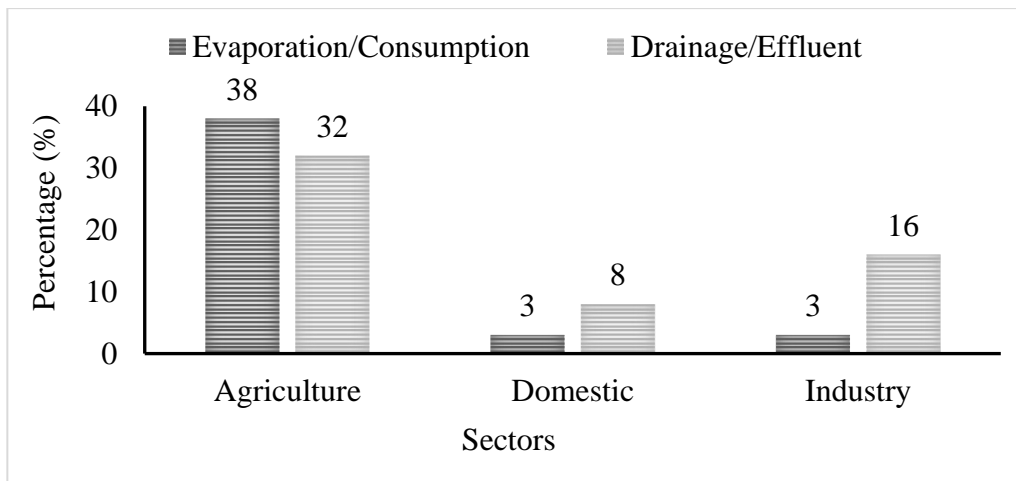


Figure 1.1: Ways of Water from Different Sectors Returning to the Environment (UNESCO, 2017).

1.2 Water Pollution in Malaysia

As a nation moving forward to the developed country goal, Malaysia's growing economy is made up of the essential sectors of heavy industries, oil and gases and small and medium enterprises. These sectors inevitably discharge various pollutants such as heavy metals, organic compounds, phosphorous, suspended solids, dyes and other compounds into the water bodies.

Department of Environment of Malaysia (DOE) (2021) reported that about 98 % of the water used in Malaysia were from rivers and they were classified based on their water qualities into five main classes of I, IIA, IIB, III, IV and V. The water classes are highly associated with the qualifying of the water's uses. For example, only Class I can be used for fisheries with very sensitive aquatic species, Class IV can be used for irrigation and Class V with the lowest quality cannot be used at all.

Based on the water quality index (WQI), the rivers of Malaysia could be categorised into "clean", "slightly polluted" and "polluted" as shown in Figure 1.2 (DOE, 2017). Clean rivers' WQI ranged from 81 to 100, slightly polluted rivers' WQI ranged from 60 to 80 and polluted rivers' WQI ranged from 0 to 59. There were 477 rivers monitored by DOE from 2012 to 2017. Over the six years, the percentage of "clean" rivers slightly dropped from 58 to 46 %, percentage of "slightly polluted" rivers increased from 34 to 43 % and "polluted" rivers slightly increased from 8 to 11 %.

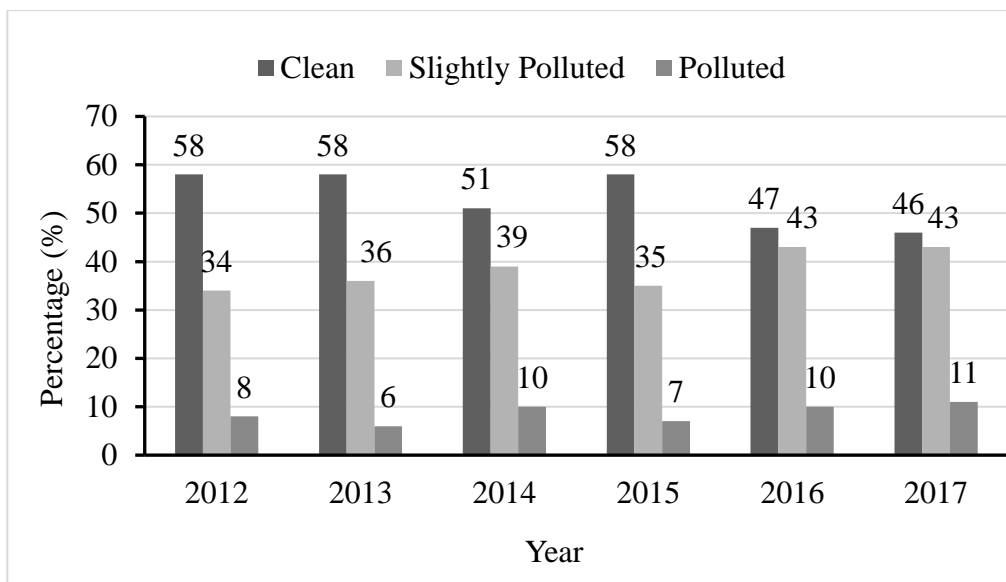


Figure 1.2: Rivers' Water Quality in Malaysia from 2012 to 2017 (DOE, 2017).

From the Environment Quality Report 2017 by DOE (2017), the three most significant water pollution parameters in Malaysian rivers were biochemical oxygen demand (BOD), ammoniacal nitrogen waste and suspended solids. Everyday of 2017, there were 545 tonnes of BOD wastes, 909 tonnes of suspended solids and 229.3 tonnes of ammoniacal nitrogen waste dumped into the rivers respectively. The five major sources for water pollution in Malaysia rivers were manufacturing industries, agricultural activities, sewage treatment plant, animal farming and wet markets (DOE, 2021).

1.3 Water Pollution Effects

It was reported that only 70 %, 38 %, 28 % and 8 % of the agricultural drainage or wastewater produced globally were given treatment of any kind in rich, middle income, lower income and poor countries respectively (UNESCO, 2017). It was estimated that more than 80 % of global wastewater was returned to the environment without sufficient treatment (UNESCO, 2017). As a result, polluted water bodies often brought worsening adverse effects to human health and the environment.

For a human, the consumption of water is inevitable as it is an essential resource for all lives on earth. According to WHO (2019), contaminated water could cause diarrhoea, cholera, dysentery, polio and other diseases. Every year, an approximate of 297 000 children under five died from diseases related to

polluted drinking water. Water polluted by organic pollutants such as dyes and fertilisers also caused hormonal disruption, altered brain functions, damage to immune and reproductive systems and kidney problems (Nair, et al., 2021). In addition, heavy metals such as aluminium, barium, copper, iron, lead, mercury, zinc and others were also found in drinking water worldwide due to inefficient water treatment. Many studies had shown that various diseases and effects such as osteomalacia, stillbirth, cancer, skin diseases, kidney failure, blood complications and others were correlated to long-term exposure to the high concentration of heavy metal drinking water (Chowdhury, et al., 2016).

For environment, acids dumped into the ocean burdened shell forming shellfish and plankton, reducing the crucial primary food source in the oceanic food chain. Biochemical oxygen demand waste also eliminated aquatic life in rivers, lakes and ponds as oxygen was used up to oxidise organic waste. Besides, plastics and spilt oil suffocated marine life. Eutrophication due to excessive nitrates and phosphate destroyed biodiversity in affected water bodies. The nutrients from farmlands drained into the water and stimulated excessive growth of algae, reducing oxygen levels in the water. This phenomenon was known as algae bloom and it often created dead zones in affected water bodies.

1.4 Problem Statement

Conventional wastewater treatments included various methods such as phase separation, sedimentation, oxidations, filtration, ultra-filtration, reverse osmosis, disinfection, coagulation/flocculation, floatation and others (Abrile, et al., 2021). In recent years, novel methods such as photocatalysis, adsorption and ozonation were being researched intensively to fill the niche of treating pollutants such as phenolic compounds, heavy metals and organic dyes which the conventional methods are unable to effectively remove (Kim, et al., 2020; Margaret, et al., 2021). Besides, some of the conventional wastewater treatments also produce secondary pollutants. The newly explored water treatment methods also had other advantages such as higher selectivity towards targeted pollutants, lower energy required, providing alternative reaction media or conditions, cheaper in overall process and more environmental-friendly.

As typical catalysts in water treatment were made up of metals or precious metals such as platinum and palladium, the catalysts were often

associated with high prices and were not environmentally friendly (Sikora, et al., 2021). For instance, rhodium's price had once increased 20 folds to 314 000 dollars per kilogram in 4.5 years (National Research Council, 2012). Some wastewater processes' commercialisations were stunted due to the infeasibility of the required catalysts in terms of prices and availability. Extra costs due to the attrition and/or deactivation of precious metals during the chemical processes must also be borne by the water treatment companies. Most of the metal catalysts being used nowadays are also not readily biodegradable. Besides, the various wastes and pollutants produced during the preparation of the catalysts are also causing harms to the environment.

In recent years, biomass had been increasingly researched, especially in the substitution of fossil fuels as awareness of global warming and the importance of sustainability raised. Cellulose, appears mainly in cell wall of plants and biofilms of bacteria, is the most abundance biopolymer on Earth. The high abundancy and thus, high affordability of cellulose is a significant advantage for it to compete with other matters in the future development of technologies. For wastewater treatment, various studies had been done by researchers on cellulose and its derivative composites in photocatalysis. The cellulose-derived photocatalysts have potential in solving water pollution problems effectively.

1.5 Research Objectives

The ultimate objective of this project is to investigate the utilisation of biomass-derived cellulose and its derivatives in photocatalysis reactions. The specific objectives of this project include the following:

1. To study the characteristic of cellulose and its derivatives composite using various physical and chemical methods
2. To review the parameters that affect the photocatalytic activity of cellulose and its derivatives composite

1.6 Scope and Limitation of Study

The starting parts of this project are related to the review of renewable resources and cellulose. Renewable resources' prospects and advantages are first studied. Among all potential renewable resources, lignocellulosic biomass is focused

due to its leading roles in sustainability development. The physical and structural properties of cellulose, hemicellulose and lignin are studied. Next, the physical, chemical, biological and other advanced techniques and methods applied across the globe in pre-treating lignocellulosic biomass are reviewed and summarised. Following that, cellulose-derived composite catalysts and photocatalysis reactions are studied and presented. The photocatalytic degradations of various types of pollutants in the presence of cellulose-derived composites are also reviewed.

The characteristics and properties of cellulose-derived photocatalysts are then reviewed and summarised. The characterisation techniques and analyses include scanning electron microscopy (SEM) and field emission scanning electron microscopy (FESEM) for surface morphology, Fourier transform infrared (FTIR) spectroscopy for functional group analysis, X-ray photoelectron spectroscopy (XPS) for chemical state analysis, X-ray diffraction (XRD) for crystallinity properties and thermogravimetric analysis (TGA) for thermal stability. Following that, the parameters that influence the photocatalytic activities of cellulose-derived photocatalysts are studied and outlined. The parameters include amount of cellulose and semiconductor in composite materials, dosage of cellulose-derived photocatalysts, initial pollutant concentration and solution pH. In addition, the photocatalysis kinetics are also studied. The suggested mechanisms involving cellulose-derived photocatalysts are summarised next.

Nevertheless, there are some limitations that must be taken into consideration throughout the study. As all the information and experimental results are retrieved from literature, some of the desired information may be unavailable and limited. Hence, some justifications and analyses will be provided.

CHAPTER 2

LITERATURE REVIEW

2.1 Lignocellulosic Biomass

Global warming, environmental pollutions, energy crisis, water insecurity, public health and other significant issues affect every human being to some extent nowadays. Most of these problems are caused by the over usage of natural resources available such as fossil fuels, lands, aquatic or terrestrial animals and plants alike. The regeneration of these valuable resources is unable to match the speed of consumption or devastation caused by humans.

As the repercussion of mother nature becomes more and more significant, renewable resources have been outstanding as solutions to the many problems and challenges faced by humanity. Renewable resources are also usually more energy cleaner in their life cycle compared to non-renewable resources. For example, the utilisation of renewable resources creates less greenhouse gases and pollutions in environment.

Lignocellulosic biomass is a great potential source of raw materials for applications in clean energy, materials, polymers, and chemicals. A study done by Elhacham, et al., (2020) showed that there were 2.2×10^{12} tonnes wet-weight basis and 1.18×10^{12} tonnes dry-weight basis of plant biomass available on earth. This huge reserve of plant biomass is readily providing a source of renewable raw materials for sustainable applications and green technologies.

The dry weight of plant biomass is known as lignocellulose. Lignocellulosic biomass consists of three main constituents, which are cellulose, lignin, and hemicellulose. Together, they make up the cell wall of most plants. The compositions of various plant biomass are summarised in Table 2.1. Besides, lignocellulosic biomass also consists of other minor constituents like wax, lipids and chlorophyll (Kalia, Kaith and Kaur, 2011). Different types of plants have different compositions of lignocellulose and a similar kind of plant also has different compositions of lignocellulose during their stages of growth (Silva, et al., 2021).

Table 2.1: Compositions of Lignocellulose in Plant Biomass.

Biomass	Cellulose (%)	Hemicellulose (%)	Lignin (%)	References
Rice hull	31.0	32.7	16.2	
Banana fibre	49.3	12.0	13.9	
Cotton	93.0	3.0	-	
Oil palm fibre	40.20	32.1	18.7	
Oil palm leaf	43.80	36.4	19.1	
Pineapple	73.40	7.1	10.5	(Arnata, et al., 2019)
Banana peel	13.2	14.8	14.0	
Corn cob	31.2	43.1	3.4	
Pine	45.3	25.1	26.4	
Wheat straw	61.8	19.0	14.1	
Tea waste	30.2	19.9	40.0	
Paper	85.0 – 99.0	-	0.0 – 15.0	
Primary wastewater solid	8.0 – 15.0	-	20.0 – 29.0	
Solid cattle manure	1.6 – 4.7	1.4 – 3.3	2.7 – 5.7	(Khalid, Ahmad and Tau,
Nut shells	25 - 30	25 - 30	30 - 40	2017)
Switchgrass	45	31.4	12	
Table Reed	30.0	23.8	26.2	
Sorghum	17.9	31.4	23.4	(Jung, Kim and Sung, 2015)
Micantus	30.5	29.9	14.7	

As different sources of lignocellulosic biomass have different compositions, a wide pool of choices of plants are available for researchers to explore for one which suits their applications. For example, researchers had done studies on various crops and found a suitable mix of green peas, soy, and wheat suitable for synthesising plant-based meat to substitute beef (Rubio, Xiang and Kaplan, 2020). 14.5 % of global greenhouse emission was from the livestock industry and 1 849.2 gallons of water were used for harvesting a pound of beef (Smith, 2021). Plant-based meat has the potential in solving the increasing global protein demand, while reducing the environmental impact of greenhouse gases emission and the large quantity of water used in cattle rearing.

As a renewable resource, the amount of desired lignocellulosic biomass can also be scaled-up and multiplied according to the needs and demand by simply growing the desired plants more. For example, palm oil had been discovered to have many health benefits compared to conventional cooking oil. Palm oil could also be used as raw material in producing many cosmetics, industrial and pharmaceutical products (Zianor Azrina, et al., 2017). In recent years, oil palm plantations had been scaled up tremendously in Southeast Asia, Latin America and Central Africa due to their high demand (Descals, et al., 2021).

Besides, biomass can be recycled and reused. For example, paper containing high percentage of cellulose was recycled to make new products such as egg cartons and newspaper (Chen, Chiu and Ma, 2016). This approach could reduce the dump in landfills and provide cheap reused raw material to the related industry at the same time. The environmental impact of producing new raw materials such as pollutants and greenhouse gases emissions could also be reduced when waste materials were being recycled and reused (Kalia, Kaith and Kaur, 2011).

On the other hand, comprehensive applications of lignocellulosic biomass can drive the economy up. The utilisation of agricultural residue like straw, stover and husks can bring extra income to farmers. Instead of disposing or burning these crops leftovers, farmers can collect and sell them as raw materials to other fields. An instance illustrating this was rice husk being combusted to ash and used as fertiliser, biochar, cement, catalyst, and adsorbent

(Hafid, et al., 2021; Moayedi, et al., 2019). Instead of being dumped, the agricultural residue can generate income and create job opportunities.

2.1.1 Cellulose

Cellulose is a biopolymer of D-glucose, $C_6H_{10}O_5$. The number of monomers for a cellulose molecule can be up to 20 000 (Hinestroza and Netravali, 2014). D-glucose is the most usual, abundant but important monosaccharide in the metabolism of animals. D-glucose appears as blood sugar and forms starch, glycogen, and other polymers.

In cellulose molecules, D-glucose monomers are first linked up by covalent β -1,4-glycosidic bond, forming straight chain elemental fibril. Elemental fibrils side up along each other and linked up by intermolecular hydrogen bonds and Van der Waals force, forming a bundle of elemental fibrils called microfibril (Kalia, Kaith and Kaur, 2011). The microfibrils are the functional units of cellulose. There are crystalline and amorphous regions along microfibrils as shown in Figure 2.1. Bundles of microfibril form macrofibre or conventionally known as cellulose fibre (Borjesson and Westman, 2015).

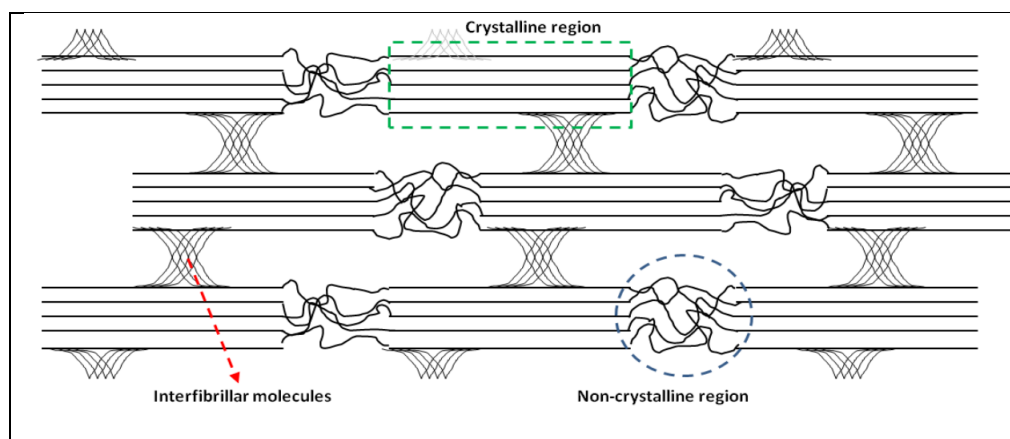


Figure 2.1: Crystalline and Amorphous Regions of Microfibrils (Borjesson and Westman, 2015).

The macrofibres are meshed into a matrix of lignin and hemicellulose. The meshing is often described as cellulose fibre acts as steels in cement of lignin and hemicellulose (Kalia, Kaith and Kaur, 2011). Layering of macrofibres in different orientations form the cell wall of plants.

The compact arrangement in cellulose with the extensive hydrogen bonding can enhance the mechanical strength and decreases its degradability. Besides, the matrix of lignin and hemicellulose surrounding cellulose makes cellulose resistant towards enzymes, acids and swelling in water as the chemicals and water are inaccessible (Hinestroza and Netravali, 2014). The amorphous region of the microfibrils is the main sites of hydrolysis for cellulose extraction after biomass pre-treatments.

Cellulose has seven allomorphs, named cellulose I_{α} , I_{β} , II, III_I , III_{II} , IV_I , and IV_{II} (Hindi, 2017). They are different in the degree of crystallinity and originate from different sources. However, they are interconvertible under certain conditions. Cellulose I_{α} is dominantly found in algae, bacteria and tunicate cellulose. In plants, cellulose I_{α} and I_{β} are present but I_{β} is more commonly found and thermodynamically more stable (Hinestroza and Netravali, 2014). In cellulose II, the cellulosic chains are not in parallel form. Hence, it is structurally stronger and is widely used in the paper industry. Moreover, cellulose III_I and III_{II} are the products of ammonia pre-treatment of cellulose I and II, respectively (Mor, et al., 2018). Lastly, cellulose IV is the irreversible product of heating cellulose III_I or III_{II} in glycerol.

Apart from the seven allomorphs, cellulose can also be broadly classified into microcrystalline cellulose (MCC), microfibrillated cellulose (MFC), cellulose nanocrystal (CNC) and nanofibrillated cellulose (NFC) (Omran, et al., 2021). However, the four main groups of cellulose have many other interchangeable names. Figure 2.2 shows the atomic force microscopy images of NCC and NFC. MCC and MFC have a size of around 10 to 50 μm in diameter while NCC and NFC have diameter size smaller than that (Abdelhamid and Mathew, 2022). MFC and NFC are obtained by mechanical size reduction of cellulose fibre into fibrous structure (Tsapekos, et al., 2017). Hence, both crystalline and amorphous regions of cellulose exist in MFC and NFC. On the other hand, MCC and NCC are obtained by hydrolysing the amorphous part of cellulose (Borjesson and Westman, 2015). As a result, only crystalline part of cellulose presents in MCC and NCC.

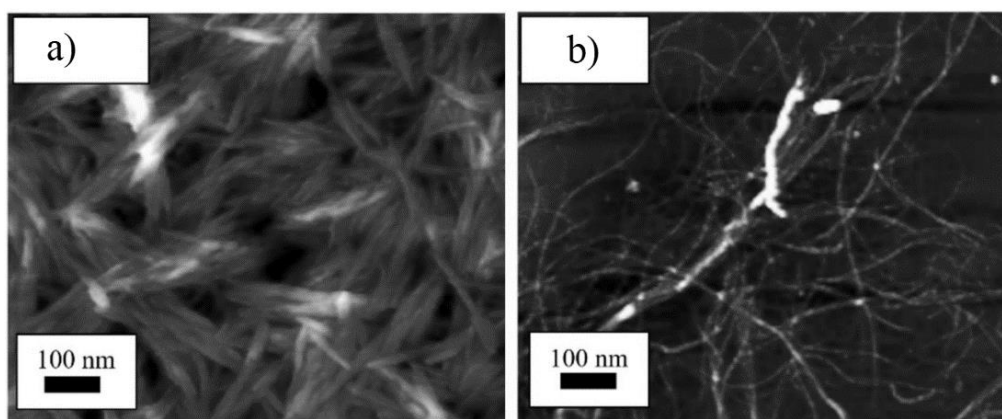


Figure 2.2: Atomic Force Microscopy Images of (a) NCC (b) NFC (Omran, et al., 2021).

2.1.2 Hemicellulose

Hemicellulose is a group of different polysaccharides unlike cellulose which is a single type of polymer of its own. Types of hemicelluloses include xylans, mannans, xyloglucans and others. Hemicellulose is the second most plentiful polymers in lignocellulosic biomass, only after cellulose. Commonly, 25 to 30 % dry weight of woods are made up of hemicellulose. Hemicelluloses are originated from the different monomers as they contain pentoses, hexoses and sugar acids. Table 2.2 summarises the common monomers appeared in hemicelluloses. Pentose and hexose are five and six-carbon sugars respectively. Sugar acids of hemicelluloses are six (galacturonic and glucuronic acids) to seven-carbon sugars (4-O-methyl-glucuronic) with hydroxyl groups. The degree of polymerisation of hemicellulose is from 80 to 3 000 (Gatenholm and Tenkanen, 2003).

Table 2.2: Types of Monosaccharide in Hemicellulose.

Types of Sugar	Monomers
Pentose	xylose, arabinose
Hexose	mannose, glucose, galactose
Sugar acid	4-O-methyl-glucuronic, galacturonic, glucuronic acids

The monomer sugars are linked up by β -1,4 and β -1,3-glycosidic bonds, forming a chain. The hemicellulose chains can be linear but mostly are branched.

Xylan is the most abundant hemicellulose in hard wood and glucomannan is the principal hemicellulose in softwood. Hemicellulose form hydrogen bonds with cellulose microfibrils, ether and ester linkages with lignin, and ester bonds with acetyl units (Ghosh, et al., 2021). Figures 2.3 shows the distribution of hemicellulose in the matrix of lignin and hemicellulose around cellulose. Apart from forming hydrogen bond with cellulose molecule, hemicellulose also surrounds the bundles of cellulose fibre spirally and the aggregation or delamination of the cellulose fibres are hindered. Hemicellulose also acts as compatibiliser between cellulose and lignin.

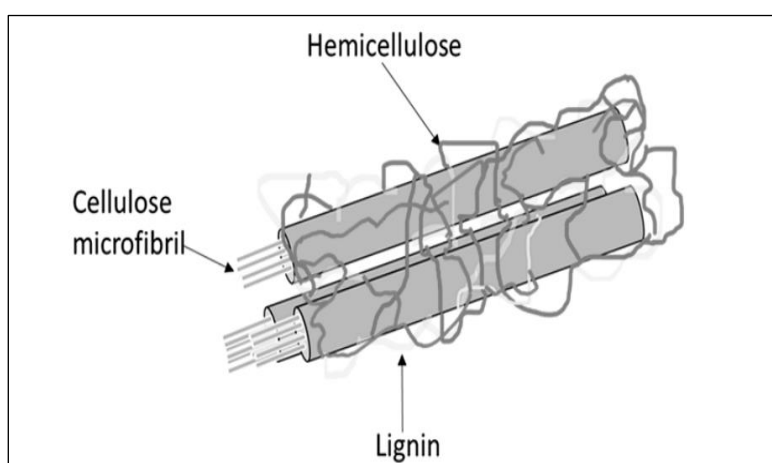


Figure 2.3: Hemicellulose Surrounding Cellulose Fibre (Gatenholm and Tenkanen, 2003).

Among cellulose, hemicellulose and lignin, hemicellulose is the easiest to be isolated and most susceptible to mechanical and chemical degradation (Joy, et al., 2015). This is due to its solubility properties in alkaline solution, low level polymerisation and amorphous structure. However, it is most resistant towards enzyme hydrolysis among the three main components of lignocellulosic biomass.

2.1.3 Lignin

Lignin is complex and amorphous due to its irregular cross linkages between monomers. Figure 2.4 shows a typical lignin structure. Its molecular weight can range from 1 000 up to 20 000 g/mol.

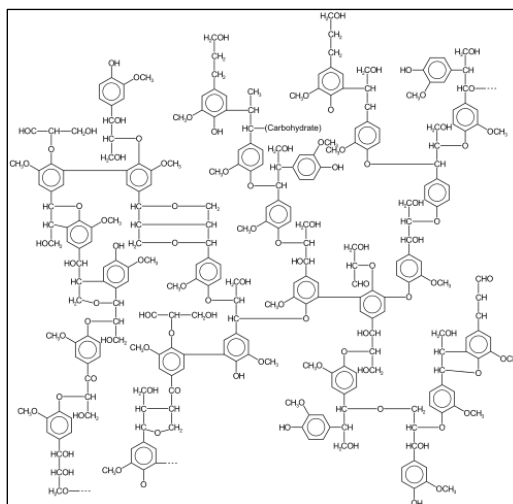


Figure 2.4: Structure of a Lignin (Glazer and Nikaido, 1995).

Lignin is a heterogenous polymer. Its three types of monomers are coumaryl alcohol, coniferyl alcohol and syringyl alcohol (Ashter, 2018). Figure 2.5 shows the formula of the three monomers. The bonds between monomers are carbon-carbon covalent bond or aryl-ether linkages (Glazer and Nikaido, 1995). Three of them are all phenols, hydrocarbons of aromatic rings with hydroxyl groups. Coniferyl alcohol is the primary monomer in softwood lignin while coumaryl and syringyl alcohols are the main constituents in hardwood lignin.

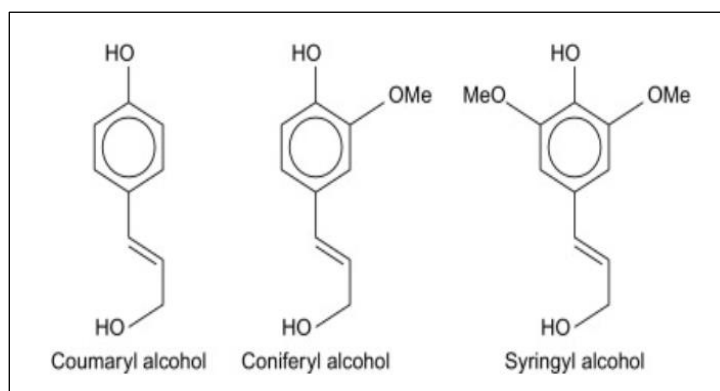


Figure 2.5: Monomers of Lignin (Ashter, 2018).

Among cellulose, hemicellulose and lignin, lignin is the most recalcitrant against degradation and hydrolysis (Silva, et al., 2021). The main role of lignin in lignocellulosic biomass is to form a matrix to accommodate cellulose fibrils. Besides, lignin's hydrophobic behaviour prevents the

penetration of solutions and enzymes into the biomass (Kumar, et al., 2021). This also contributes to the impermeability of the biomass. Its 3-dimension meshing also provide the rigidity of the plant cell wall.

2.2 Pre-treatment of Lignocellulosic Biomass

The inaccessible to the isolated cellulose, hemicellulose, and lignin components due to their meshing in a matrix becomes a challenge to utilise the biomass fully. Pre-treatments are very important for the subsequent extraction and break down of the lignocellulosic biomass. There are many ways of pre-treating the biomass and they are often used in combination to achieve the desired result. Currently, the low efficiency, high cost and energy of pre-treatments of the biomass is the main bottleneck of fully utilising the widely available and abundant lignocellulosic biomass. Various types of physical, chemical, physiochemical, biological, and advanced technique of lignocellulosic biomass pre-treatments are discussed in the following subtopics.

2.2.1 Physical

Size reduction is usually the first pre-treatment of biomass, where the biomass raw materials are mechanically cut, chipped, milled, crushed, sieved, or grinded. The macroscopic structure of lignocellulosic biomass is destroyed by applying shear or compression force (Tsapekos, et al., 2017). The final pieces or powder are of different sizes and diameters depending on the biomass. The main objective of size reduction is to increase the surface area per unit volume of the lignocellulosic biomass for higher efficiency in the proceeding treatments or reactions. Armeanue, David and Badescu (2019) grinded and sieved rapeseed oil cake, walnut shells, peanut shells, and apricot stones and conducted pyrolysis tests. They concluded that grinding and sieving pre-treatments have a positive effect on the amount of fuel gas yield from biomass.

Besides size reduction, thermal pre-treatment is also widely used in lignocellulosic biomass component extractions. Thermal pre-treatment increases the dissociation rate of bonds between the molecules in biomass. The main parameters in heat pre-treatment are the temperature and duration. In general, the higher the temperature and the longer the duration, the more effectively the thermal pre-treatment (Kargarzadeh, Ahmad and Thomas, 2017).

Besides, many other pre-treatments and extraction of biomass components are also done under elevated temperature or even high temperature to increase the effectiveness of the process (Hafid, et al., 2021; Shaikh, et al., 2021).

Both size reduction and thermal pre-treatment of biomass are highly energy intensive and usually contributes a large fraction of the pre-treatment cost (Armeanue, David and Badescu 2019; Kargarzadeh, Ahmad and Thomas, 2017). However, both pre-treatments are still being used extensively due to their effectiveness.

2.2.2 Chemical

Chemical pre-treatments is currently the most adopted method in lignocellulosic biomass component extraction. Suitable chemicals such as alkali, organic solvents and ozone are used to hydrolyse or dissolve the unwanted components in lignocellulosic biomass.

In chemical pre-treatment, the most widely used alkali is sodium hydroxide while others such as potassium hydroxide, calcium hydroxide and ammonium hydroxide are also used but in much lesser extent. The first objective of alkali pre-treatment is to cause swelling or increase surface area of cellulose fibre to make fibre more susceptible for subsequent process (Kargarzadeh, Ahmad and Thomas, 2017). Besides, alkali pre-treatments are also extensively used to remove lignin and/or hemicellulose by solubilising them, depending on the biomass and applications.

Alkali pre-treatment is usually done in conditions of temperature below 100 °C and alkali concentration below 20 wt % but long time up to a few hours or even days (Zianor Azrina, et al., 2017). Gopi, et al. (2019) and Rasheed, et al. (2020) used sodium hydroxide of 4 wt % at 80 °C for 2 hours to solubilise lignin, hemicellulose, and pectin for their alkali pre-treatments. The most significant and famous alkali pre-treatment is the Kraft process where paper and pulp are made (Joubert, Chiphango and Gorgens, 2016; Mongkhonsiri, et al., 2021). Various types of woods are boiled in sodium hydroxide for a few hours to remove lignin and hemicellulose for extraction of cellulose to make paper and pulp.

Other than alkali, organic solvents are also used in lignocellulosic pre-treatment to delignify the biomass. Organosolvation pre-treatment using organic

solution either in pure form or aqueous form, with or without inorganic acid catalysts. Various kinds of organic solvents had been used including alcohols, phenols, esters, organic acids, amines, and others (Shuai and Luterbacher, 2016). Organosolvation is usually done at above 100 °C but below 250 °C. Various advantages of using these solvents have been reported such as ease of solvent recovery, high speed and rate of delignification and higher yield of component extraction in later process (Olajuyin, et al., 2018). Methanol and ethanol are highly preferred in pre-treatment for posterior biomass fermentations due to their low boiling point and hence ease of separation (Zhang, et al., 2018). The ease of separation is crucial to prevent the inhibitory effect of the solvent on the microorganisms during fermentations.

Ozone treatment is also one of the chemical pre-treatments of lignocellulosic biomass. Its main function is to delignify the biomass specifically without disrupting the structure of cellulose and hemicellulose. Lignin's side chain and aromatic double bonds make it very susceptible for oxidation or by ozone treatment (Perrone, et al., 2021). The biomass is usually hydrated before subjecting to ozone gas flow generated from oxygen under room temperature and pressure (Li, et al., 2021). Ozone treatment also leaves no inhibitory residues as ozone decomposes under high temperature. However, ozone treatment is also expensive and has no effect in removing hemicellulose. Therefore, ozone treatments are often followed with alkaline treatment for biomass undergoing enzymatic hydrolysis (Ortega, et al., 2021).

2.2.3 Physiochemical

Exploitation of both physical and chemical treatments for removal of hemicellulose and lignin are highly used in lignocellulosic biomass pre-treatment. More modern physiochemical pre-treatments include steam explosion, ammonia fibre expansion, liquid hot water, and others.

In steam explosion, lignocellulosic biomass is subjected to elevated temperature (120 °C – 250 °C) and high pressure (up to 26.5 bar) under saturated steam (Steinbach, et al., 2019; Tupciauskas, et al., 2021). After a few minutes of retention, the sudden discharge of biomass to atmospheric environment provides the explosion effect and disrupts the biomass structure mechanically. Steam explosion is known to break down hemicellulose linkages significantly

in the biomass (Wu, et al., 2020). Acetic acid would form hemicellulose's acetyl groups and this helps in hydrolysis of the biomass too.

Ammonia fibre expansion is a pre-treatment usually used to loosen fibre and increase digestibility or fermentability of lignocellulosic biomass. It is also well known to be used to pre-treat feed for ruminant livestock like buffaloes and cattle (Mor, et al., 2018). The biomass is first subjected to steam and then soaked in liquid ammonia under elevated temperature and high pressure (Campbell, et al., 2020). Then, the biomass is gradually depressurised before stripping the leftover ammonia off by steam. Ammonia fibre expansion is known to be not efficient to separate components of lignocellulosic biomass in overall as some insoluble sugar will form from reaction between hemicellulose and ammonia (Zeng, et al., 2021).

Liquid hot water pre-treatment is used widely in lignocellulosic biomass pre-treatments to significantly remove most hemicellulose but only part of lignin (Serna-Loaiza, et al., 2021). The biomass is mixed with water and subjected to high temperature in retention. Usually, the ratio of biomass to water is 1:10, temperature ranges from 150 °C to 250 °C and the retention time is around 1 hour (Lu, et al., 2021; Yang, et al., 2021). In liquid hot water pre-treatment, there is no rapid depressurisation, but other chemical pre-treatment usually followed to remove lignin effectively (Kim, et al., 2021).

2.2.4 Biological

Biological pre-treatments utilising microorganisms such as fungi and bacteria are one of the significant and most industrialised way of treating lignocellulosic biomass. The microorganisms disrupt the lignin seal of lignocellulosic biomass with their metabolite of enzymes, allowing subsequent reaction such as digestion or fermentation to be taken place (Tsegaye, Balomajumder and Roy, 2019). Biological pre-treatments have significant advantages such as environment friendly as no chemical or solvent involved, low energy requirement and cost effective (Papoutsis and Edelenbos, 2021). However, strict reaction condition must be maintained, and the time taken for completion of the pre-treatment is relatively long.

Bacteria strains with degrading enzymes are widely used in biological pre-treatments. Often, the biomass is hydrolysed and fermented directly in

bacterial pre-treatments (Papoutsis and Edelenbos, 2021). However, most bacteria used are cellulolytic and hemicellulolytic, which have high degrading ability on cellulose and hemicellulose but not on lignin (Sharma, Xu and Qin, 2017). Bioethanol is one of the most significant biofuels produced from bacteria biological pre-treatment.

On the other hand, fungi have more significant influence in lignin removal in biological pre-treatment compared to bacteria. White, brown and soft-rot fungi are some of the commonly used fungi groups in pre-treating lignocellulosic biomass (Indira, et al., 2020). The ability of white-rot fungi is given much attention. A study showed that three types of white-rot fungi (*Phanerochaete chrysosporium*, *Lentinula edodes*, and *Trametes versicolor*) had significant degradation rates of lignin from 82 to 89 % (Hou, et al., 2020). In fact, white-rot fungi and brown-rot fungi get their names by the residues of white cellulose and brown lignin they left behind, respectively. Generally, fungi pre-treatments which takes up to weeks or months require longer time than bacteria pre-treatments which only need days or even hours.

2.2.5 Advanced Technique

One of the novel and advanced techniques used in lignocellulosic biomass pre-treatments is the ultrasound pre-treatment. Ultrasound is higher frequency sound waves which human cannot hear. It can break the lignin-hemicellulose linkages in lignocellulosic biomass and effectively remove lignin from the biomass (Zhang, et al., 2021). The biomass is immersed in water and ultrasound with frequency ranges from 20 to 42 kHz is applied for optimally 5 to 60 minutes (Pei, et al., 2021; Sharma, Nargotra and Bajaj, 2019). The temperature of ultrasound pre-treatment is at 25 °C or even lower (Kandasamy, et al., 2017). Ultrasound pre-treatment has advantages such as short reaction time, environment-friendly, easy to operate and low energy consumption.

Microwave is also one of the advanced lignocellulosic biomass pre-treatments. Its usages are mainly serving as heat treatment to directly break the biomass linkages or assist in other pre-treatments. The electromagnetic wave of microwave penetrates the surface of biomass, resulting in volumetric heat generation instead of conventional surface heating. Hence, microwave pre-treatments are considered more time and energy saving than conventional

heating in thermal treatment of lignocellulosic biomass (Yu, et al., 2020; Kol and Cayir, 2021).

Pulsed electric field pre-treatment is an electro-chemistry technique applied in lignocellulosic pre-treatment. It is widely used on biomass in the food industry. The biomass is placed between two electrodes and an alternating high voltage is ran across the biomass. Usually, table salt solution is used to immerse the biomass (Yu, Jin and Xiao, 2017). The electric field strength ranges from 0 to 5 kV cm⁻¹, with up to 8 000 pulses and the duration is within few minutes (Andreou, et al., 2020). The intense and alternating electric field damages the structure of the biomass cell wall and the permeability increases significantly. This helps in the subsequent drying or extraction of valuable components from the biomass (Hendrawan, et al., 2019).

2.3 Extraction of Cellulose

One of the main usages of lignocellulosic biomass is the derivatives of cellulose. However, cellulose is very difficult to be extracted. All the current technologies for the extraction of cellulose are considered inefficient nor environment friendly in overall. Most of the currently investigated cellulose extraction were using acid hydrolysis. Besides, ionic liquid is also getting more attention.

2.3.1 Acid Hydrolysis

Acid hydrolysis is the most important and common way of extracting cellulose from pre-treated biomass currently. The conventional acids used in extracting cellulose is either hydrochloric acid or sulfuric acid (Hafid, et al., 2021). Besides, acetic acid, phosphoric acid and hydrobromic acid are also used (Lau, et al., 2018).

Usually, the biomass first undergoes physical size reduction treatment of cutting, grinding to obtain their powder form. This is to increase the surface area and accessibility of the following chemicals. Then, the biomass would be subjected to alkali pre-treatment and oxidative bleaching to remove hemicellulose and lignin, respectively. Hemicellulose is soluble in alkali solution. Lignin can be easily removed as its aromatic ring and ether bond are susceptible to oxidation. Besides, all the processes are usually done with elevated temperature to increase the rate of reaction.

The literature review of cellulose extractions utilising acid hydrolysis is summarised in Table 2.3. As the degree of hydrolysis strongly affects the properties of cellulose extracted, the acid hydrolysis duration, temperature, and concentration of acid used are very important in determining the properties of cellulose extracted (Joy, et al., 2015). Different type of biomass has different optimum condition of combination of the three factors. Usually, the acid used is strong with mass fraction up to 60 wt % (Lau, et al., 2018). Besides, the common temperature of acid hydrolysis would be mild (below 100 °C) with appropriate reaction time (45 minutes to 2 hours) (Sukyai, et al., 2018; Zianor Azrina, et al., 2017).

The function of acid hydrolysis is hydrolysing the amorphous part along microfibrils, yielding the crystalline parts of cellulose (Joy, et al., 2015). Acid hydrolysis extraction method is widely used in extractions where products of nanocrystalline or microcrystalline cellulose are opted for (Borjesson and Westman, 2015).

According to Kargarzadeh, Ahmad and Thomas (2017), the benefit of acid hydrolysis is the ability to recover the acids used after cellulose extraction to save costs. Besides, acid hydrolysis is also considered more energy saving and easier to perform, compared to other cellulose extraction methods currently available (Gopi, et al., 2019).

However, acid hydrolysis has its drawbacks such as time consuming, costly and corrosive chemicals and loss of cellulose (Zianor Azrina, et al., 2017). The yield of cellulose drops significantly when highly concentrated sulphuric acid or hydrochloric acid (more than 60 wt %) is used. Strong sulphuric acid causes sulfation and oxidation of cellulose while hydrochloric acid causes flocculation of cellulose. The acids also cause more dispersion of cellulose into the solution. As a result, the yield is reduced when the acid is washed away. Other characteristics such as low temperature stability and low crystallinity of extracted cellulose are also caused by the usage of strong acid during cellulose extraction (Kargarzadeh, Ahmad and Thomas, 2017).

Table 2.3: Cellulose Extraction Utilising Acid Hydrolysis.

Biomass	Pre-treatment	Condition of Acid Hydrolysis	Acid Used	Cellulose Concentration Obtained	References
Rice husk	Sodium hydroxide	2 hours at 120 °C	Acetic acid (25 wt %) + Sulphuric acid (5 wt %)	63.38 %	(Hafid, et al., 2021)
			Acetic acid (25 wt %) + Nitric acid (10 wt %)	65.51 %	
Roselle fibre	None	30 minutes at 45 °C	Sulfuric acid (50 wt %)	12.51 %	(Lau, et al., 2018)
		45 minutes at 45 °C		20.64 %	
		60 minutes at 45 °C		21.92 %	
Turmeric spent	Sodium hydroxide and sodium chlorite	1 hour at 50 °C	Sulfuric acid (60 wt %)	98.46 %	(Gopi, et al., 2019)
Bamboo fibre	Sodium hydroxide and sodium hypochlorite	30 minutes at 85 °C	Hydrochloric acid (2.5 mol/L)	80 %	(Rasheed, et al., 2020)

Table 2.3: (Continued)

Biomass	Pre-treatment	Condition of Acid Hydrolysis	Acid used	Cellulose Concentration Obtained	References
Sugarcane bagasse	Steam explosion and sodium chlorite	75 minutes at 45 °C	Sulfuric acid (60 v %)	87.68 %	(Sukyai, et al., 2018)
Date palm	Supercritical carbon dioxide, sodium hydroxide and sodium chlorite	60 minutes at 45 °C	Sulfuric acid (50 wt %)	65 %	(Shaikh, et al., 2021)
Oil palm fruit branch	Sodium hydroxide and dimethyl sulfoxide	2 hours at 45 °C	Sulfuric acid (64 v %)	87.7 %	(Zianor Azrina, et al., 2017)
African baobab leaves	Potassium hydroxide and hydrogen peroxide	15 minutes at 105 °C	1-butyl-3-methylimidazolium hydrogen sulfate	88.76 %	(Chowdhury, et al., 2019)

2.3.2 Ionic Liquid

Recently, the use of ionic liquid in cellulose extraction has received increasingly more attention. Ionic liquid are solvents that have unique properties of high thermal and chemical stability, high polarities, non-flammable, and negligible vapour pressure.

Table 2.4 shows the summary of the usage of ionic liquids in cellulose extraction from biomass. The cellulose extraction by ionic liquid is by the reorientation of hydroxyl groups in the cellulose molecule due to interaction with ions in the ionic liquids (Caputo, et al., 2021). Usually, ionic liquid extraction of cellulose is performed under high temperature (slightly higher than 100 °C) in short period of time (below 30 minutes). The current common challenges of commercialisation of ionic liquid extraction of cellulose are the toxicity, high cost of ionic liquids and elevated temperature required (Ejaz, et al., 2020).

2.4 Cellulose-Derived Catalysts

Cellulose-derived catalysts are getting more attention in recent years. Cellulose had many oxygen-containing functional groups on the surface, granting it high hydrophilicity and biocompatibility (Gan, et al., 2019). Besides, wide abundance of cellulose also made it a potential widely used material for catalytic applications. Cellulose-derived catalysts were catalysts hybridised into cellulose or cellulose based materials such as graphene, activated carbon (AC) and metal organic frameworks (MOF). When functionalised or grafted with molecules or other materials, certain chemical or physical properties of cellulose were enhanced and applied (Ahamad, et al., 2019). Besides, inherent disadvantages inherent in certain materials for catalysts such as low solubility, weak in strength, tend to agglomerate and hard to be recycled were mitigated or solved when cellulose was used together (Zik, Sulaiman and Jamal, 2020; Gupta, et al., 2020).

Table 2.4: Cellulose Extraction Utilising Ionic Liquid.

Biomass	Pre-treatment	Condition of Ionic Liquid Extraction	Ionic Liquid Used	Cellulose Concentration Obtained	References
Buckwheat chaff	Mechanical blending	10 minutes at 120 °C	1:5 ratio of propylene carbonate to	5.44 %	(Caputo, et al., 2021)
			1-butyl-2,3-dimethylimidazolium chloride	9.7 %	
			1-butyl-3-methyl imidazolium acetate	20.16 %	
			Tetrabutyl ammonium acetate		
Municipal primary sludge	Powdered	24 hours at 100 °C	Tetrakis (hydroxymethyl) phosphonium chloride	25.3 %	(Glinska, et al., 2020)
Industrial paper sludge	Powdered	24 hours at 100 °C	Tetrakis (hydroxymethyl) phosphonium chloride	32.8 %	

2.4.1 Metal Oxides/Cellulose

Cellulose-derived metal oxides catalysts as a hybrid of inorganic-organic nanocomposites were a new class of catalysts that were being widely researched. Table 2.5 shows the summary of recently developed catalysts and their applications. Different cellulose-derived metal oxides catalysts had been prepared, ranging from aluminium oxide, iron oxides, copper oxide, titanium dioxide (TiO₂) to others. The synergistic effect between the organic cellulose and inorganic metal oxides had granted the catalysts some desired properties such as high reusability, high yield and ease to generate.

One of the most prominent properties of cellulose-derived metal oxide catalysts was the high dispersion of metal oxide on cellulose. When the metal oxides of nano sizes were dispersed on the cellulose, the undesired phenomenon of agglomeration of metal oxides were significantly reduced compared to reactions with bare metal oxides as catalysts (Hamzavi, et al., 2020). The dispersion and reduced agglomeration increased the aspect ratio and total surface area to volume ratio of the metal oxides. As a result, more active sites were exposed to the reactants and the turnover frequency of the catalysts were also increased significantly compared to metal oxides catalysts without cellulose (Gan, et al., 2019). Cellulose-derived metal oxide catalytic reactions were usually of very high yield, often more than 90 % (Boroujeni and Tahani, 2017; Zik, Sulaiman and Jamal, 2020).

Besides, the sorbent properties of catalysts in catalytic reactions were enhanced with the integration of metal oxides into cellulose. The functional groups in cellulose such as hydroxyl groups increased the adsorbent of targeted components and hence the catalytic activity of the metal oxides was also enhanced (Thanaraj, et al., 2019). The adsorption capacity of cellulose-derived metal oxide catalysts was significantly higher than pure metal oxides (Zirak, et al. 2018). Other than functional groups, the abundant pores of cellulose also contributed to the adsorption of reactants and increase in rate of reaction (Gan, et al., 2019).

High stability was one of the advantages of utilising cellulose-derived metal oxides catalysts. The leaching of metals or release of toxic ions into the reaction solutions due to metal oxides used was prevented when metal oxides are anchored in cellulose (Thanaraj, et al., 2019). The stability of the cellulose-

Table 2.5: Summary of Recently Developed Cellulose-Derived Metal Oxide Catalysts.

Catalysts	Applications	Significant Findings	References
Cellulose/ aluminium oxide composite-supported imidazolium chloroaluminate ionic liquid (Cellulose/Al₂O₃-[MeIm]Cl-XAlCl₃)	Solvent free synthesis of xanthenes	1) 95 % yield of 9-(4-nitrophenyl)-3,3,6,6-tetramethyl-3,4,5,6,7,9-hexa-hydro-1H-xanthene-1,8(2H)-dione was achieved 2) 1,8-dioxo-octahydroxanthenes could be synthesised from acid-sensitive aldehydes without by-products 3) Desired properties of ionic liquids and advantages of a solid support were combined	(Boroujeni and Tahani, 2017)
Nanocrystal cellulose/ calcium oxide supported by polyvinyl alcohol (NCC/CaO-PVA)	Biodiesel production from kitchen waste	Maximum yield of 98.40 % at optimum condition of 65 °C; 0.5 wt % catalyst loading; 6:1 methanol to oil ratio	(Zik, Sulaiman and Jamal, 2020)
Copper oxide decorated on cellulose nanocrystals (CuO-CNs)	Synthesise of 2-amino-4H-benzo[b]pyran derivatives	Derivatives were synthesised with high yield (81 – 97 %) at room temperature	(Thanaraj, et al., 2019)

Table 2.5: (Continued)

Catalysts	Applications	Significant Findings	References
Cellulose-copper (II) oxide composite (Cellulose/Cu)	Click reaction synthesis of 1,2,3-Triazole from phenylacetylene and benzyl azide reduced by sodium ascorbate	1) High yield (84 – 92 %) of 1,2,3-Triazole were obtained with the catalyst at various conditions 2) 50 °C was the optimum temperature and large yield drop when temperature is changed slightly	(Hamzavi, et al., 2020)
Cobalt ferrite supported by cellulose-derived carbon nanofibre (CoFe₂O₄/CCNF)	Activation of peroxymonosulfate to oxidise organic pollutant of dimethyl phthalate	1) New catalyst successfully developed for dimethyl phthalate oxidation 2) Sulphate ion was the dominant active species in dimethyl phthalate oxidation	(Gan, et al., 2019)
Palladium and platinum containing, cellulose bead promoted with iron oxide (Pd-Pt/CB-Fe₂O₃)	Reduction by hydrogenation of chlorate	1) Highest reduction of chlorate (92.5 %) at 7:1 ratio of palladium to platinum in catalyst 2) Iron oxide increased the adsorption and desorption of chlorate at the catalyst	(Sikora, et al. 2021)

Table 2.5: (Continued)

Catalysts	Applications	Significant Findings	References
Nitrogen-doped graphitic carbon-contained titanium dioxide (NGC-TiO₂)	Adsorption removal of nitrophenol from water	<p>1) 4-Nitrophenol was removed most effectively among nitrophenol with 80 % removal</p> <p>2) pH 3 was optimal for nitrophenol removal by NGC-TiO₂</p> <p>3) Catalyst adsorption capacity was at 52.91 mg/g</p>	(RanguMagar, et al., 2019)
Cellulose-titanium dioxide-zirconium dioxide composite (Cellulose-TiO₂-ZrO₂)	Glucose conversion to 5-ethoxymethylfurfural	Maximum yield of 45.50 % at optimal condition of 4 hours reaction, 160 °C, 1:1 ratio of dioxides in composite	(Dini, Helmiyati and Krisnandi, 2021)
Carboxymethyl cellulose coated iron (II, III) oxide at silicon dioxide core-shell magnetic nanoparticles (CMC coated Fe₃O₄@SiO₂ MNPs)	Adsorption removal of methylene blue (MB) from water	<p>1) Maximum removal of 85 % at optimal availability of active sites at 0.03 g catalyst with 70 ppm MB</p> <p>2) Increasing temperature and pH, decreasing ionic strength of solution increases removal efficiency</p>	(Zirak, et al., 2018)

derived metal oxides catalysts also contributed to their high reusability frequently reported. Most of the cellulose-derived metal oxides catalysts were able to be regenerated easily and reused at least four times without significant decrease in their catalytic activities (Sikora, et al., 2021; Zik, Sulaiman and Jamal, 2020).

2.4.2 Carbon Materials/Cellulose

As the most abundance source of carbon, cellulose had been utilised in developing many carbon material-based catalysts for water treatment. Table 2.6 summarises the recently developed cellulose-derived carbon material catalysts. Graphene, AC and MOFs were the most intensively researched variants of cellulose-derived catalysts.

One of the most utilised cellulose-derived carbon material catalysts in water treatment and other applications was graphene. Graphene was a two-dimensional carbon sheet structure formed by sp^2 bonds between the carbon atoms. Based on the surface oxygen content, graphene had several variants such as graphene, graphene oxide and reduced graphene oxide. With the oxygen functionalities on it, graphene could interact and adsorb many compounds very effectively by forces such as hydrogen bonding, dispersion force and electrostatic interaction (Gopalakrishnan, Singh and Badhulika, 2020; Niakan, et al., 2021; Zhang, et al., 2017). Other substances such as metal nanoparticles and MOF could be added to modify cellulose-derived graphene to suit their applications. Iron was hybridised into graphene as nanocomposite to provide synergistic effect of catalysts such as high adsorption and easily retrievable by magnet (Ain, Farooq and Jalees, 2020). There were also increases in surface area, charges, active sites and pore size of catalyst when graphene was integrated with MOF (Firoujaei, et al., 2020).

AC was also one of the cellulose-derived catalysts. It was obtained from the pyrolysis of lignocellulosic biomass in the absence of oxygen. Various kinds of lignocellulosic biomass containing carbon were suitable to be used as the source of AC. The activations of carbon could be done before or during the pyrolysis by soaking the biomass in suitable chemicals. The ratio of biomass to activation chemical were crucial for the percentage yield of AC from biomass. The two most frequently used activation chemicals were potassium hydroxide

Table 2.6: Summary of Recently Developed Cellulose-Derived Carbon Material Catalysts.

Catalysts	Applications	Significant Findings	References
Iron magnetised graphene oxide	Removal of heavy metal ions and water disinfection	1) Maximum adsorption capacities of heavy metal ions of lead (Pb^{+2}) and zinc (Zn^{+2}) were 200.00 and 63.694 mg/g, respectively 2) High removal efficiency of 98.787 %, 97.150 % and 97.689 % towards three kinds of different bacteria	(Ain, Farooq and Jalees, 2020)
Graphene oxide-copper metal-organic framework (GO-Cu-MOF)	MB removal	1) Maximum adsorption capacity at 262 mg/g 2) Optimum removal at temperature at 65 °C	(Firoujaei, et al., 2020)
Molybdenum disulfide nanosheet/ graphene hybrid on cellulose filter paper (MoS₂-G-CFP)	MB removal	1) Fast removal of dye within 2 minutes due to electrostatic interaction occurred 2) Maximum adsorption capacity of 485.4 mg/g	(Gopalakrishnan, Singh and Badhulika, 2020)

Table 2.6: (Continued)

Catalysts	Applications	Significant Findings	References
Cellulose-modified magnetite-graphene oxide nanocomposite immobilised palladium (GO-Fe₃O₄-Cellulose-Pd)	Heck and Sonogashira coupling reactions of aryl or alkyl halides with terminal alkenes and alkynes in deep eutectic solvents	<p>1) Dimethyl ammonium chloride (DMAC) and glycerol (Gly) were the best performance solvent</p> <p>2) Maximum yield of 98 % in Heck reactions with optimum condition of 0.75 mol % catalyst, 1:2 ratio of DMAC to Gly, 100 °C and 5 hours reaction time</p> <p>3) Maximum yield of 96 % in Sonogashira reactions with optimum condition of 1 mol % catalyst, 1:2 ratio of DMAC to Gly, 120 °C and 5 hours reaction time</p>	(Niakan, et al., 2021)
Hierarchical porous cellulose/AC composite monolith	Removal of MB and rhodamine B (RhB) from water	<p>1) Maximum adsorption capacities of 159 and 33.4 mg/g for MB and RhB respectively</p> <p>2) Optimum condition at 0.30 g/L catalyst loading and 60 °C, pH 8 and pH 3 for MB and RhB respectively</p> <p>3) No drop of activity after 8 successive cycles of adsorption</p>	(Bai, et al., 2017)

Table 2.6: (Continued)

Catalysts	Applications	Significant Findings	References
Cellulose /AC composite monolith	Phenol removal from water	Maximum adsorption capacity of 45 mg/g at phenol concentration of 0.8 mg/L	(Xiong, et al., 2018)
AC	MB removal from water	1) Phosphoric acid pre-treated AC had highest adsorption capacity at 303.03 mg/g among various acid 2) Optimum adsorption condition at pH 7, 30 °C	(Zhu, et al., 2017)
	Mono-phenol production via catalytic microwave pyrolysis of cellulose	1) Maximum yield of AC (44.4 wt %) from pyrolysis when 0.85:1 ratio of phosphoric acid to biomass was used 2) Maximum yield of mono-phenol (44.4 wt %) at 450 °C for 15 minutes	(Zhang, et al., 2018)
	Antibiotics (amoxicillin and sulfamethoxazole) removal from water	1) Optimum condition of AC yield from pyrolysis at 800 °C for 20 minutes and 1:5 ratio of potassium hydroxide to paper sludge 2) Effective removal of amoxicillin (85 %) and sulfamethoxazole (72 %)	(Sousa, et al., 2021)

Table 2.6: (Continued)

Catalysts	Applications	Significant Findings	References
Carboxymethyl cellulose fibre-supported copper terephthalate metal-organic framework (Cu(BDC)/CMC)	Aerobic oxidation of alcohols	1) High yield of converting primary alcohols to aromatic aldehydes (70 – 94 %) 2) Overcame the defects of Cu(BDC) as catalyst such as deactivation and non-reusability	(Javanbakht, et al., 2021)
Cellulose stabilised Fe₃O₄ and cobalt (II)-based metal organic framework (Fe₃O₄/cellulose/Co-MOF)	Knoevenagel condensation of aromatic aldehydes with malononitrile	1) Optimum conditions of Knoevenagel condensation of malononitrile with benzaldehyde at 15 mg catalyst using ethanol as solvent and 10 minutes reaction time 2) High reusability of catalyst up to five times with no significant drop of performance	(Zare and Rafiee, 2020)
Microcrystalline cellulose/metal organic framework 199 hybrid (MCC/MOF-199)	Extraction of chlorophenols	1) 81.0 % extraction of 0.1 ng/mL to 200 ng/mL of 2-chlorophenol and 4-chlorophenol; 88.3 % extraction of 0.15 ng/mL to 200 ng/mL of 2,3-dichlorophenol and 2,5-dichlorophenol	(Ghaemi and Amiri, 2020)

Table 2.6: (Continued)

Catalysts	Applications	Significant Findings	References
Cellulose acetate/metal organic framework-derived porous carbon (CA/MOFDPC)	Adsorption of MB	1) Optimum membrane was formed from 15 wt % polyethylene glycol as pore former agent and 2 wt % MOFDPC 2) 98.2 % removal of MB	(Tahazadeh, et al., 2021)
MIL-100(Fe) – coated cellulose paper	Adsorption of paracetamol	Optimum adsorption efficiency of 89.75 % at 35.6 mg/L paracetamol initial concentration, 6.44 pH, 167.06 minutes agitation time and 16.87 mg/L adsorbent dosage	(Yilmaz, Zengin and Sahan, 2021)

and phosphoric acid (Sousa, et al., 2021). AC had a very large specific surface area and excellent adsorption capacity (Bai, et al., 2017). These two properties were due to AC's extensive pores in its structure. Its excellent adsorption capacity made it a very good adsorbent and was used in many studies on pollutants removal from water (Xiong, et al., 2018). Other than adsorption removal of undesired pollutants, AC was also used as catalyst such as pyrolysis reaction (Zhu, et al., 2017). On the other hand, AC was hard to be recovered once used due to its powder form. However, the combined usage of AC with other substance or in monolith form could avoid the difficulty in recovery while maintaining the high surface area and pore volume of AC (Zhang, et al., 2018).

Cellulose-supported MOF catalysts are also gaining attention in recent years due to their unique features. MOFs are a class of compounds composed of metal ions or metal clusters coordinated in organic ligands (Lin, et al., 2021). They have special features include large surface area, high porosity, controllable topologies and chemical tenability. Javanbakht, et al. (2021) developed Cu(BDC)/CMC and found out that the Cu-based MOF possessed excellent catalytic performance and high selectivity in aerobic oxidations of alcohols to aldehydes and ketones. There were also no undesired further oxidations to carboxylic acids. Besides, the developed composite had only negligible loss of MOF after being recycled for four times. This proved the compositing of Cu(BDC) into CMC solved the deactivation and poisoning problems of Cu(BDC) when being used individually.

On the other hand, Zare and Rafiee, (2020) developed a novel catalyst of $\text{Fe}_3\text{O}_4/\text{cellulose}/\text{Co-MOF}$ for Knoevenagel condensations of aromatic aldehydes. The catalyst was reported to be highly economic and had high recyclability and excellent yields. Besides, the heterogeneous catalyst needed only room temperature and short reaction time compared to other catalytic conversions of Knoevenagel condensation reactions. In addition, cellulose's high adsorption capability also attracted attention from researchers to develop cellulose-supported MOF catalysts for the adsorption and removal of water pollutants. For example, MCC/MOF-199, CA/MOFDPC and MIL-100(Fe) – coated cellulose paper were developed to remove chlorophenols, methylene blue (MB) and paracetamol respectively (Ghaemi and Amiri, 2020; Tahazadeh, et al., 2021; Yilmaz, Zengin and Sahan, 2021). The catalysts were all reported

to have excellent adsorptive performance and high removal efficiency towards the targeted pollutants.

2.5 Photocatalysis

Photocatalysis had been one of the novel ways in water treatment where degradation of pollutants was accelerated in the presence of photocatalysts under visible or ultraviolet (UV) radiation. The first recorded photocatalysis performed was in 1911, where German scientist Dr Alexander Eibnor conducted dark blue pigment bleaching using zinc oxide (ZnO) under sunlight (Saravanan, Francisco and Stephen, 2017). Subsequently, various studies on photocatalysts had been carried out but the advancement in the field was limited. In 1938, TiO₂ was discovered. Since then, TiO₂ had been remaining as the most utilised photocatalyst. The next breakthrough in the study of photocatalysis was in 1972, Japanese scientists Akira Fujishima and Kenichi Honda discovered the electrochemical photolysis of water utilising platinum and TiO₂ under UV (Tanaka, et al., 2017). The successful production of hydrogen with a very low voltage by photocatalysis compared to the conventional production method had a significant impact to drive resources and attention of researchers towards studies in photocatalysis (Zhang, et al., 2019).

Since then, photocatalysis had been applied and researched in many fields. Water splitting to obtain hydrogen as a potential energy source was one of the major fields in photocatalysis (Tanaka, et al., 2017). Besides, water treatment and air treatment by photocatalysis were also increasingly being researched. In general, the same mechanisms and principles of photocatalysis applied to these applications except the types of photocatalyst, reactants and products (Saravanan, Francisco and Stephen, 2017). The major advantages of using photocatalysis compared to conventional processes were significantly less energy required, no formation of harmful or secondary wastes, mild reaction conditions and modest reaction time (Nagarajan and Venkatanarasimhan, 2019; Zou, et al., 2019). Photocatalysis also had high versatility as it could be applied on solid, liquid and gas phase reactions. In some cases, a few desired reactions could take place at the same time. For instance, organic dye rhodamine B (RhB) could be treated with heavy metal ion, hexavalent chromium (Cr(VI)) at the same time with photocatalysis (Gan, et al., 2020).

2.5.1 Principles

There was an energy gap between the semiconductors' valence band and conduction band (Saravanan, Francisco and Stephen, 2017). Figure 2.6 shows the band gap of various semiconductors at pH 7. In the energy gap, no electronic states could exist. However, electrons could be excited and transferred from valence band to conduction band. The minimum energy difference for an electron to be excited and jumped from the semiconductors' valence band to the conduction band was termed band gap energy (Ghosh, 2018).

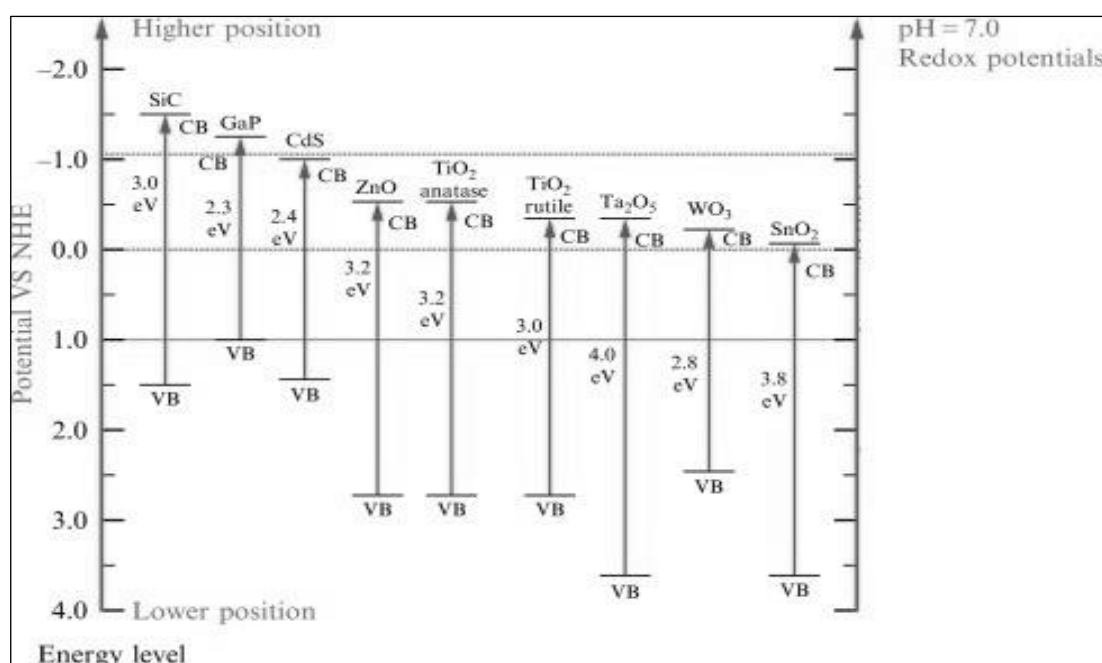


Figure 2.6: Band Gap Energy of Various Semiconductors (Saravanan, Francisco and Stephen, 2017).

When UV or visible light was radiated upon photocatalysts, the energy of incoming photons was absorbed and changes occurred in the electronic structure of the photocatalysts. If the band gap of the photocatalyst was equivalent to or smaller than the incident electromagnetic radiation, the electrons in the valence band could be excited by absorbing the photons (Saravanan, Francisco and Stephen, 2017). The photocatalysts were then activated. Photocatalysis was initiated when the charges were utilised in converting reactants to products in redox reactions as shown in Figure 2.7. The excited electrons moved from the valence band to conduction band and holes

were formed in the valence band. Next, the electrons and holes made up a resultant negative and positive charge in the respective bands. These charges enabled redox reactions to take place on the photocatalysts (Zhang, et al., 2019). Redox reaction occurred when oxidation happened at valence band and reduction happened at conduction band.

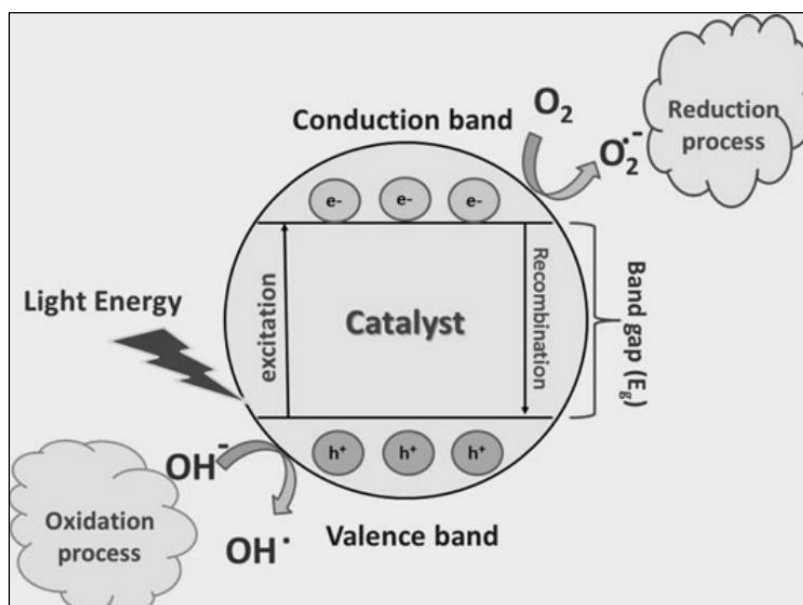


Figure 2.7: Photocatalysis and Redox Reaction (Zhang, et al., 2019).

Based on electronic properties, materials could be broadly divided into insulators, semiconductors and conductors. Figure 2.8 shows the band gap energy of materials. Conductors' valence band and conduction band were overlapping and only electrons are available for oxidation reaction (Tanaka, et al., 2017). Hence, no redox reaction could take place and conductors were not suitable as materials for photocatalysis. On the other hand, insulators' band gap were too large and free electrons were lacking. Hence, large energy was required for conductors to be photocatalysts and only reduction reactions were available. Insulators were not suitable to be photocatalysts. Semiconductors had moderate band gap and low electron hole pair recombination rate (Saravanan, Francisco and Stephen, 2017). Although metal oxides, sulphides and selenides could absorb the energy from the UV-visible light spectrum, only metal oxides were not toxic and stable to undergo photocatalysis (Ghosh, 2018). Besides, organic materials such as carbon nanotubes, graphene, MOF could also utilise the

energy from UV or visible light and were suitable to be material for photocatalysts.

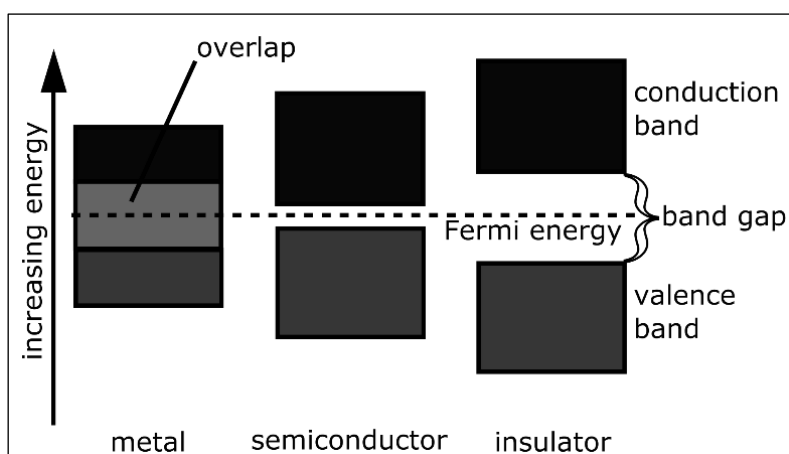


Figure 2.8: Band Gap Energy of Materials (Tanaka, et al., 2017).

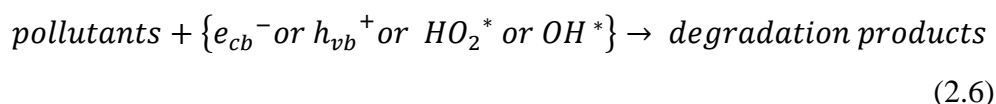
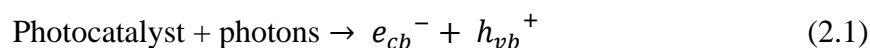
Other than suitable material which could utilise light energy, a well-performing photocatalyst had certain general criteria to fulfil. First, its electron hole pair recombination must be slow (Saravanan, Francisco and Stephen, 2017). This was to extend the time of electrons and holes in conduction and valence bands respectively to fully utilise the energy for reactants to react and photocatalysis to take place. Besides, the charge transportation must be rapid (Ghosh, 2018). As the reaction took place on the surface of photocatalysts, electrons and holes should reach the surface at a high rate and speed to maintain the rate of reaction. Next, the photocatalysts' adsorptivity of reactants must be high (Tanaka, et al., 2017). This was to prevent the occurrence of low rate of reaction due to insufficient reactants at the surface of photocatalysts. Last, the photocatalysts that were responsive to the broad spectrum of solar light were preferred (Zou, et al., 2019). The photocatalysts that could absorb electromagnetic radiation of a broader range were more versatile to work under different conditions of light.

2.5.2 Mechanisms

In general, photocatalysis removal of pollutants in wastewater treatment consisted of the five basic steps of surface reaction (Zou, et al., 2019; Chang, et al., 2021). First, the pollutants diffused across the bulk solution, followed by

adsorption on the surface of catalysts, surface reaction and desorption. Finally, the diffusion of products off the catalysts' surface happened.

The general reactions of photocatalysis are represented by Equation (2.1) to Equation (2.7) (Ghosh, 2018; Saravanan, Francisco and Stephen, 2017; Zhang, et al., 2019). Pollutants could either directly react with electrons in conduction band (e_{cb}^-) and holes in valence band (h_{vb}^+) or indirectly react with the radicals formed by e_{cb}^- and h_{vb}^+ on the photocatalysts. Water splitting occurred when a water (H_2O) molecule reacted with h_{vb}^+ , forming hydrogen ion (H^+) and hydroxyl ion (OH^-). Dissolved oxygen (O_2) was electrophilic and reacted with e_{cb}^- , forming superoxide anion ($O_2^{\cdot-}$). $O_2^{\cdot-}$ was then protonated by consuming a H^+ , forming perhydroxyl radical (HO_2^*). OH^- lost one electron at h_{vb}^+ and formed hydroxyl radical (OH^*). Lastly, e_{cb}^- and h_{vb}^+ recombined and releases energy in the form of heat or photons.



2.6 Photocatalytic Degradation of Pollutants

In water treatment, cellulose-derived photocatalysis is a growing topic. However, the scientific development of cellulose-derived photocatalysis is still in its early stages. The catalysts are being prepared and examined only in laboratory scale and not deployed in wide application or commercialisation yet. Phenolic compounds, organic dyes and heavy metals are the frequently researched pollutants for cellulose-derived photocatalytic degradation. In most cases, organic dyes were used to test the photocatalytic activity of the newly developed photocatalyst. Besides, semiconductor of various metal oxides is the most utilised type of catalysts in cellulose-derived photocatalysis.

2.6.1 Phenolic Compounds

Phenolic compounds are organic compounds with at least one hydroxyl group directly bonded to an aromatic ring. Phenol compounds are not readily degradable by conventional water treatment methods due to their recalcitrant phenolic ring structure (Margaret, et al., 2021). Hence, phenolic compounds are some of the commonly studied pollutants by cellulose-derived photocatalysis. Phenolic compounds are very useful in various industries as chemical intermediates and feedstocks. They are also being discharged into water bodies from pharmaceuticals, coal mining, explosives, paint, dye industries and others (Ahamad, et al., 2019). Besides, phenolic compounds can also be released into waters when plants or animals die and decompose. Phenolic compounds such as bisphenol A (BPA) and nitrophenol are also toxic to humans and animals (Anku, Mamo and Govender, 2017). When consumed, these phenolic compounds can cause disrupting effects on the endocrine system, gastrointestinal tract, muscle contractions, delay in puberty and others.

Table 2.7 summarises the recent studies in phenolic compounds-polluted water treatments by cellulose-derived photocatalysis. Among the phenolic compounds that were researched, BPA was most frequently researched. BPA also had high resistance against degradation by photocatalysis. However, sulphur and nitrogen doping in cellulose-derived photocatalysts can effectively increase the physical adsorption and speed up the degradation of BPA (Ahamad, et al., 2019; Al-Kahtani, et al., 2019). Besides, Mu, et al. (2017) reported high photocatalytic degradation of BPA using cellulose-derived graphene-supported silver phosphate ($\text{Ag}_3\text{PO}_4/\text{graphene}$). The large surface area and porous structure of graphene significantly increased the adsorption of the hydrophobic BPA onto the composite. As a result, the photodegradation of BPA was enhanced.

On the other hand, the reducing agent sodium borohydride (NaBH_4) was mandatory to be used in photocatalytic degradation of nitrophenol (Gupta, et al., 2020). Zhang, et al. (2017) developed nickel manganese oxide microspheres/cotton cellulose fibre ($\text{NiMn}_2\text{O}_4/\text{CCF}$). They reported that the diffusion distance was shorten for nitrophenol to reach the active sites of the photocatalyst as a result of compositing cellulose fibre with NiMn_2O_4 . Fu, et al. (2018) prepared cellulose-based silver-functionalised zinc oxide nanocomposite

Table 2.7: Recent Studies on Cellulose-Derived Photocatalytic Degradation of Phenols.

Phenolic Compounds	Photocatalysts	Degradation Conditions	Degradation Efficiency	References
BPA	Nitrogen/sulphur doped carbon embedded with zinc sulfide (ZnS-NSDC)	Visible light; pH 7; 0.2 g/L catalyst; room temperature	88 % in 150 minutes	(Al-Kahtani, et al., 2019)
	Cellulose-derived graphene-supported silver phosphate (Ag ₃ PO ₄ /graphene)	Visible light; 25 ° C; 0.5 g/L catalyst; 10 ppm BPA	100 % in 12 minutes	(Mu, et al., 2017)
	Cerium oxide/graphitic carbon nanosheet (CeO ₂ /CNNS)	Visible light; 50 mg/L catalyst; 50 ml of 10 mg/L BPA	93.7 % in 80 minutes	(Ma, et al., 2019)
Phenol	ZnO microrod-reduced graphene oxide composite (ZnO-rGO)	Visible light; 0.2 g/L catalyst; pH 4; 20 ppm phenol	84.2 % in 150 minutes	(Margaret, et al., 2021)
	Bismuth oxybromide/regenerated cellulose composite (BiOBr/RC)	Visible light; 20 mL of 7 mg/L phenol, 3 pieces of 1 cm X 2 cm BiOBr/RC	80 % in 180 minutes	(Li, et al., 2016)

Table 2.7: (Continued)

Phenolic Compounds	Photocatalysts	Degradation Conditions	Degradation Efficiency	References
Nitrophenol	Cellulose acetate-ferric oxide nanocomposite (CA/Fe ₂ O ₃)	UV; 0.1 mM nitrophenol; 5 mg catalyst; 0.5 mL of 0.1 M NaBH ₄	100 % in 13 to 16 minutes	(Bakhsh, et al., 2018)
	Cellulose-based silver-functionalised zinc oxide nanocomposite (AZC)	UV; 0.1 mM 4-nitrophenol; 0.1 M NaBH ₄ ; 0.15 g catalyst	100 % in 12 minutes	(Fu, et al., 2018)
	Nickel manganese oxide microspheres/cotton cellulose fibre (NiMn ₂ O ₄ /CCF)	UV-visible, 10 mg/L nitrophenol, 0.2 g/L catalyst, 0.1 mol/L NaBH ₄	100 % in 15 minutes	(Zhang, et al., 2017)

(AZC) and studied the photodegradation of nitrophenol. The composite possessed high mechanical strength, high thermal stability and excellent antibacterial behaviour. Moreover, the composite developed had comparable nitrophenol photocatalytic degradation performance with expensive photocatalyst of gold-supported TiO₂.

2.6.2 Organic Dyes

One of the most easily spotted water pollution is by dyes. The textile, plastic, rubber, paper, cosmetics and leather industries are the top contributors to dye-polluted water. There are over 100 000 types of dyes available commercially and more than 1×10^6 tonnes of synthetic dyes are produced every year (Nagarajan and Venkatanarasimhan, 2019). Dyes' colour changing, inert, hard to bio-degrade and toxicity properties are highly detrimental to human when they appear in water sources. Besides, dyes also block the penetration of sunlight into water bodies, affecting the activities of aquatic life. One of the most commonly researched topics of cellulose-derived photocatalysts in water treatment is the degradation of organic dyes. Conventional wastewater treatment methods could not effectively treat organic dye wastewater due to their persistency and harmful intermediates formed (Nair, et al., 2021). In fact, dyes removal by photocatalysis is also one of the most effective ways of dealing with dyes-contaminated water as it does not produce any secondary pollutants (Dara, et al., 2021; Morshed, et al., 2020).

Table 2.8 summarises the recent studies in organic dyes polluted water treatments by cellulose-derived photocatalysis. The most commonly studied organic dyes were MB, methyl orange (MO) and RhB. Photocatalytic reduction is the main way of degradations of organic dyes in cellulose-derived photocatalysis (Bakhsh, et al., 2018). A reducing agent is optional in many cases and NaBH₄ is the most used reducing agent (Nagarajan and Venkatanarasimhan, 2019). UV and visible light are the most utilised photon sources for the photocatalytic degradation of dyes (Ng and Leo, 2019).

On the other hand, metal oxides are the most frequently used material in cellulose-derived photocatalysis for organic dyes. Among metal oxides, in cellulose-supported copper (II) oxide (CuO) has a very excellent photocatalytic degradation of organic dyes. It is often reported to be capable of decolourising

Table 2.8: Recent Studies in Cellulose-Derived Photocatalytic Degradation of Organic Dyes.

Organic Dyes	Photocatalysts	Degradation Conditions	Degradation Efficiency	References
Acid red	Copper (II) oxide nanoparticles coated-cellulose sponge (CuO@CS)	UV-visible, 50 mL 40 ppm acid red; 25 mg catalyst; 3.75 mL 1.5 M NaBH ₄	100 % in 6 minutes	(Nagarajan and Venkatanarasimhan, 2019)
	Cellulose-supported Tb ₂ CoMnO ₆ (Tb ₂ CoMnO ₆ /cellulose)	UV; 100 mL 20 ppm acid red; 0.05 g catalyst	38 % in 90 minutes	(Dara, et al., 2021)
Acid green	CuO@CS	UV-visible, 50 mL 40 ppm acid green; 25 mg catalyst; 3.75 mL 1.5 M NaBH ₄	100 % in 6 minutes	(Nagarajan and Venkatanarasimhan, 2019)
Congo red	TiO ₂ /cellulose acetate nanocomposite (TiO ₂ /CA)	Sunlight; 10 ppm, 20 ppm, 30 ppm Congo red	100 %, 75 % 66 % in 12 hours	(Nair, et al., 2021)
		UV; 10 ppm, 20 ppm, 30 ppm Congo red	56 %, 28 %, 21% in 12 hours	
MB	CuO@CS	UV-visible, 50 mL 40 ppm MB; 25 mg catalyst; 3.75 mL 1.5 M NaBH ₄	100 % in 10 minutes	(Nagarajan and Venkatanarasimhan, 2019)

Table 2.8: (Continued)

Organic Dyes	Photocatalysts	Degradation Conditions	Degradation Efficiency	References
	Polyvinyl alcohol-TiO ₂ -microfibrillated cellulose composite film (PVA-TiO ₂ -MFC)	UV; 5 ppm MB	91.45 % in 10 minutes	(Ng and Leo, 2019)
	Cellulose-supported titanium dioxide (cellulose/TiO ₂)	UV; 15 ppm MB; 10 mg catalyst	98.1 % in 20 minutes	(Li, et al., 2018)
		UV; pH 7; 40 mL 50 ppm MB; 5 mg catalyst	98.5 % in 40 minutes	(Morshed, et al., 2020)
MO	Cellulose acetate-ferric oxide nanocomposite-supported silver, copper, nickel (Ag@CA/Fe ₂ O ₃), (Cu@CA/Fe ₂ O ₃), (Ni@CA/Fe ₂ O ₃)	UV-visible; 0.1 mM MO; 0.5 mL 0.1 M NaBH ₄ ; 5 mg catalyst	100 % in 10, 14, 12 minutes	(Bakhsh, et al., 2018)
Remazol black	Cellulose nanofibre-supported nickel ferrite (CNF-NiFe)	UV; 0.1 mL of 30 % w/v hydrogen peroxide; 100 mL of 50 mg/L Remazol black; 50 mg catalyst	100 % in 50 minutes	(Gupta, et al., 2020)

Table 2.8: (Continued)

Organic Dyes	Photocatalysts	Degradation Conditions	Degradation Efficiency	References
RhB	CuO@CS	UV-visible, 50 mL 40 ppm RhB; 25 mg catalyst; 3.75 mL 1.5 M NaBH ₄	100 % in 10 minutes	(Nagarajan and Venkatanarasimhan, 2019)
	Tb ₂ CoMnO ₆ /cellulose	UV; 100 mL 20 ppm RhB; 0.05 g catalyst	22 % in 90 minutes	(Dara, et al., 2021)
	Cellulose-supported silver phosphate (cellulose/Ag ₃ PO ₄)	UV-visible; 25 mg catalyst; 25 mL 10 μM RhB	96 % in 60 minutes	(Tavker, Gaur and Sharma, 2020)
	Cellulose-supported tin sulfide (cellulose/SnS ₂)	Visible light; 10 mg catalyst; 50 mL 10 μM RhB	91 % in 25 minutes	(Tavker and Sharma, 2020)

various dyes such as acid red, acid green, MO and RhB with 100 % efficiency under normal light and requires no sunlight (Bakhsh, et al., 2018). This high efficiency of cellulose-supported CuO catalyst is comparable or even better than the degradation of dyes catalysed by noble metal catalysts (Nagarajan and Venkatanarasimhan, 2019).

Moreover, modifications can be done on cellulose-derived photocatalysts to adapt them to different applications. TiO₂ blended into polyvinyl alcohol (PVA) and cellulose was found to be able to strengthen the photocatalyst (Ng and Leo, 2019). Besides, the addition of PVA improved the dispersion of metal oxide, adsorption of MB and reusability of the catalyst up to 10 times. To utilise solar energy more effectively, a floating photocatalyst was prepared by immobilising TiO₂ in a cellulose acetate (CA) matrix supported by ethylene vinyl acetate by Nair, et al. (2021). The novel floating photocatalyst degraded Congo red completely in half of a day.

2.6.3 Heavy Metals

Heavy metals are defined as metal elements that have high atomic weight or density higher than 5 g/cm³ (Pica, 2021). Some examples of heavy metals are iron, copper, silver, zinc and others. Currently, metal plating, mining, battery, tannery and other industries are releasing heavy metal into the environment (Lin, et al., 2019). The toxic heavy metals are harmful to living even in low concentration and can bio-accumulate in the bodies. However, some of the heavy metals are very important to humans' metabolisms as trace elements.

Cellulose-derived photocatalysts have been extensively researched in getting rid of heavy metals from water. However, most of the studies done are focused on the adsorption of metal ions rather than the photocatalytic degradation of heavy metals (Balasurya, et al., 2020; Omuwere, et al., 2021; Pica, 2021). Table 2.9 summarises the current studies on cellulose-derived photocatalysis on heavy metal degradation. Among the study of cellulose-derived photocatalysis water treatment on heavy metals, the reduction of Cr (VI) is prevalently researched. Cr (VI) is highly carcinogenic and toxic, its derived compounds have lethal doses below 50 mg/kg (Gan, et al., 2020). The common release sources of Cr (VI) into water bodies were tannery, pigment and stainless-steel productions (Qiu, et al., 2019). The reduced product of Cr (VI) is trivalent

Table 2.9: Recent Studies on Cellulose-Derived Photocatalytic Degradation of Heavy Metal.

Heavy metal ions	Photocatalysts	Degradation Conditions	Degradation Efficiency	References
Cr (VI)	Cellulose-supported bismuth oxybromide (BiOBr/CCNF)	Visible light; 500 mg/L catalyst; 10 mg/L Cr (VI)	70 % in 60 minutes	(Gan, et al., 2020)
	Cellulose nanofibre-supported zinc indium sulfide (CNF/ZnIn ₂ S ₄)	Visible light; 40 mg catalyst; 40 mL 50 mg/L Cr (VI)	100 % in 90 minutes	(Qiu, et al., 2019)
	Cellulose-supported molybdenum disulfide (cellulose/MoS ₂)	Visible light; 0.03 g catalyst; 100 mL 50 mg/L Cr (VI)	100 % in 180 minutes	(Lin, et al., 2019)
	Cellulose-supported cerium oxide (cellulose/CeO ₂)	Visible light; 6 mg catalyst; 20 mL 4 ppm Cr (VI)	95 % in 60 minutes	(Zhang, et al., 2017)
	Cellulose acetate/chitosan/single walled carbon nanotubes-supported ferrite/titanium dioxide (CA/chitosan/SWCNT/Fe ₃ O ₄ /TiO ₂)	UV; pH 3; 0.5 g/L catalyst; 20 mg/L Cr (VI)	100 % in 60 minutes	(ZabihiSahebi, et al., 2019)
	Arsenic (V)	CA/chitosan/SWCNT/Fe ₃ O ₄ /TiO ₂	UV; pH 3; 0.5 g/L catalyst; 20 mg/L arsenic (V) ion	100 % in 60 minutes

chromium (Cr (III)), which is one of the trace metals needed in the human body. Hence, the reduction of Cr (VI) is important in water treatment.

Usually, visible light is used in the photocatalytic reduction of Cr (VI) to Cr (III) (Gan, et al., 2020; Zhang, et al., 2017). Besides, cellulose played a major role in the enhanced performance in photocatalytic reduction of Cr (VI) to Cr (III). Qiu, et al. (2019) reported that the hybridisation of zinc indium sulfide ($ZnIn_2S_4$) and cellulose nanofibre (CNF) resulted in the significant increase of active sites, decrement of charge transport distance and improvement in light-harvesting and hydrophilic properties from the individual materials. As a result, Cr (VI) was reduced with high efficiency. Besides, the adsorption of heavy metals such as Cr (VI) and pentavalent arsenic (As (V)) on cellulose acetate/chitosan/single walled carbon nanotubes-supported ferrite/titanium dioxide (CA/chitosan/SWCNT/ Fe_3O_4/TiO_2) were also remarkable (ZabihiSahebi, et al., 2019). The adsorption kinetics of Cr (VI) and As (V) on CA/chitosan/SWCNT/ Fe_3O_4/TiO_2 were significant highly than MB and Congo red of the same concentration. As a result, the performance in photocatalytic degradations of heavy metals using CA/chitosan/SWCNT/ Fe_3O_4/TiO_2 were also better than the organic dyes.

In addition, the photocatalytic oxidation of RhB could be conducted simultaneously with the photocatalytic reduction of Cr (VI) (Lin, et al., 2019). The overall water treatment efficiency was reported to accelerate when the two pollutants mixed (Gan, et al., 2020). This was caused by delayed hole-electron recombination caused by RhB when it was degraded with Cr (VI).

CHAPTER 3

METHODOLOGY AND WORK PLAN

3.1 Systematic Literature Review

The research aim is to investigate the utilisation of biomass-derived cellulose and its derivatives in photocatalysis reaction. To manage vast information and large number of publications, an appropriate method is needed. The methodology of systematic literature review was used in the research to generate findings in a comprehensive and transparent way. Systematic literature review method is a process to identify and critically appraise research publications before collecting and analysing the data (Snyder, 2019). The special feature of systematic literature review was the use of eligibility criteria (Chen, et al., 2020). The panel of eligibility criteria was established as a guideline of content to be searched and reviewed based on the research title. During the process, all empirical evidence from research publications that matched the eligibility criteria were identified, collected and managed. Then, the critical analysis was conducted, and the review findings and conclusions were presented. In the research, the approach consisted of four main stages of planning, searching, screening and reporting.

3.2 Planning

Based on the research aim, the specific research objectives were defined. They were to study the characteristics of cellulose and its derivatives using various physical and chemical methods and to review the parameters that affect the photocatalytic activity of cellulose and its derivatives composite. These specific objectives provided the boundaries of the systematic review and were applied to all subsequent steps in the research. Based on the specific objectives, the scope containing relevant topics (lignocellulosic biomass, lignocellulosic pre-treatments, cellulose extractions, cellulose-derived catalysts, photocatalysis, cellulose-derived photocatalyst were established.

After the defining of objectives and establishment of scope of topics, the eligibility criteria were set. The two main criteria were inclusion and

exclusion criteria. The inclusion criteria signified the relevance of publications to the research. The publications matched with inclusion criteria were collected and proceeded to the next stages. Any works or publications matched with the topics in the scope of study, published from 2017 onwards, published by reliable journal publishers, reported with comprehensive results and information were included.

The exclusion criteria defined the set of unwanted criteria to exclude publications from the research, whether they were out of the scope of research or unfavourable sources of publication. Any works or publications in a language other than English, published earlier than 2017, published by unreliable publisher or author, with nature of reviewing other research, with content related to non-biomass-derived cellulose or non-cellulose-derived catalysts were excluded. The eligibility criteria helped to maintain transparency of the review by excluding information sources that were unnecessary, unreliable or irrelevant to scope of study.

3.3 Searching

Relevant published articles between 2017 and 2021 were examined for the literature review. Database of the Library of University Tunku Abdul Rahman was used as the main bibliographic search engine. Renowned publishers such as Elsevier, Emerald, Springer and Wiley and many others were subscribed by the university and thus available. Other reliable databases such as Scopus, Web of Science, Science Database and PubMed were also searched to maximise the collection and study of relevant publications. These databases and publishers' reliability and diversities are promised besides having a large pool of journals relevant to the research title.

In each subsection, the relevant keywords were used to search for published journals in the search engine. The Boolean strings and wildcard symbols such as "OR", "AND" and "*" were also used to specify the searching. The synonyms and keywords under the topics were also searched. For example, when "dye" is the main researched pollutant, synonyms such as "colourant" and "pigments" were also searched. Besides, "acid red", "methylene blue",

“rhodamine B” which can be categorised under “dyes” were also searched and taken into consideration.

3.4 Screening and Reporting

The systematic screening was done to ensure the completeness and fidelity of the research. The titles, and abstracts of the publications were screened for potential inclusion based on the eligibility criteria set in the planning stage. After the searching and screening, 286 publications from the databases were classified as relevant and they were recorded down. Then, the publications were downloaded and transferred to the personal storage. They were then tagged with their author names, date of publications and title to ease the further assessment.

Once the collection of publications completed, the study of the full texts commenced. Analogues or similar papers were removed to increase the diversities of the review. Publications of low quality or significance were also removed from the pool of reviewing materials. In addition, the reference lists of the publications were also examined for further studies or potentially relevant information sources. Overall, 113 research publications were chosen as final candidates to be critically analysed, summarised and reported in terms of content and other important features.

From the 113 publications, data extractions were performed based on the desired findings. When each of the topic was discussed, all relevant data and information from the publications were studied and reported. The introduction, mechanism, technology used, advantages, disadvantages and the overall trend of the topic of discussion were reported. Tables were also used to summarise and present the parameters in the publications for the relevant topics such as type of reactants, catalysts used, reaction conditions, percentage yields and others.

CHAPTER 4

RESULTS AND DISCUSSION

4.1 Characterisation of Cellulose-derived Photocatalysts

One of the most important studies in cellulose-derived photocatalyst development is characterisation. The understanding of the morphology, thermal stability, functional and crystallinity properties are extremely crucial for the researchers to determine their developed photocatalysts. Various characterisation techniques such as scanning electron microscopy (SEM), field emission scanning electron microscopy (FESEM), Fourier transform infrared (FTIR) spectroscopy, X-ray photoelectron spectroscopy (XPS), X-ray diffraction (XRD) and thermogravimetric analysis (TGA) were used extensively. Characterisations using these techniques in recent cellulose-derived photocatalyst development are discussed in the subsequent subsections.

4.1.1 Surface Morphology

As the performance of a catalyst is highly affected by its size and shape, the surface morphology of a photocatalyst is important to be characterised by scientists when developing photocatalysts. It is a common practice for the researchers to quantify the size and understand the shape of the prepared photocatalysts from SEM micrographs. Figure 4.1(a) to Figure 4.1(c) show the SEM and FESEM micrographs of some cellulose-derived photocatalysts. Al-Kahtani, et al. (2019) observed uniform embedding of spherical zinc sulfide (ZnS) nanoparticles in the carbon matrix and determined that the diameters of the ZnS nanoparticles was from 15 to 25 nm in their developed nitrogen/sulphur doped carbon embedded with zinc sulfide nanocomposite (ZnS-NSDC). Besides, Nair, et al. (2021) confirmed that the uniform nanoflake TiO_2/CA nanocomposite obtained were in the size range of 200 nm. In addition, Zhang, et al. (2017) reported the final size and shape of 400 nm cellulose-supported cerium oxide nanocomposite (cellulose/ CeO_2) after the nano-tube shaped cellulose grew on the circular cerium oxide (CeO_2).

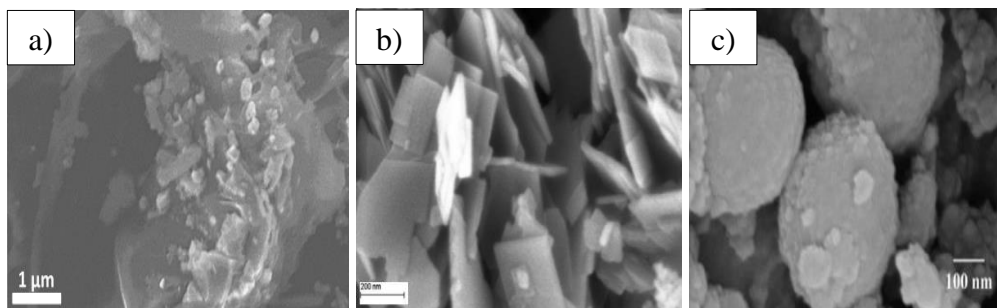


Figure 4.1: (a) SEM Micrograph of ZnS-NSDC (Al-Kahtani, et al., 2019), (b) FESEM Micrograph of Nanoflake Shaped TiO_2/CA Nanocomposite (Nair, et al., 2021) (c) SEM Micrograph of Cellulose/ CeO_2 Nanocomposite (Zhang, et al., 2017).

Next, the most frequently observed morphology in cellulose-derived photocatalysts is the dispersion degree of nanoparticles on the matrix material. The scattered anchoring nanoparticles on another bulkier or larger sized material indicates the successfulness of preparing a nanocomposite as a photocatalyst. Figure 4.2(a) to Figure 4.2(c) show the dispersion of nanoparticles in the photocatalysts. Li, et al. (2016) found that bismuth oxybromide (BiOBr) not only scattered on the surface of cellulose, but also filled and occupied the pores of cellulose at higher density in bismuth oxybromide/regenerated cellulose composite (BiOBr/RC). Besides, Zhang, et al. (2017) also observed the dispersed anchoring of NiMn_2O_4 microspheres on the cellulose fibre of curled and smooth surface. Nagarajan and Venkatanarasimhan (2019) also observed uniformly distributed CuO on cellulose sponge (CS) of smooth surface in copper (II) oxide nanoparticles coated-cellulose sponge ($\text{CuO}@CS$).

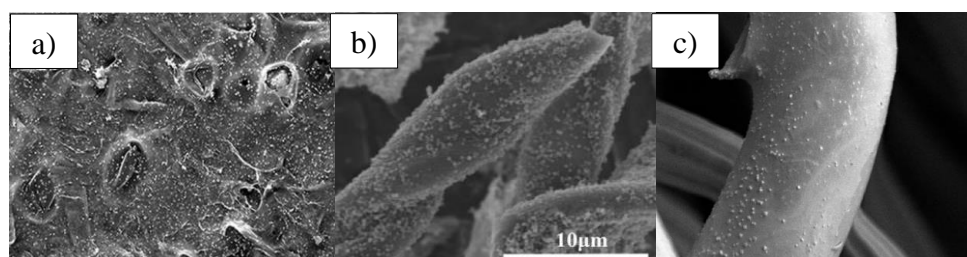


Figure 4.2: SEM Micrographs of (a) BiOBr/RC (Li, et al., 2016) (b) $\text{NiMn}_2\text{O}_4/\text{CCF}$ (Zhang, et al., 2017), (c) $\text{CuO}@CS$ (Nagarajan and Venkatanarasimhan, 2019).

Another usage of SEM micrographs is the observation of morphology of individual materials and after combining them into a composite in cellulose-derived photocatalysts preparation. Figure 4.3 shows the micrographs obtained by Mu, et al. (2017). A significant reduction of the diameter (from 10 to 0.3 μm) and increase in the distribution of silver phosphate (Ag_3PO_4) nanoparticles was found when incorporating with graphene. Besides, the layering of individual graphene was substituted with a spatially reticulated structure wrapping the nanoparticles and an increase in surface area to volume ratio was also obtained. Similar changes in the morphology of ZnO were also observed after combining with reduced graphene oxide (rGO) (Margaret, et al., 2021). On the other hand, the change in shape and structure due to the addition of material into the photocatalysts could be captured and observed using SEM. The change from flower-like microsphere morphology to a 3-dimensional netted structure was observed in ZnIn_2S_4 , after the addition of CNF to the photocatalysts (Qiu, et al., 2019).

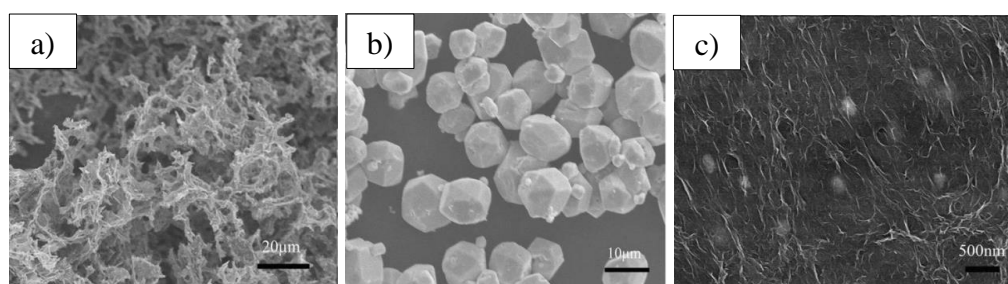


Figure 4.3: SEM Micrographs of (a) Graphene, (b) Ag_3PO_4 and (c) Ag_3PO_4 /graphene (Mu, et al., 2017).

However, there are also some limitations from the SEM analysis. First, the elemental or chemical species of the micrographs are not identified because only the surface morphology is revealed (Bakhst, et al., 2018). Hence, characterisation technique which confirms the species of the specimens such as energy dispersive spectroscopy (EDX) usually follows or is incorporated with SEM (Ng and Leo, 2019; Tavker and Sharma, 2020). Another inadequacy of SEM is the difficulty to observe the changes in the concentration or quantity of photocatalysts. For example, Tavker, Gaur and Sharma, (2020) reported that the

increment of pure Ag_2PO_3 nanoparticles on cellulose was not obvious through the FESEM micrographs alone and the use of EDX was necessary.

4.1.2 Functional Group Analysis

FTIR is commonly used to examine the functional groups of the developed cellulose-derived photocatalysts. FTIR spectrograms have absorption bands and peaks that allow the researchers to identify the types of functional groups in the photocatalysts. Table 4.1 shows the FTIR absorption peaks for the developed cellulose-derived photocatalysts. In the development of ZnO microrod-reduced graphene oxide composite (ZnO-rGO), Margaret, et al. (2021) reported the reduction of oxygen functionalities as compared with rGO. This confirmed the successfulness of reducing the surface of graphene oxide to rGO. Besides, Nagarajan and Venkatanarasimhan (2019) also observed no absorption peak in the wavenumber range of 600 to 660 cm^{-1} , indicating the absence of copper (I) oxide. Hence, they concluded that an observed sharp absorption peak at 525 cm^{-1} found in the CS supporting matrix was attributed to the CuO functional group.

FTIR can also be used to check for the removal of the organic solvents used in the photocatalyst synthesis procedures. Dara, et al. (2021) reported no absorption peaks appeared related to the maltose and date syrup used in photocatalyst synthesis processes of pyrolysis and calcination. This confirmed the effectiveness of solvent removal process in their experiment. On the other hand, FTIR spectra are also important to replicate the previously prepared photocatalyst. Researchers usually compared the FTIR spectrum and the characteristic peaks of their synthesised photocatalyst with spectra reported by others to confirm the successfulness of replicating the photocatalysts (Ng and Leo, 2019). The absorption peak of P-O-P stretching vibration in Ag_3PO_4 at 1097 cm^{-1} shifted to 1122 cm^{-1} after combining with rGO (Mu, et al., 2017). The shift in wavenumber suggested some interactions happened between these two species in the composite. When cellulose was modified by Ag_3PO_4 , two new strong absorption bands at 1000 cm^{-1} and 544 cm^{-1} appeared in the FTIR spectrum (Tavker, Gaur and Sharma, 2020). The bands were caused by the newly formed metal phosphate bonding between the metal nanoparticle and cellulose, indicating a chemical bonding between the two species in the

Table 4.1: FTIR Spectra of Cellulose-Derived Photocatalysts.

Photocatalysts	Wavenumber (cm ⁻¹)	Functional Groups	References
Ag₃PO₄/ graphene	1051	C-O-C stretching vibration of the epoxy and alkoxy groups	(Mu, et al., 2017)
	1391	C-OH stretching vibration	
	1650	C=C stretching vibration	
	550	O=P-O bending vibration	
	850 and 1097	P-O-P symmetric and asymmetric stretching vibration of	
	1383	P=O stretching vibration	
	1570	Skeletal vibration of graphene layers	
	1240	C-O stretching vibration in the epoxy group	
CA/Fe₂O₃	3415	O-H groups in cellulose acetate	(Bakhsh, et al., 2018)
	1630	O-H bending	
	1740	C=O stretching	
	1040	C-H stretching vibration	
	1240	C-O-C asymmetrical stretching vibration	
	1375	C-C stretching vibration	
	590	Fe=O	

Table 4.1: (Continued)

Photocatalysts	Wavenumber (cm ⁻¹)	Functional Groups	References
ZnO-rGO	3200-3500	O-H stretching vibration of amide group	(Margaret, et al., 2021)
	459	Zn-O hexagonal phase stretching vibration	
	1627	C=C and skeletal ring vibration	
	1385	C-OH stretching vibration	
	893	C-OH bending vibration	
CuO@CS	3325	O-H stretching vibration	(Nagarajan and Venkatanarasimhan, 2019)
	1371 and 2895	C-H stretching and deformation vibrations	
	888	β - glycosidic linkage	
	1061	C-O stretching vibration	
	525	Cu-O stretching	
Tb₂CoMnO₆/cellulose	595	Mn-O bond	(Dara, et al., 2021)
	464	Co-O bond	
PVA-TiO₂-MFC	3000-3700	O-H stretching vibration	(Ng and Leo, 2019)
	2900-3000	C-H stretching vibration	
	1700	C=O stretching vibration of ester bond and carboxyl groups	
	1150-1300	C-C stretching	

Table 4.1: (Continued)

Photocatalysts	Waveumber (cm⁻¹)	Functional Groups	References
Cellulose/TiO₂	3450	O-H stretching vibration	(Morshed, et al., 2020)
	2900	CH ₂ group	
	1646.77	O-H bending vibration	
	1373-1642	Ti-O-C vibration	
Cellulose/Ag₃PO₄	3400-3420	O-H stretching	(Tavker, Gaur and Sharma, 2020)
	2920-2922	=C-H group	
	1400-1600	C=C stretching	
	1050-1060	C-O stretching	
	400-700	C-H bending	
	1000 and 544	P-O vibration	
CNF/ZnIn₂S₄	1300-1500	C-H vibrations in cellulose	(Qiu, et al., 2019)
	1300-900	C-O vibrations in cellulose	
	1639 and 1722	C=O stretching vibration in ester group from carbonyl	

Table 4.1: (Continued)

Photocatalysts	Wavenumber (cm⁻¹)	Functional Groups	References
Cellulose/CeO₂	480	Ce-O stretching	(Zhang, et al., 2017)
	1657	C=O stretching	
	3433	O-H stretching vibration	
	1052	C-O stretching	
CA/chitosan/SWCNT/Fe₃O₄/TiO₂	3000-3500	O-H stretching	(ZabihiSahebi, et al., 2019)
	1450-1650	Aromatic rings of SWCNT	
	1600-1650	C-H stretching	
	1670	C=O stretching	
	1310	C-O stretching	
	420, 550	Fe-O stretching	
	400-700	Ti-O vibration	
CeO₂/CNNS	808	S-triazine stretching vibration	(Ma, et al., 2019)
	1200-1700	C=N and C-N stretching vibration	
	3000-3600	O-H and N-H stretching vibration	
	400-700	Ce-O stretching vibration	

composite.

On the other hand, BiOBr and TiO₂ were immobilised onto cellulose through hydrogen bonds (Li, et al., 2016; Morshed, et al., 2020). The absorption peaks of hydroxyl groups of cellulose at 3300-3450 cm⁻¹ shifted to lower wavenumbers after being immobilised on BiOBr (Li, et al., 2016). Similar shifting of hydroxyl group to lower wavenumbers was also observed after loading of TiO₂ onto cellulose (Morshed, et al., 2020).

Moreover, the incorporation of ferric oxide (Fe₂O₃) onto CA did not involve any functional group between the species as there was no change in the FTIR spectra before and after the incorporation (Bakhst, et al., 2018). The metal oxide nanoparticles of Fe₂O₃ were just binding to the host material of CA physically. Similar results were observed between CuO and CS (Nagarajan and Venkatanarasimhan, 2019). The wavenumbers of the peaks and characteristic absorption bands of CS remained the same before and after the loading of CuO.

Apart from confirming the species and checking the bonds of cellulose-derived photocatalysts, FTIR could also be used to check whether the original characteristics of the materials were destroyed during the preparation processes. Graphitic carbon nanosheet (CNNS) could retain its chemical structure in cerium oxide/ graphitic carbon nanosheet (CeO₂/CNNS) after going through ultrasonic irradiation and calcination (Ma, et al., 2019). The characteristic absorption peaks of CNNS remained in FTIR after the anchoring of CeO₂. However, the characteristic bands of cellulose including C-H bending vibration, C-O and C-O-C stretching vibrations disappeared after acid heat treatment with TiO₂ (Morshed, et al., 2020). Besides, the intensity of absorption bands for hydroxyl groups of cellulose also decreased significantly after converted into biochar (Gan, et al., 2020). The absorption peak of O-H stretching at 3300 cm⁻¹ was severely weakened when exposing the cellulose to high temperature.

Overall, FTIR is one of the most widely used characterisation techniques in recent studies of cellulose-derived photocatalysts as it gives important and useful results by determining the chemical species, bonds and original characteristics of materials in the composites. These results from the spectrograms were extremely significant for the characterisations of cellulose-derived photocatalysts.

4.1.3 Chemical State Analysis

XPS technique allows the researchers to identify the types of elements and chemical states of the photocatalysts. Al-Kahtani, et al. (2019) found that carbon, nitrogen, oxygen, sulphur and zinc elements were coexisting on the surface of ZnS-NSDC using XPS survey scanning. Besides, researchers can also determine whether there is any impurity on the cellulose-derived photocatalysts. The survey scan of cellulose-supported tin sulfide (cellulose/SnS₂) revealed that only tin, sulphur, carbon and oxygen were presented and there was no other impurity (Tavker and Sharma, 2020). Tavker, Gaur and Sharma (2020) reported similar findings as there were no other impurity elements on the cellulose/Ag₃PO₄ except silver, phosphate, carbon and oxygen.

After the survey scan, the researchers zoomed into the XPS spectra peaks of the elements presented to characterise high-resolution peaks of the elemental electron states. For each element, the full range of spectra was observed and the bonding energies, types of elemental electrons, and chemical environment of the element were characterised. Table 4.2 shows the XPS spectra of cellulose-derived photocatalysts obtained through XPS. It was worth noting that remarkable shifting to lower binding energy of Ag 3d after being deposited onto ZnO (Fu, et al., 2018). This was caused by the conversion of pure silver to +1 oxidation state. The electrons were transferred from silver to ZnO upon compositing the two materials, indicating a good interaction between the materials.

Another significant result using XPS is to discover the oxidation states of the elements in the cellulose-derived photocatalysts. Table 4.3. shows the oxidation states of elements in cellulose-derived photocatalysts characterised by XPS. This was possible as different oxidation states of elements had unique binding energies. This characterisation was important as the researchers would like to make sure only the desired oxidation states of the element were synthesised or incorporated into the photocatalysts.

Table 4.2: XPS of Cellulose-derived Photocatalysts.

Photocatalysts	Binding Energy (eV)	Elemental Electron	References
ZnS-NSDC	229	S 2s	(Al-Kahtani, et al., 2019)
	532	O 1s	
	1024	Zn 2p	
	1044.08	Zn 2p _{1/2}	
	1021.16	Zn 2p _{3/2}	
	162	S 2p	
	161.8	S 2p _{3/2}	
	162.74	S 2p _{1/2}	
	401	N 1s	
	398.46	Pyridinic N	
	399.54	Pyrrolic N	
	400.91	Graphitic N	
	284	C 1s	
	283.83	sp ² C	
	284.79	sp ³ C	
	285.39	C-S	
286.20	C=N		
288.30	C=O		
Ag₃PO₄/graphene		Ag 3d	(Mu, et al., 2017)
	367.5	Ag 3d _{3/2}	
	373.4	Ag 3d _{5/2}	
		C 1s	
	284.9	C-C or C=C	
	286.6	C-O	
287.7	C=O and O=C-OH		
AZC		O 1s	(Fu, et al., 2018)
	531.3	C-O-C, C-OH	
	530.2	Zn-O	
		Zn 2p	
	1044.6	Zn 2p _{3/2}	
	1021.4	Zn 2p _{1/2}	
		Ag 3d	
	365.8 – 366.1	Ag 3d _{5/2}	
371.8 – 372.1	Ag 3d _{3/2}		

Table 4.2: (Continued)

Photocatalysts	Binding Energy (eV)	Elemental Electron	References
CuO@CS	933.6	Cu 2p	(Nagarajan and Venkatanarasimhan, 2019)
	953.5, 964	Cu 2p _{3/2} Cu 2p _{1/2}	
	530.2, 532.3	O 1s	
BiOBr/ CCNF	284.8	C 1s	(Gan, et al., 2020)
	286.5	C=C	
	288.0	C-O-C, C-OH	
	289.2	C=O O-C=O	
Cellulose/SnS₂	486.6	Sn 3d	(Tavker and Sharma, 2020)
	495	Sn 3d _{3/2} Sn 3d _{5/2}	
	161.2	S 2p	
	162.5	S 2p _{3/2}	
	167.8	S 2p _{1/2}	
		- C - SO _x - Sn	
	284.41	C 1s	
	285.52, 288.30	C-H C-O	
	530.48, 531.49	O 1s	
Cellulose/CeO₂	284.8	C 1s	(Zhang, et al., 2017)
	285.8	C-C or C-H	
	287.9	C-OH	
	290.1	O-C-O	
		O-C-O --- OH	
	529.0	O 1s	
531.2 and 532.7	CeO ₂ C-OH		

Table 4.2: (Continued)

Photocatalysts	Binding Energy (eV)	Elemental Electron	References
Cellulose/Ag ₃ PO ₄	130.02	P 2p	(Tavker, Gaur and Sharma, 2020)
	133.65	P-C P in phosphate group	
	284.8	C 1s	
	286.2	C-H	
	286.4	C-O	
		Cellulose – Ag ₃ PO ₄	
	367.9	Ag 3d	
	373.9	Ag 3d _{5/2} Ag 3d _{3/2}	
	530.56	O 1s	
	532.34	P=O P-O-Ag	
CNF/ZnIn ₂ S ₄	284.8	C 1s	(Qiu, et al., 2019)
	286.1	C-C	
	287.8	C-O	
		C=O	
	534.1	O 1s	
	533.0	C=O	
	532.0	C-O	
		O-H	
	1044	Zn 2p	
	1020.9	2 p _{1/2} 2p _{3/2}	

Table 4.3: Oxidation States of Elements in Cellulose-derived Photocatalyst.

Photocatalysts	Elements	Oxidation States	References
Ag ₃ PO ₄ /graphene	Ag	+1	(Mu, et al., 2017)
Cellulose/SnS ₂	S	-2	(Tavker and Sharma, 2020)
AZC	Zn	+2	(Fu, et al., 2018)
CuO@CS	Cu	+2	(Nagarajan and Venkatanarasimhan, 2019)
Cellulose/Ag ₃ PO ₄	Ag	+1	(Tavker, Gaur and Sharma, 2020)
CNF/ZnIn ₂ S ₄	Zn	+2	(Qiu, et al., 2019)

4.1.4 Crystallinity Properties

The crystallinity properties of cellulose-derived photocatalysts were conducted using XRD technique. The 2θ angles and the respective cryptographic planes obtained from the diffractogram results were unique to the chemical component. In CeO₂/CNNS, the characteristic peaks of both CeO₂ and CNNS were preserved in the XRD diffractogram of the composite (Ma, et al., 2019). This indicated the successful hybridisation during materials preparation. The same condition was also observed for the combination of nickel ferrite (NiFe) and cellulose into a nanocomposite (Gupta, 2020). Besides, when decreasing the ratio of cellulose to NiFe in the nanocomposite, the characteristic peaks of NiFe also became more intense. On the other hand, Gan, et al. (2020) found that a higher pyrolysis temperature led to a higher graphitisation of cellulose in BiOBr/cellulose. The 2θ angle at 44° in the diffractogram unique to biochar became more observable when the pyrolysis temperature of cellulose increased. In cellulose nanofibre-supported zinc indium sulfide (CNF/ZnIn₂S₄), cellulose was much dispersed than on ZnIn₂S₄ than pristine CNF (Qiu, et al., 2019). The characteristic peaks of cellulose at 21.1° and 22.6° became significantly broader and even combined together when ZnIn₂S₄ was hybridised into CNF.

In addition, characterisations using XRD are also useful to check for any impurity or unwanted material in the cellulose-derived photocatalysts. In the XRD characterisations of cellulose acetate-ferric oxide (CA/Fe₂O₃) nanocomposites conducted by Bakhst, et al. (2018), they confirmed that no unwanted oxides or hydroxides of the metal nanoparticles appeared on CA. No characteristic peaks of the oxides or hydroxides of copper, silver and nickel were found in the respective XRD diffractograms of the photocatalysts developed. Margaret, et al. (2021) and Lin, et al. (2019) also confirmed no impurities in their synthesised ZnO-rGO and cellulose-supported molybdenum disulfide (cellulose/MoS₂) respectively.

Ag₃PO₄/graphene had many graphene layers with a spacing distance of 3.67 Å between each other and Ag₃PO₄ was a body-centred cubic structure completely filling the spaces between the graphene layers (Mu, et al., 2017). The crystalline hexagonal wurtzite structure of urchin-like ZnO in ZnO-rGO was also characterised and confirmed using XRD (Margaret, et al., 2021). Moreover, the size of cellulose crystals was found to be at 28 nm and the structure of TiO₂ in cellulose-supported titanium dioxide (cellulose/TiO₂) was anatase (Morshed, et al., 2020). However, TiO₂ existed in a mixture of rutile and anatase in TiO₂/CA (Nair, et al., 2021). On the other hand, Tavker, Gaur and Sharma (2020) reported that cellulose/Ag₃PO₄ consisted of monoclinic structure of cellulose and body-centred cubic form of Ag₃PO₄.

In short, XRD is very useful in cellulose-derived photocatalyst characterisations as the diffractograms give useful results in determining successfulness of compositing materials, presence of impurities and crystallinity structure of cellulose-derived photocatalysts.

4.1.5 Thermal Stability

The thermal resistance of the cellulose-derived photocatalysts was characterised using TGA. The thermal stability and properties of the sample can be studied via the percentage mass drop and temperature range of mass drop (Li, et al., 2016). Sometimes, the first derivative thermographic (DTG) curve of the sample was also generated to identify the temperature with maximum and significant mass change (Li, et al., 2018; Tavker, Gaur and Sharma, 2020). Table 4.4

summarises the TGA and DTG results of the cellulose-derived photocatalysts. TGA curves of cellulose-derived photocatalysts showed one to two major changes in mass and two to three minor or little changes in mass at certain temperature. Polyvinyl alcohol-TiO₂-microfibrillated cellulose composite film (PVA-TiO₂-MFC) had two major mass drops occurred at different temperature (Ng and Leo, 2019). The first mass drop of 10 % occurred from 35 °C to 120 °C was due to the desorption of moisture by the composite film. Another major drop occurred from 200 °C to 460 °C indicated that PVA started degrading from 200 °C and was completely pyrolysed at 460 °C. Only 10 % of the initial mass of the composite was left after the heating process. Hence, it could be deduced that the composite could function without degradation below 200 °C. It was found that 10 % of the total weight loss was attributed to the water molecules and 80 % was PVA. Besides, Li, et al., (2018) reported that cellulose/TiO₂ photocatalyst had two major mass drops in its TGA curves. They also reported that 8 % of weight lost from the first stage of 100 °C to 120 °C was due to the moisture from the composite. The second and third stages of the TGA curve occurred at 120 to 400 °C and above 400 °C were attributed to the degradation of cellulose. The first derivative thermogravimetric curve showed the major mass drop occurred at 237 °C and 316 °C.

Another significance of TGA in characterising cellulose-derived photocatalysts is to identify how thermal stability of the developed material is affected by the loading of nanoparticles or combining both the matrix and active material of the photocatalysts. ZabihiSahebi, et al. (2019) found that the compositing of SWCNT/Fe₃O₄/TiO₂ into supporting medium of CA/chitosan effectively extended the degradation temperature from 206 to 215 °C as compared to CA/chitosan. Besides, the final weight of ash after burning up to 400 °C was increased from 21 to 27 %. These two findings using TGA found out that the incorporation of the SWCNT/Fe₃O₄/TiO₂ nanoparticles increased the thermal stability and resistance of the composite. Similar results were also obtained by Li, et al. (2018). The nanocomposite of cellulose/TiO₂ had ten times lower pyrolysis rate than pristine cellulose. The ash left after a complete pyrolysis up to 800 °C also increased from 15 to 75 % after incorporating TiO₂ into cellulose.

Table 4.4: TGA and DTG Data for Cellulose-Derived Photocatalysts at Different Thermal Degradation Stages.

Photocatalysts	TGA						DTG	References
	First Stage		Second Stage		Third Stage		Temperature	
	Temperature (°C)	Weight loss (%)	Temperature (°C)	Weight loss (%)	Temperature (°C)	Weight loss (%)	Peak (°C)	
ZnO-rGO	150 – 400	9.61	400 – 510	19.49	520 – 800	63	-	(Margaret, et al., 2021)
BiOBr/RC	25 - 280	5	280 - 430	75	450 - 550	25	-	(Li, et al., 2016)
PVA-TiO₂-MFC	35 – 120	10	200 - 460	80	460 - 800	10	-	(Ng and Leo, 2019)
Cellulose/TiO₂	25 - 120	9	120 - 400	16	400 - 800	75	316	(Li, et al., 2018)
BiOBr/ CCNF	0 - 100	12	100 - 380	80	380 - 1000	8	-	(Gan, et al., 2020)
Cellulose/CeO₂	0 - 225	3	225 - 600	73	-	-	340	(Zhang, et al., 2017)
CA/chitosan/SWCNT/ Fe₃O₄/TiO₂	50 - 215	8	215 - 320	65	320 - 400	27	-	(ZabihiSahebi, et al., 2019)

Overall, TGA analysis is less being investigated in the field of photocatalysis due to the common operating condition of photocatalysis is conducted at ambient temperature and most of the decomposition of the photocatalysts happened at higher temperature (Li, et al., 2016). The relatively high decomposition temperature than the operating temperature of the photocatalysis reaction makes TGA analysis not a compulsory characterisation method.

4.2 Parameters Affecting the Photocatalytic Activities of Cellulose-derived Photocatalysts

The main goal of exploring the parameters that affect the photocatalytic activities is to find out the most optimum and effective conditions of photo-degrading the pollutants. Those parameter factors include amount of the cellulose and semiconductor in the composite materials, dosage of cellulose-derived photocatalysts, initial pollutant concentration and solution pH. However, the effects of these parameters are often studied individually while maintaining the rest at constant values in recent studies.

4.2.1 Amount of Cellulose and Semiconductor in Composite Materials

The photocatalytic activities of cellulose-derived photocatalysts are highly dependent on the type and ratio of materials in the composites. It is also the most critical and focused parameter by researchers in recent studies for the development of cellulose-derived photocatalysts (Al-Kahtani, et al., 2019; Gupta, et al., 2020). In general, the type and optimum ratio of cellulose in composite materials can enhance the synergistic effect of developed catalysts such as increasing active sites, decreasing charge transport distance and making light-harvesting more efficient (Qiu, et al., 2019). Besides, the adsorptivity of pollutants by the photocatalysts can also be improved by hybridising with optimum amounts of cellulose-derived materials (Ng and Leo, 2019).

The Cr (VI) reduction capacity of CNF/ZnIn₂S₄ in the first half an hour was reported to increase from 34.0 mg/L to 39.3 mg/L when increasing the cellulose weight percentage in the composite from 20 % to 40 % (Qiu, et al., 2019). ZnIn₂S₄ semiconductor was dispersed evenly on cellulose with low

agglomeration, which increased the surface area to volume ratio and active sites available for photocatalytic activities. Similar result was also obtained by Gupta, et al. (2020) where Remazol black degradation rate constant of cellulose nanofibre-supported nickel ferrite (CNF-NiFe) increased from 0.0236 min^{-1} to 0.0343 min^{-1} when the ratio of CNF to NiFe increased from 1.5:1 to 2.5:1. The agglomeration of NiFe nanoparticles due to the inherent magnetic property of was reduced significantly when the nanoparticles were supported by CNF.

On the other hand, the increase of cellulose content (from 1 to 8 g) in the cellulose/ Ag_3PO_4 photocatalyst improved the RhB degradation rate significantly (from 0.0101 to 0.024 min^{-1}). This was related to the enhancement on the charges' separation and delaying the charges recombination (Tavker, Gaur and Sharma, 2020). Besides, PVA- TiO_2 -MFC's MFC to TiO_2 weight ratio of 1:2 had higher catalytic activity as compared to PVA- TiO_2 -MFC with MFC to TiO_2 weight ratio of 1:4 (Ng and Leo, 2019). The increased cellulose content was reported to improve the mobility and absorptivity of MB to the photocatalyst. In conclusion, the synergistic effect was enhanced when increasing the cellulose content to an optimum value.

However, the Cr (VI) reduction capacity of CNF/ ZnIn_2S_4 decreased from 39.3 mg/L to 31.9 mg/L when weight percentage of cellulose was increased from 40 % to 60 % (Qiu, et al., 2019). This indicated that the light harvesting capability of the composite dropped and less photocatalytic activities occurred if exceeded the optimum cellulose content in the composite material. Similar result was also reported by Mu, et al. (2017) in the BPA degradation by Ag_3PO_4 /graphene. The optimum weight percentage of graphene in the composite material was reported to be 11 wt %. Above the optimum amount, graphene would contribute a nonnegligible shading effect that reduced the light penetration and photocatalytic degradation rate BPA.

On the other hand, the amount of metal oxide is also a major influencing factor for the cellulose-derived photocatalytic activities. Similar to the amount of cellulose-derived material, the amount of metal oxides in the composite materials should be optimum to achieve the highest photocatalytic activities.

When the content of metal oxide increased initially, the availability of radicals needed for photocatalysis increased and photocatalytic activities increased due to the increment of charge separation sites (Li, et al., 2018). However, when the weight percentage of the metal oxide content exceeded the optimum value, metal oxide agglomerated and affected the heterostructure of the composite materials. More recombination sites were generated by the increment of metal oxide in the composite materials, led to a decrement in the photocatalytic activities. The surplus metal oxide also caused light blocking effect where light energy could not be absorbed effectively by the photocatalyst. For instance, the weight percentage of CeO₂ was reported to be optimum at 28.3 % in CeO₂/CNNS (Ma, et al., 2019). The BPA photocatalytic degradation efficiency increased from 81.1 % to 93.7 % and decreased to 81.0 % when CeO₂ wt % was increased from 20.8 % to 28.3 % and 37.9 %. On the other hand, the ratio of TiO₂ to SWCNT/Fe₃O₄ at 20:1 was found to be optimum in CA/chitosan/SWCNT/Fe₃O₄/TiO₂ (ZabihiSahebi, et al., 2019). The OH^{*} increased in concentration when increasing the content of TiO₂. Besides, inappropriate content of SWCNT/Fe₃O₄ would limit the transfer of hydrated electrons and light absorbing effect, which affects the photocatalytic performance later.

4.2.2 Dosage of Cellulose-derived Photocatalysts

In general, the photocatalytic activity or performance of a photocatalyst increases as increasing the photocatalyst dosage up to an optimum value. Above the optimum dosage, the rate of photocatalytic degradation will decrease.

Al-Kahtani, et al. (2019) reported that the degradation efficiency of BPA by ZnS-NSDC improved from 47.23 % to 95.8 % when the photocatalyst dosage increased from 0.01 g/L to 1.0 g/L. More active sites of catalysts were provided for the degradation of BPA by increasing the dosage of photocatalyst. However, photocatalytic degradation efficiency of 88 % was achieved when utilising a ZnS-NSDC dosage of 0.2 g/L, this performance was only slightly lower than 95.8 % when utilising 1.0 g/L. The results indicated that increasing the photocatalyst dosage would not further improve the catalytic performance significantly due to the unsaturated active sites. The dosage of 0.2 g/L was

selected by the authors as optimum value due to the consideration from the economic perspective.

Similarly, the optimum dosage of CNF-NiFe in the degradation of Remazol black was 0.50 g/L (Gupta, et al., 2020). The photocatalytic degradation rate was increased from 0.0324 min⁻¹ to 0.0345 min⁻¹ and decreased to 0.0302 min⁻¹ when utilising 0.25 g/L, 0.50 g/L and 0.75 g/L CNF-NiFe, respectively. This was due to the light scattering effects if utilising excessive dosage of photocatalyst. On the other hand, cellulose/CeO₂ had optimum dosage of 6 mg/L in reducing 3 ppm of Cr (VI) to Cr (III) (Zhang, et al., 2017). Cr (VI) was first reduced very rapidly at the beginning 20 minutes and slowly after that if utilising photocatalyst dosage above 6 mg/L. Hence, it can be concluded that optimum photocatalyst dosages had better overall performance than systems of very high photocatalyst dosage.

4.2.3 Initial Pollutant Concentration

In general, the cellulose-derived photocatalytic degradation performance is higher when decreasing the initial pollutant concentration. Nair, et al. (2021) reported that the initial concentration of 10 ppm Congo red in the presence of TiO₂/CA could be fully degraded within 12 hours. When the initial concentration was increased to 20 ppm and 30 ppm, degradation efficiency dropped significantly to 75 % and 65 % Congo red after 15 hours. They found out that the reactive radicals such as O₂^{·-} and OH^{*} are less available to degrade the pollutants at high pollutant concentration. This was due to the suppression of the radicals' generation when the excessive pollutants adsorb on the photocatalysts' surface (ZabihiSahebi, et al., 2019).

Zhang, et al. (2017) found that a significantly higher photocatalytic performance when treating initial concentration of Cr (VI) at 3 ppm in the presence of cellulose/CeO₂. The photocatalytic reduction performance decreased when increasing the concentration above 3 ppm. The light scattering effect by high concentration of pollutants could lead to low light harvesting by the photocatalysts. On the other hand, ZabihiSahebi, et al. (2019) found that the photocatalytic degradation of Cr (VI), As (V), MB and Congo red at initial concentration of 100 mg/L in the presence of CA/chitosan/SWCNT/Fe₃O₄/TiO₂

could achieve up to 99 % within 60 minutes. When the concentration increased to 200 mg/L, the reduction efficiency of Cr (VI) and As (V) dropped to 95 % while the degradation efficiency of MB and Congo red dropped to 85 %. The increase in pollutant concentration caused the blockage of the pores of CA/chitosan/SWCNT/Fe₃O₄/TiO₂, leading to lower rate of conversion.

4.2.4 Solution pH

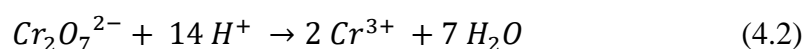
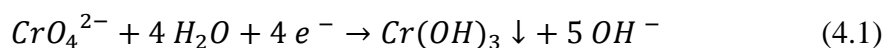
The influences of solution pH on the photocatalytic activities of cellulose-derived photocatalysts is very significant and complex. The solution pH determines the surface charges of photocatalysts, charges and chemical forms of pollutants and the availability and concentration of electrons, holes and radicals important to photocatalytic activities. In recent research of cellulose-derived photocatalysts, the variations in pH values used were largely dependent on the types of pollutants experimented and the type of degradation reaction planned to be used (Gan, et al., 2018; Zhang, et al., 2017).

For phenolic compounds, high pH solutions were commonly used. Al-Kahtani, et al. (2019) found that the optimum pH value of 9.0 happened for the degradation of BPA utilising ZnS-NSDC. The BPA degradation efficiency improved significantly when increasing the solution pH from 3.0 to 9.0. No significant increase in the photocatalytic performance was observed if the photocatalytic degradation was operated above pH 9.0. OH^{*} was the most important radical in degrading BPA and its availability increased as increasing the solution pH value. However, excessive hydroxide ion caused significant deprotonation on ZnS-NSDC surface and adsorption of BPA anion was significantly reduced due to repulsion. Hence, the degradation efficiency of BPA was limited by solution pH value.

For organic dyes, solution pH affects the photocatalytic performance mainly by affecting the surface charges and charges of the dyes in the solution. The surface charges of cellulose-derived photocatalysts can be changed according to the solution pH. The pH where the surface is neutrally charged is called zero-point charge pH (Zou, et al., 2019). Above zero-point charge pH, the catalyst surface will be negatively charged. Below zero-point charge pH, the surface will be positively charged. When the surface charge of cellulose-derived

photocatalysts is the opposite of the organic dye ions, electrostatic force of attraction exists, and adsorption will be enhanced. For instances, MB and RhB are cationic dyes and their photocatalytic degradation performances were higher in alkaline solution than in acidic solution (Nagarajan and Venkatanarasimhan, 2019; Gan, et al., 2018).

On the other hand, Cr (VI) has different forms in different pH solutions. It exists as dichromate ion ($\text{Cr}_2\text{O}_7^{2-}$) and chromate ion (CrO_4^{2-}) in acidic and alkaline solutions respectively. Equation (4.1) and Equation (4.2) show the reduction of Cr (VI) in acid and alkaline medium. The reduction of Cr (VI) to Cr (III) must be conducted in acidic solution as the product of reduction in alkaline solution, chromium (III) hydroxide ($\text{Cr}(\text{OH})_3$) was solid and would block the active sites of cellulose-derived photocatalysts (Qiu, et al., 2019). Besides, the surface charges of photocatalyst and Cr (VI) were of opposite charges at low solution pH and the adsorption was enhanced by the electrostatic attraction (Zhang, et al., 2017). Moreover, the redox potential of $\text{Cr}_2\text{O}_7^{2-}$ was 0.98 eV, which was higher than 0.24 eV of CrO_4^{2-} (Lin, et al., 2019). This indicated that the reduction of Cr (VI) could be initiated and taken place more easily in acidic environments.



4.2.5 Photocatalysis Kinetics

The photocatalytic kinetic study in the presence of cellulose-derived photocatalysts is also one of the most important studies. The photocatalytic activities could be observed quantitatively with the calculated kinetic constant and comparisons were made.

Most of the experimental data for photocatalytic degradation of organic pollutants in the presence of cellulose-derived photocatalysts fitted well into pseudo-first order (PFO) kinetic model. The kinetic model is shown in Equation (4.3). Table 4.5 shows the kinetic constants of cellulose-derived photocatalysis in recent research. The high coefficient of determination (R^2) also proved that the photocatalytic experimental data fitted into PFO kinetic.

$$\ln C_t = \ln C_0 - kt \quad (4.3)$$

where

C_t = concentration of pollutants at time t (mg/L)

C_0 = initial concentration of pollutants (mg/L)

k = PFO rate constant (min^{-1})

t = photodegradation time (min)

The PFO kinetic model was widely chosen for the modelling of cellulose-derived photocatalysis because the photocatalysis conditions fulfilled the assumption made for PFO kinetic model. The assumption made was the saturation of active sites on photocatalysts (Morales, et al., 2012). In the experiment, the concentration of pollutants used were high (Fu, et al., 2019; Gupta, et al., 2020; Nagarajan and Venkatanarasimhan, 2019). Hence, the active sites of the photocatalysts could be assumed to be fully adsorbed with pollutants. As a result, the pollutants also maintained relatively constant concentration throughout the experiment.

The validity of PFO kinetic model revealed that the adsorption of pollutants using the composite materials involved physisorption and the photocatalytic degradation rate of pollutants was proportional to the concentration of pollutants in solutions. The physisorption of pollutants on cellulose-derived photocatalysts was contributed to the hydrogen bond and Van der Waals force of attraction between the pollutants and cellulose-derived photocatalysts (Li, et al., 2016; Morshed, et al., 2020). The hydroxyl groups of cellulose formed hydrogen bond with the organic pollutants and enhanced the adsorption of pollutants on the composite materials. On the other hand, the proportionality of photocatalytic degradation rate of pollutants to the concentration of pollutants in solutions could only be valid when operating at low concentration of pollutants. This was due to the suppression of the radicals' generation when the excessive pollutants adsorb on the photocatalysts' surface (ZabihiSahebi, et al., 2019). In fact, the R^2 values of the fitting of the experimental data into PFO kinetic model dropped when increasing the

Table 4.5: Kinetic Constants of Cellulose-derived Photocatalysis in Recent Studies.

Photocatalysts	Type of Pollutants	Photocatalytic Degradation Conditions	PFO Kinetic Model		References
			k (min^{-1})	R^2	
ZnS-NSDC	BPA	Visible light; pH 7; 0.2 g/L catalyst; room temperature	0.00971	-	(Al-Kahtani, et al., 2019)
CeO ₂ /CNNS	BPA	Visible light; 50 mg/L catalyst; 50 ml of 10 mg/L BPA	0.0334	-	(Ma, et al., 2019)
Ag@CA/Fe ₂ O ₃	MO	UV; 0.05 mM MO; 5 mg catalyst; 0.5 mL of 0.1 M NaBH ₄	0.5148	-	(Bakhsh, et al., 2018)
	Nitrophenol	UV; 0.1 mM nitrophenol; 5 mg catalyst; 0.5 mL of 0.1 M NaBH ₄	0.2862	-	
NiMn ₂ O ₄ /CCF	Nitrophenol	UV-visible, 10 mg/L pollutant, 0.2 g/L catalyst, 0.1 mol/L NaBH ₄	0.3903	-	(Zhang, et al., 2017)
	MB		0.0232	-	

Table 4.5: (Continued)

Photocatalysts	Type of Pollutants	Photocatalytic Degradation Conditions	PFO Kinetic Model		References
			k (min^{-1})	R^2	
CNF-NiFe	Nitrophenol	UV; 50 eq NaBH_4 ; 100 mL of 50 mg/L nitrophenol; 50 mg catalyst	0.438	-	(Gupta, et al., 2020)
	Remazol black	UV; 50 eq NaBH_4 ; 100 mL of 50 mg/L Remazol black; 50 mg catalyst	0.0345	-	
BiOBr/RC	Phenol	Visible light; 20 mL of 7 mg/L phenol, 3 pieces of 1 cm X 2 cm BiOBr/RC	0.00445	-	(Li, et al., 2016)
ZnO-rGO	Phenol	Visible light; 0.2 g/L catalyst; pH 4; 20 ppm phenol	0.02423	0.9858	(Margaret, et al., 2021)
Cellulose/TiO₂	MB	UV; pH 7; 40 mL 50 ppm MB; 5 mg catalyst	0.188	0.985	(Morshed, et al., 2020)
Cellulose/SnS₂	RhB	Visible light; 10 mg catalyst; 50 mL 10 μM RhB	0.087	-	(Tavker and Sharma, 2020)
Cellulose/Ag₃PO₄	RhB	UV-visible; 25 mg catalyst; 25 mL 10 μM RhB	0.024	-	(Tavker, Gaur and Sharma, 2020)

Table 4.5: (Continued)

Photocatalysts	Type of Pollutants	Photocatalytic Degradation Conditions	PFO Kinetic Model		References
			k (min ⁻¹)	R ²	
CuO@CS	Acid red	UV-visible, 50 mL 40 ppm dye; 25 mg catalyst; 3.75 mL 1.5 M NaBH ₄	0.1235	0.9724	(Nagarajan and Venkatanarasimhan, 2019)
	Acid green		0.1147	0.9727	
	MB		0.1598	0.9823	
	RhB		0.0990	0.9857	
	Solochrome black		0.0244	0.9530	
AZC	Nitrophenol	UV; 0.1 mM 4-nitrophenol; 0.1 M NaBH ₄ ; 0.15 g catalyst	0.14	-	(Fu, et al., 2018)

concentration of pollutants (Ollis, 2018). Hence, it can only be concluded that the experimental data fitted the PFO kinetic model at low concentration of pollutants.

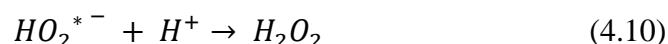
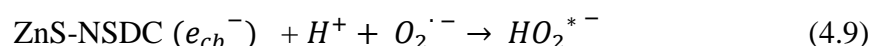
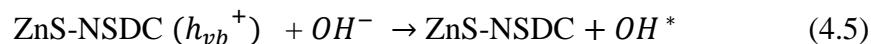
Among the cellulose-derived photocatalysts listed in Table 4.5, the photocatalytic degradation of MO in the presence of cellulose acetate-ferric oxide nanocomposite-supported silver (Ag@CA/Fe₂O₃) had the highest k value of 0.5148 min⁻¹. Bakhsh, et al. (2018) reported that this was due to the low initial pollutant concentration of 0.05 mM MO, high photocatalyst dosage of 5 mg and high amount of 0.1 M NaBH₄. All the parameters were optimum for the high photocatalytic activity to be achievable. Besides, the utilisations of NaBH₄ had significant effect on the kinetic rates. For instances, the photocatalytic degradation of nitrophenol and organic dyes in the presence of Ag@CA/Fe₂O₃, NiMn₂O₄/CCF, CNF-NiFe, CuO@CS and AZC with NaBH₄ as reducing agent and electron donor had the higher k values than the photocatalytic degradation without NaBH₄. NaBH₄ provided electrons to the photocatalytic reaction and boosted the formation of radicals, which effectively speeded up the rate of photocatalysis (Zhang, et al., 2017). For photocatalytic degradation with no addition of NaBH₄, the photocatalytic degradation of MB in the presence of cellulose/TiO₂ had the highest k value of 0.188 min⁻¹ (Morshed, et al., 2020). High k value was due to the excellent radicals' generation capacity by TiO₂ photocatalyst and operated at low initial MB concentration of 50 ppm.

4.3 Mechanisms

The mechanisms of the photocatalytic degradation of pollutants are also one of the most important studies in cellulose-derived photocatalysts. The mechanisms are often suggested by researchers after conducting scavenger tests to determine the types of molecules that are responsible for the photocatalytic degradations.

The photocatalytic degradations of phenolic compounds by cellulose-derived photocatalysts were mainly by species O₂^{·-} and OH^{*} (Li, et al., 2016; Mu, et al., 2017). The full mechanisms of BPA degradation by ZnS-NSDC are shown from Equation (4.4) to Equation (4.11) (Al-Kahtani, et al., 2019). Firstly, the charge separation of electrons in conduction band (e_{cb}^-) and holes in valence band (h_{vb}^+) occurred upon light radiation. Then OH^{*} was formed from

either oxidation of OH^- or water molecules. $\text{O}_2^{\cdot-}$ was formed from reaction of O_2 with free electrons on the photocatalyst surface. Lastly, BPA was degraded by the reactive radicals.

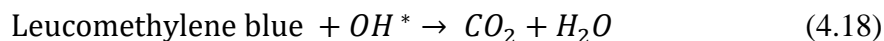
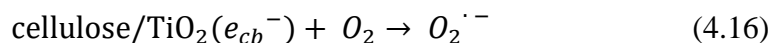
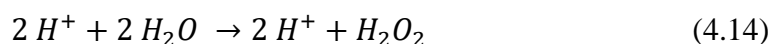
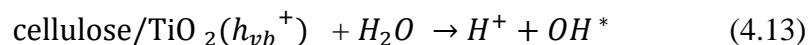


Gupta, et al. (2020) reported that the role of O_2 as the electron acceptor was important to degrade organic pollutant. O_2 consumed electrons and hence prevented the recombination of charges. The addition of the optimum amount of hydrogen peroxide could act as the electron acceptor to increase the concentration of $\text{O}_2^{\cdot-}$ (Al-Kahtani, et al., 2019; Mu, et al., 2017).

Figure 4.4 shows the photocatalytic degradation pathways of BPA in the presence of ZnS-NSDC. Firstly, OH^* attacked BPA at the symmetrical phenyl rings (Al-Kahtani, et al., 2019; Li, et al., 2016). The possible intermediates formed were isopropyl phenol and phenolic hydroxyl groups. When the carbon between the aromatic rings of BPA was attacked, isopropyl alcohol was formed. Meanwhile, when the ortho or para position of the aromatic rings was attacked, phenolic hydroxyl groups were formed. The intermediates were then involved in ring opening reactions and mineralised into carbon dioxide and water.

the BH_4^- electron donor ions once the ions were adsorbed onto the surface of the photocatalysts. The electrons then reacted with the nitro group of nitrophenol and promoted the reduction to amine group, forming aminophenol. The aminophenol was the desired final product of degradation of nitrophenol through photocatalytic reduction (Bakhsh, et al., 2018).

Similar to BPA, $O_2^{\cdot-}$ and OH^* were also the predominant species to interact and degrade the organic dyes (Nagarajan and Venkatanarasimhan, 2019). Equation (4.12) to Equation (4.18) and Figure 4.5 show the photocatalytic degradation mechanisms of MB in the presence of cellulose/ TiO_2 (Morshed, et al., 2020). OH^* were responsible for the photocatalytic degradation of MB into the colourless intermediate of Leucomethylene blue. Leucomethylene blue was then further degraded into carbon dioxide and water. The photocatalytic degradation of RhB using cellulose-supported Tb_2CoMnO_6 (Tb_2CoMnO_6 /cellulose) and cellulose/ SnS_2 also had the similar mechanisms and final products (Dara, et al., 2021; Tavker and Sharma, 2020). RhB would be degraded into phthalic acid as intermediates before being converted to carbon dioxide and water (Gan, et al., 2020).



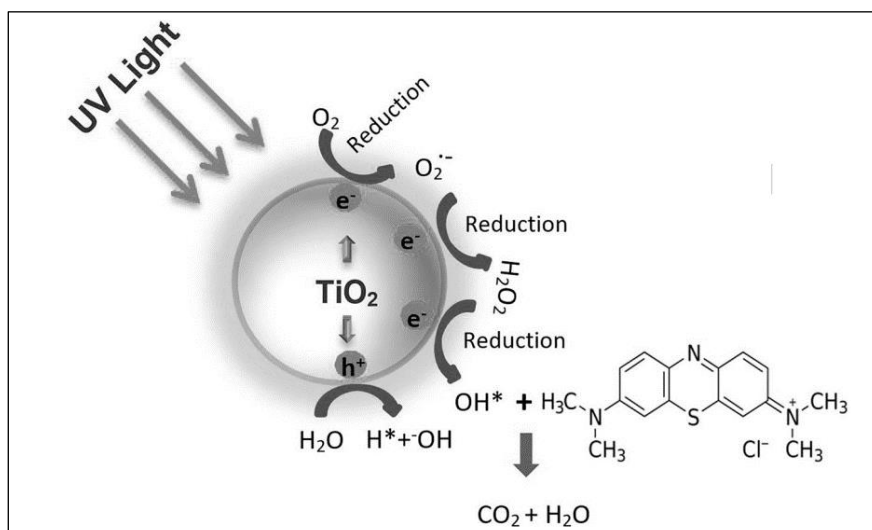
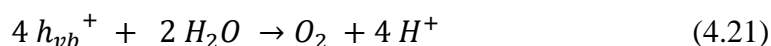


Figure 4.5: Degradation Mechanism of MB Using Cellulose/TiO₂ (Morshed, et al., 2020).

On the other hand, the photocatalytic reduction of Cr (VI) to Cr (III) utilised the electrons formed at the cellulose-derived photocatalyst surface and H⁺ in the solution (ZabihiSahebi, et al., 2019). The mechanism of reducing Cr (VI) to Cr (III) using CNF/ZnIn₂S₄ are shown from Equation (4.19) to Equation (4.21) and Figure 4.6 (Qiu, et al., 2019). As electrons were used up in the reduction, water molecules acted as holes acceptors and formed O₂ and H⁺. The mechanism was the same for Cr (VI) reduction using cellulose/CeO₂ and cellulose/MoS₂ (Lin, et al., 2019; Zhang, et al., 2017).



In the simultaneous photodegradation of RhB and Cr (VI) using BiOBr/CCNF, RhB and Cr (VI) acted as the hole and electron acceptors, respectively (Gan, et al., 2020). Once h_{vb}^+ and e_{cb}^- were generated upon light radiation, H⁺ and e_{cb}^- reduced Cr (VI) to Cr (III). On the other hand, h_{vb}^+ bonded with RhB and took part in the RhB degradation reactions. In the cases where there was only RhB present in the solution, e_{cb}^- would directly convert O₂ to O₂⁻ (Dara, et al., 2021). In the simultaneous photodegradation of RhB

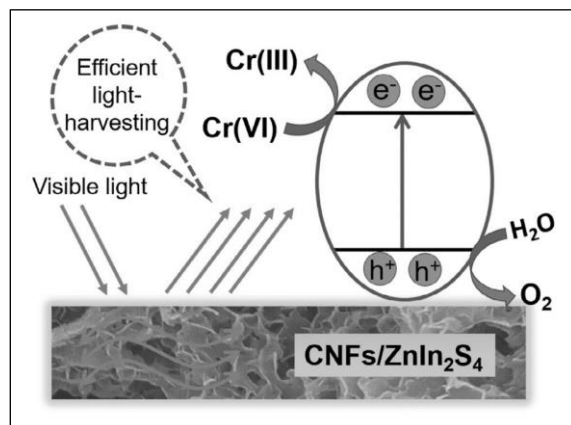


Figure 4.6: Photocatalytic Reduction of Cr (VI) to Cr (III) using CNF/ZnIn₂S₄ (Qiu, et al., 2019).

and Cr (VI), e_{cb}^- would first reduce Cr (VI) to Cr (III) before converting O₂ to O₂^{•-} to degrade RhB (Lin, et al., 2019).

CHAPTER 5

CONCLUSIONS AND RECOMMENDATIONS

5.1 Conclusions

Overall, cellulose-derived photocatalyst demonstrated high photocatalytic activity due to the synergistic effect of combining cellulose with semiconductors. The synergistic effect included increment in active sites, decrement in charge transport distance and more efficient light harvesting of the photocatalysts.

Based on the SEM micrographs the cellulose-derived photocatalysts had many different forms, sizes and surface morphologies due to the wide variety of cellulose-derived materials and semiconductors incorporated. The semiconductor demonstrated a smaller size, less agglomeration and greater dispersion when compositing with cellulose than in their individual forms. Next, FTIR analysis had confirmed the successful integrations of materials and the retainment of materials' original characteristics. It was found that chemical bonds, hydrogen bonds and physical bindings were existed between the materials in cellulose-derived photocatalysts. Next, the XPS spectra had confirmed only the desired types of elements and chemical states were incorporated into the cellulose-derived photocatalysts. In addition, XRD analyses had confirmed the crystallinity structure of the cellulose-derived photocatalysts. Lastly, TGA results had showed that the cellulose-derived photocatalysts possessed high thermal stability and could operate well under usual photocatalysis temperature.

The photocatalytic activities of cellulose-derived photocatalysts increased as increasing the amount of cellulose in the composite materials up to an optimum value. The increment of cellulose amount enhanced the synergistic effect of the composites such as increasing adsorptivity, active sites, decreasing charge transport distance and more efficient light-harvesting. Further increment of the cellulose amount caused the shading effects and less light penetration. Next, the photocatalytic activities increased as increasing the amount of semiconductor in the composite materials up to an optimum value as more radicals were available. The agglomeration of semiconductor, increment of

recombination sites and light blocking caused the drop of photocatalytic activities if exceeded the optimum amount of semiconductor in composite materials. Moreover, the photocatalytic activities also increased as increasing the dosage of cellulose-derived photocatalysts up to an optimum value as more active sites were available. Above the optimum dosage value, the photocatalysts caused turbidity and light scattering that lowered the photocatalytic activities. On the other hand, the lower the initial pollutant concentration, the higher the photocatalytic activities. This was due to the higher availability of reactive radicals for the pollutants when dealing with low pollutant concentration. Besides, it was found that high solution pH boosted the photodegradation of nitrophenol, BPA, MB and RhB. On the other hand, Cr (VI) was degraded effectively at low solution pH. In addition, the photocatalytic degradation of pollutants in the presence of cellulose-derived photocatalysts fitted to PFO kinetic model with high R^2 values.

For the mechanisms involved in the photodegradation of pollutants, BPA, MB and RhB were degraded by the reactive radicals of OH^* and $\text{O}_2^{\cdot-}$ into intermediate products, before undergoing ring opening reactions and mineralisation into carbon dioxide and water. On the other hand, BPA was degraded by photo-generated electrons with reducing agent NaBH_4 . Lastly, Cr (VI) was photocatalytic reduced by H^+ , into Cr (III). Then, Cr (III) could be totally removed by precipitation in alkaline solution.

As a conclusion, all the research objectives were achieved. The recently developed cellulose-derived photocatalysts demonstrated excellent degradation abilities towards phenolic compounds, organic dyes and heavy metals. Hence, cellulose-derived composites were proven to be promising photocatalysts for the removal of water pollutants.

5.2 Recommendations for Future Work

The wide applications of biomass-derived cellulose in various fields face bottlenecks in pre-treatments and extractions such as expensive, large quantity of waste being generated and high energy consumption. Furthermore, the overall published works of cellulose-derived photocatalytic degradation of water pollutants were limited. Besides, most of the recent studies of cellulose-

derived catalyst focused on water pollutants removal by adsorption rather than photocatalysis. The current studies of cellulose-derived photocatalysis are mostly based on synthetic pollutants. The study of photocatalytic degradation of industrial wastewater is not widely conducted currently. Some of the data from different journals were found to be investigated at different experiment conditions as operated by different researchers. Hence, there are some recommendations that can be made for future studies.

The future studies can aim to implement improved schemes to pre-treat and extract cellulose effectively. Furthermore, regeneration studies of the developed cellulose-derived photocatalysts can be performed on other different water pollutants and real industrial wastewater. Lastly, the procedures of the recent studies can be modified to be carried under same conditions in order to obtain more comparable results.

REFERENCES

- Abdelhamid, H.N. and Mathew, A.P., 2022. Cellulose–metal organic frameworks (CelloMOFs) hybrid materials and their multifaceted applications. *Coordination Chemistry Reviews*, 451, pp.214263.
- Abrile, M.G., Ciucio, M.M. Demarchi, L.M., Bono, V.M., Fiasconaro, M.L. and Lovato, M.E. 2021. Degradation and mineralization of the emerging pharmaceutical pollutant sildenafil by ozone and UV radiation using response surface methodology. *Environmental Science and Pollution Research (international)*, 28(19), pp.23868-23886.
- Ahamad, T., Naushad, M., Ruksana, Alhabarah, A.N. and Alshehri, S.M., 2019. N/S doped highly porous magnetic carbon aerogel derived from sugarcane bagasse cellulose for the removal of bisphenol-A. *International Journal of Biological Macromolecules*, 132, pp.1031–1038.
- Ain, Q.U., Farooq, M.U. and Jalees, M.I., 2020. Application of magnetic graphene oxide for water purification: heavy metals removal and disinfection. *Journal of Water Process Engineering*, 33, pp.101044.
- Al-Kahtani, A.A., Alshehri, S.M., Naushad, M., Ruksana and Ahamad, T., 2019. Fabrication of highly porous N/S doped carbon embedded with ZnS as highly efficient photocatalyst for degradation of bisphenol. *International Journal of Biological Macromolecules*, 121, pp.415–423.
- Andreou, V., Dimopoulos, G., Dermesonlouoglou, E. and Taoukis, P., 2020. Application of pulsed electric fields to improve product yield and waste valorization in industrial tomato processing. *Journal of Food Engineering*, 270, pp.109778.
- Anku, W.W., Mamo, M.A. and Govender, P.P., 2017. *Phenolic compounds in water: sources, reactivity, toxicity and treatment methods*. London: IntechOpen.
- Armeanu, A., David, E. and Badescu, V., 2019. Mechanical and thermal pre-treatment of biomass for the thermochemical conversion. *UPB Scientific Bulletin, Series D: Mechanical Engineering*, 81(3), pp.213–224.
- Arnata, I.W., Suprihatin, S., Fahma, F., Richana, N. and Candra Sunarti, T., 2019. Cellulose production from sago frond with alkaline delignification and bleaching on various types of bleach agents. *Oriental Journal of Chemistry*, 35(1), pp.8–19.
- Ashter, S.A., 2018. *Technology and applications of polymers derived from biomass*. Massachusetts: Elsevier.
- Bai, Q., Xiong, Q., Li, C., Shen, Y. and Uyama, H., 2017. Hierarchical porous cellulose/activated carbon composite monolith for efficient adsorption of dyes. *Cellulose*, 24(10), pp.4275–4289.

Balasurya, S., Syed, A., Thomas, A.M., Bahkali, A.H., Al-Rashed, S., Elgorban, A.M., Raju, L.L., Das, A. and Khan, S.S., 2020. Preparation of Ag-cellulose nanocomposite for the selective detection and quantification of mercury at nanomolar level and the evaluation of its photocatalytic performance. *International Journal of Biological Macromolecules*, 164, pp.911–919.

Bakhsh, E.M., Khan, S.A., Marwani, H.M., Danish, E.Y., Asiri, A.M. and Khan, S.B., 2018. Performance of cellulose acetate-ferric oxide nanocomposite supported metal catalysts toward the reduction of environmental pollutants. *International Journal of Biological Macromolecules*, 107, pp.668–677.

Borjesson, M. and Westman, G., 2015. *Crystalline nanocellulose — preparation, modification, and properties*. London: IntechOpen.

Boroujeni, K.P. and Tahani, P., 2017. The cellulose aluminum oxide composite-supported imidazolium chloroaluminate ionic liquid as a novel and stable heterogeneous catalyst. *Inorganic and Nano-Metal Chemistry*, 47(8), pp.1150–1156.

Campbell, T., Bals, B., Teymouri, F., Glassbrook, J., Nielson, C., Videto, J., Rinard, A., Moore, J., Julian, A. and Bringi, V., 2020. Scale-up and operation of a pilot-scale ammonia fiber expansion reactor. *Biotechnology and Bioengineering*, 117(4), pp.1241–1246.

Caputo, D., Fusco, C., Nacci, A., Palazzo, G., Murgia, S., D'Accolti, L. and Gentile, L., 2021. A selective cellulose/hemicellulose green solvents extraction from buckwheat chaff. *Carbohydrate Polymer Technologies and Applications*, 2, pp.100094.

Chen, D., Cheng, Y., Zhou, N., Chen, P., Wang, Y., Li, K., Huo, S., Cheng, P., Peng, P., Zhang, R., Wang, L., Liu, H., Liu, Y. and Ruan, R., 2020. Photocatalytic degradation of organic pollutants using TiO₂-based photocatalysts. *Journal of Cleaner Production*, 268, pp.121725.

Chen, P.C., Chiu, M.C. and Ma, H.W., 2016. Measuring the reduction limit of repeated recycling – a case study of the paper flow system. *Journal of Cleaner Production*, 132, pp.98–107.

Chang, N., Chen, Y.R., Xie, F., Liu, Y.P. and Wang, H.T., 2021. Facile construction of Z-scheme AgCl/Ag-doped-ZIF-8 heterojunction with narrow band gaps for efficient visible-light photocatalysis. *Colloids and Surfaces A: Physicochemical and Engineering Aspects*, 616, pp.126351.

Chowdhury, S., Mazumder, M. A. J., Al-Attas, O., and Husain, T., 2016. Heavy metals in drinking water: Occurrences, implications, and future needs in developing countries. *Science of The Total Environment*, 569-570, pp.476–488.

Chowdhury, Z.Z., Chandran, R.R.R., Jahan, A., Khalid, K., Rahman, M.M., Al-Amin, M., Akbarzadeh, O., Badruddin, I.A., Khan, T.M.Y., Kamangar, S., Hamizi, N.A., Abdul Wahab, Y., Johan, R. and Adebisi, G.A., 2019. Extraction of cellulose nano-whiskers using ionic mathematical modelling using box – behnken design. *Symmetry*, 11, pp.1–20.

Dara, M., Hassanpour, M., Amiri, O., Baladi, M. and Salavati-Niasari, M., 2021. $\text{Tb}_2\text{CoMnO}_6$ double perovskites nanoparticles as photocatalyst for the degradation of organic dyes: synthesis and characterization. *Arabian Journal of Chemistry*, 14(10), pp.103349.

Descals, A., Wich, S., Meijaard, E., Gaveau, D.L.A., Peedell, S. and Szantoi, Z., 2021. High-resolution global map of smallholder and industrial closed-canopy oil palm plantations. *Earth System Science Data*, 13(3), pp.1211–1231.

Department of Environment of Malaysia (DOE), 2017. *Environmental quality report 2017*. [online] Available at: <<https://www.doe.gov.my/portalv1/wp-content/uploads/2018/09/Kualiti-Air-Sungai.pdf>> [Accessed 13 June 2021].

Department of Environment of Malaysia (DOE), 2021. *Water classes and uses*. [online] Available at: <<https://www.doe.gov.my/portalv1/wp-content/uploads/2019/05/Standard-Kualiti-Air-Kebangsaan.pdf>> [Accessed 13 June 2021].

Dini, F.W., Helmiyati, H. and Krisnandi, Y.K., 2021. Cellulose and $\text{TiO}_2\text{-ZrO}_2$ nanocomposite as a catalyst for glucose conversion to 5-EMF. *Bulletin of Chemical Reaction Engineering & Catalysis*, 16(2), pp.320–330.

Ejaz, U., Muhammad, S., Ali, F.I., Hashmi, I.A. and Sohail, M., 2020. Cellulose extraction from methyltrioctylammonium chloride pretreated sugarcane bagasse and its application. *International Journal of Biological Macromolecules*, 165, pp.11–17.

Elhacham, E., Ben-Uri, L., Grozovski, J., Bar-On, Y.M. and Milo, R., 2020. Global human-made mass exceeds all living biomass. *Nature*, 588, pp.442–444.

Firouzjaei, M.D., Akbari Afkhami, F., Rabbani Esfahani, M., Turner, C.H. and Nejati, S., 2020. Experimental and molecular dynamics study on dye removal from water by a graphene oxide-copper-metal organic framework nanocomposite. *Journal of Water Process Engineering*, 34, pp.101180.

Fu, F., Gu, J., Zhang, R., Xu, X., Yu, X., Liu, L., Liu, X., Zhou, J. and Yao, J., 2018. Three-dimensional cellulose based silver-functionalized ZnO nanocomposite with controlled geometry: Synthesis, characterization and properties. *Journal of Colloid and Interface Science*, 530, pp.433–443.

Gan, L., Geng, A., Song, C., Xu, L., Wang, L., Fang, X., Han, S., Cui, J. and Mei, C., 2020. Simultaneous removal of rhodamine B and Cr(VI) from water using cellulose carbon nanofiber incorporated with bismuth oxybromide: The effect of cellulose pyrolysis temperature on photocatalytic performance. *Environmental Research*, 185, pp.109414.

Gan, L., Zhong, Q., Geng, A., Wang, L., Song, C., Han, S., Cui, J. and Xu, L., 2019. Cellulose derived carbon nanofiber: a promising biochar support to enhance the catalytic performance of CoFe_2O_4 in activating peroxydisulfate for recycled dimethyl phthalate degradation. *Science of the Total Environment*, 694, pp.133705.

Gatenholm, P. and Tenkanen, M., 2003. *Hemicelluloses: science and technology*. Washington: American Chemical Society.

Ghaemi, F. and Amiri, A., 2020. Microcrystalline cellulose/metal–organic framework hybrid as a sorbent for dispersive micro-solid phase extraction of chlorophenols in water samples. *Journal of Chromatography A*, 1626, pp.1-7.

Ghosh, D., Tanner, J., Lavoie, J.M., Garnier, G. and Patti, A.F., 2021. An integrated approach for hemicellulose extraction from forest residue. *Bioresources*, 16(2), pp.2524–2547.

Ghosh, S., 2018. *Visible-light-active photocatalysis: nanostructured catalyst design, mechanisms and applications*. Weinheim: Wiley.

Glazer, A.N. and Nikaido, H., 1995. *Microbial biotechnology: fundamentals of applied microbiology*. New York: Freeman.

Glińska, K., Lerigoleur, C., Giralt, J., Torrens, E. and Bengoa, C., 2020. Valorization of cellulose recovered from wwtp sludge to added value levulinic acid with a brønsted acidic ionic liquid. *Catalysts*, 10(9), pp.1–16.

Gopalakrishnan, A., Singh, S.P. and Badhulika, S., 2020. Reusable, few-layered-MoS₂ nanosheets/graphene hybrid on cellulose paper for superior adsorption of methylene blue dye. *New Journal of Chemistry*, 44(14), pp.5489–5500.

Gopi, S., Amalraj, A., Jude, S., Benson, K.T., Balakrishnan, P., Haponiuk, J.T. and Thomas, S., 2019. Isolation and characterization of stable nanofiber from turmeric spent using chemical treatment by acid hydrolysis and its potential as antimicrobial and antioxidant activities. *Journal of Macromolecular Science, Part A: Pure and Applied Chemistry*, 56(4), pp.327–340.

Gupta, K., Kaushik, A., Tikoo, K.B., Kumar, V. and Singhal, S., 2020. Enhanced catalytic activity of composites of NiFe₂O₄ and nano cellulose derived from waste biomass for the mitigation of organic pollutants. *Arabian Journal of Chemistry*, 13(1), pp.783–798.

Hafid, H.S., Omar, F.N., Zhu, J. and Wakisaka, M., 2021. Enhanced crystallinity and thermal properties of cellulose from rice husk using acid hydrolysis treatment. *Carbohydrate Polymers*, 260, pp.117789.

Hamzavi, S.F., Gerivani, S., Saeedi, S., Naghdipari, K. and Shahverdizadeh, G., 2020. Preparation and characterization of a novel spherical cellulose–copper(II) oxide composite particles: as a heterogeneous catalyst for the click reaction. *Molecular Diversity*, 24(1), pp.201–209.

Hendrawan, Y., Sabrinauly, Hawa, L.C., Rachmawati, M. and Argo, B.D., 2019. Analysis of the phenol and flavonoid content from basil leaves (*Ocimum americanum* L) extract using pulsed electric field (PEF) pre-treatment. *Agricultural Engineering International: CIGR Journal*, 21(2), pp.149–158.

Hindi, S.S.Z., 2017. The interconvertibility of cellulose's allomorphs. *BioCrystal Journal*, 1(11), pp.1–12.

- Hinestroza J.P. and Netravali, A.N., 2014. *Cellulose based composites*. Weinheim: Wiley.
- Hou, L., Ji, D., Dong, W., Yuan, L., Zhang, F., Li, Y. and Zang, L., 2020. The synergistic action of electro-fenton and white-rot fungi in the degradation of lignin. *Frontiers in Bioengineering and Biotechnology*, 8, pp.1–11.
- Indira, T.I., Burhan, K.H., Manurung, R. and Widiana, A., 2020. Enhancement of essential oil yield from *Melaleuca leucadendra* L. leaves by lignocellulose degradation pre-treatment using filamentous fungi. *Journal of Bioresources and Bioproducts I*, 2020, pp.1–14.
- Ivan, R., Tussupova, K., Klemes, J.J. and Persson, K.M., 2021. Oil refinery and water pollution in the context of sustainable development: Developing and developed countries. *Journal of Cleaner Production*, 302, pp.126987.
- Javanbakht, S., Mohammadian, R., Farhid, H., Shaabani, A. and Amini, M.M., 2021. A green, reusable and remarkable catalyst for selective aerobic oxidation of alcohols: Construction of Cu(BDC) on the surface of carboxymethyl cellulose fiber. *Materials Today Communications*, 28(5), pp.102502.
- Joubert, A.J., Chimphango, A.F.A. and Görgens, J.F., 2016. Effect of integrating xylan extraction from *e. grandis* into the kraft pulping process on pulp yield and chemical balance. *BioResources*, 11(1), pp.2417–2437.
- Joy, J., Jose, C., Mathew, P.L., Thomas, S. and Khalaf, M.N., 2015. *Biological delignification of biomass*. New York: Apple Academic Press.
- Jung, S.J., Kim, S.H. and Chung, I.M., 2015. Comparison of lignin, cellulose, and hemicellulose contents for biofuels utilization among 4 types of lignocellulosic crops. *Biomass and Bioenergy*, 83, pp.322–327.
- Kalia, S., Kaith, B.S. and Kaur, I., 2011. *Cellulose fibers: bio- and nano-polymer composites green chemistry and technology*. Berlin: Springer.
- Kandasamy, M., Hamawand, I., Bowtell, L., Seneweera, S., Chakrabarty, S., Yusaf, T., Shakoor, Z., Algayyim, S. and Eberhard, F., 2017. Investigation of ethanol production potential from lignocellulosic material without enzymatic hydrolysis using the ultrasound technique. *Energies*, 10(1), pp.1-13.
- Kapelewska, J., Kotowska, U., Karpinska, J., Astel, A., Zielinski, P., Suchta, J. and Algryzm, K., 2019. Water pollution indicators and chemometric expertise for the assessment of the impact of municipal solid waste landfills on groundwater located in their area. *Chemical Engineering Journal*, 359, pp.790-800.
- Kargarzadeh, H., Ahmad, I. and Thomas, S., 2017. *Handbook of cellulose nanocomposites*. Weinheim: Wiley.
- Keller, D.H., Zelanko, P.M., Gagnon, J.E., Horwitz, R.J., Galbraith, H.S. and Velinsky, D.J., 2018. Linking otolith microchemistry and surface water contamination from natural gas mining. *Environmental Pollution*, 240, pp.457-465.

- Khalid, K.A., Ahmad, A.A. and Yong, T.L.-K., 2017. Lignin extraction from lignocellulosic biomass using sub- and supercritical fluid technology as precursor for carbon fiber production. *Journal of the Japan Institute of Energy*, 96(8), pp.255–260.
- Kim, J.H., Choi, J.H., Kim, J.C., Jang, S.K., Kwak, H.W., Koo, B. and Choi, I.G., 2021. Production of succinic acid from liquid hot water hydrolysate derived from quercus mongolica. *Biomass and Bioenergy*, 150, pp.106103.
- Kim, M., Lee, S.Y., Yoo, S.M., Paek, S.H., Lee, Y.H., Cho, K.T., Zimmermann, I., Kim, H.Y., Lim, B.S., Song, M.K., Shin, T.H., Kim, K.S., Huckaba, A.J., Nazeeruddin, M.K. and Lee, H.J., 2020. Effective preparation of nanoscale $\text{CH}_3\text{NH}_3\text{PbI}_3$ perovskite photosensitizers for mesoporous TiO_2 -based solar cells by successive precursor layer adsorption and reaction process. *Energy Technology*, 8(4), pp.1901186.
- Kol, H.S. and Cayır, B., 2021. Increasing the impregnability of oriental spruce wood via microwave pretreatment. *BioResources*, 16(2), pp.2513–2523.
- Kumar, R., Butreddy, A., Kommineni, N., Guruprasad Reddy, P., Bunekar, N., Sarkar, C., Dutt, S., Mishra, V.K., Aadil, K.R., Mishra, Y.K., Oupicky, D. and Kaushik, A., 2021. Lignin: drug/gene delivery and tissue engineering applications. *International Journal of Nanomedicine*, 16, pp.2419–2441.
- Lau, K.K., Jawaid, M., Ariffin, H. and Karim, Z., 2018. Isolation and characterization of nanocrystalline cellulose from roselle-derived microcrystalline cellulose. *International Journal of Biological Macromolecules*, 114, pp.54–63.
- Lellis, B., Fávaro-Polonio, C.Z., Pamphile, J.A. and Polonio, J.C., 2019. Effects of textile dyes on health and the environment and bioremediation potential of living organisms. *Biotechnology Research and Innovation*, 3(2), pp.275–290.
- Li, C., Wang, L., Chen, Z., Li, Y., Luo, X. and Zhao, F., 2021. Ozonolysis of wheat bran in subcritical water for enzymatic saccharification and polysaccharide recovery. *Journal of Supercritical Fluids*, 168, pp.105092.
- Li, S., Hao, X., Dai, X. and Tao, T., 2018. Rapid photocatalytic degradation of pollutant from water under UV and sunlight via cellulose nanofiber aerogel wrapped by TiO_2 . *Journal of Nanomaterials*, 18, pp.8752015.
- Li, Q., Zhou, D., Zhang, P., Man, P., Tian, Z., Li, Y. and Ai, S., 2016. The BiOBr/regenerated cellulose composite film as a green catalyst for light degradation of phenol. *Colloids and Surfaces A: Physicochemical and Engineering Aspects*, 501, pp.132–137.
- Lin, C., Liu, Y., Su, Q., Liu, Y., Lv, Y. and Liu, M., 2019. One-pot synthesis of cellulose/ MoS_2 composite for efficient visible-light photocatalytic reduction of Cr(VI). *BioResources*, 14(3), pp.6114–6133.

- Lin, X., Guo, L., Shaghaleh, H., Hamoud, Y.A., Xu, X. and Liu, H., 2021. A TEMPO-oxidized cellulose nanofibers/MOFs hydrogel with temperature and pH responsiveness for fertilizers slow-release. *International Journal of Biological Macromolecules*, 191(9), pp.483–491.
- Lu, J., Song, F., Liu, H., Chang, C., Cheng, Y. and Wang, H., 2021. Production of high concentration bioethanol from reed by combined liquid hot water and sodium carbonate-oxygen pretreatment. *Energy*, 217, pp.119332.
- Lu, S., Liu, J.Y. and Ge, J.W., 2021. Dynamic game in agriculture and industry cross-sectoral water pollution governance in developing countries. *Agricultural Water Management*, (243), pp.106417.
- Ma, R., Zhang, S., Li, L., Gu, P., Wen, T., Khan, A., Li, S., Li, B., Wang, S. and Wang, X., 2019. Enhanced visible-light-induced photoactivity of type-II CeO₂/g-C₃N₄ nanosheet toward organic pollutants degradation. *ACS Sustainable Chemistry and Engineering*, 7(10), pp.9699–9708.
- Margaret, S.M., Paul Winston, A.J.P., Muthupandi, S., Shobha, P. and Sagayaraj, P., 2021. Enhanced photocatalytic degradation of phenol using urchin-like zno microrod-reduced graphene oxide composite under visible-light irradiation. *Journal of Nanomaterials*, 2021, pp.1–11.
- Moayedi, H., Aghel, B., Abdullahi, M.M., Nguyen, H. and Safuan A Rashid, A., 2019. Applications of rice husk ash as green and sustainable biomass. *Journal of Cleaner Production*, 237, pp.117851.
- Mongkhonsiri, G., Anantpinijwatna, A., Charoensuppanimit, P., Arpornwichanop, A., Gani, R. and Assabumrungrat, S., 2021. Novel biorefinery-integrated-kraft-pulping network for sustainable development. *Chemical Engineering and Processing - Process Intensification*, 163, pp.108373.
- Mor, P., Bals, B., Tyagi, A.K., Teymouri, F., Tyagi, N., Kumar, S., Bringi, V. and VandeHaar, M., 2018. Effect of ammonia fiber expansion on the available energy content of wheat straw fed to lactating cattle and buffalo in India. *Journal of Dairy Science*, 101(9), pp.7990–8003.
- Morales, G. V., Sham, E.L., Cornejo, R. and Farfan Torres, E.M., 2012. Kinetic studies of the photocatalytic degradation of tartrazine. *Latin American Applied Research*, 42(1), pp.45–49.
- Morodi, T.J. and Mpofu, C., 2018. Environmental decision making on acid mine drainage issues in South Africa: an argument for the precautionary principle. *Science and Engineering Ethics*, 24(4), pp.1181-1199.
- Morshed, M.N., Al Azad, S., Deb, H., Shaun, B.B. and Shen, X.L., 2020. Titania-loaded cellulose-based functional hybrid nanomaterial for photocatalytic degradation of toxic aromatic dye in water. *Journal of Water Process Engineering*, 33, pp.101062.

Mu, C., Zhang, Y., Cui, W., Liang, Y. and Zhu, Y., 2017. Removal of bisphenol A over a separation free 3D Ag₃PO₄-graphene hydrogel via an adsorption-photocatalysis synergy. *Applied Catalysis B: Environmental*, 212, pp.41–49.

Nagarajan, D. and Venkatanarasimhan, S., 2019. Copper(II) oxide nanoparticles coated cellulose sponge—an effective heterogeneous catalyst for the reduction of toxic organic dyes. *Environmental Science and Pollution Research*, 26(22), pp.22958–22970.

Nair, A.K., Roy George, D., Jos Baby, N., Reji, M. and Joseph, S., 2021. Solar dye degradation using TiO₂ nanosheet based nanocomposite floating photocatalyst. *Materials Today: Proceedings*, 46, pp.2747–2751.

National Research Council, 2012. *The role of the chemical sciences in finding alternatives to critical resources: a workshop summary*. Washington (DC): National Academies Press (US).

Ng, H.K.M. and Leo, C.P., 2019. Translucent and adsorptive PVA thin film containing microfibrillated cellulose intercalated with TiO₂ nanoparticles for dye removal. *Colloids and Surfaces A: Physicochemical and Engineering Aspects*, 578, pp.123590.

Niakan, M., Masteri-Farahani, M., Shekaari, H. and Karimi, S., 2021. Pd supported on clicked cellulose-modified magnetite-graphene oxide nanocomposite for C-C coupling reactions in deep eutectic solvent. *Carbohydrate Polymers*, 251, pp.117109.

Olajuyin, A.M., Yang, M., Mu, T., Tian, J., Thygesen, A., Abidemi, O., Oluwatosin, A., Adaramoye, A., Song, A. and Xing, J., 2018. Enhanced production of succinic acid from methanol – organosolv pretreated strophanthus preussii by recombinant escherichia coli. *Bioprocess and Biosystems Engineering*, 41, pp.1497–1508.

Ollis, D.F., 2018. Kinetics of photocatalyzed reactions: five lessons learned. *Frontiers in Chemistry*, 6(AUG), pp.1–7.

Omran, A.A.B., Mohammed, A.A.B.A., Sapuan, S.M., Ilyas, R.A., Asyraf, M.R.M., Kooloor, S.S.R. and Petru, M., 2021. Micro-and nanocellulose in polymer composite materials. *Polymers*, 13(2), pp.1–30.

Onwumere, J., Piątek, J., Budnyak, T., Chen, J., Budnyk, S., Karim, Z., Thersleff, T., Kuśtrowski, P., Mathew, A.P. and Slabon, A., 2020. Celluphot: hybrid cellulose-bismuth oxybromide membrane for pollutant removal. *ACS Applied Materials and Interfaces*, 12(38), pp.42891–42901.

Ortega, J.O., Mora Vargas, J.A., Metzker, G., Gomes, E., da Silva, R. and Boscolo, M., 2021. Enhancing the production of the fermentable sugars from sugarcane straw: A new approach to applying alkaline and ozonolysis pretreatments. *Renewable Energy*, 164, pp.502–508.

Papoutsis, K. and Edelenbos, M., 2021. Postharvest environmentally and human-friendly pre-treatments to minimize carrot waste in the supply chain caused by physiological disorders and fungi. *Trends in Food Science and Technology*, 112, pp.88–98.

Pei, Y., Li, Z., Xu, W., Song, C., Li, J. and Song, F., 2021. Effects of ultrasound pretreatment followed by far-infrared drying on physicochemical properties, antioxidant activity and aroma compounds of saffron (*Crocus sativus* L.). *Food Bioscience*, 42, pp.101186.

Perrone, O.M., Moretti, M.M. de S., Bordignon, S.E., Pereira, J. de C., da Silva, R., Gomes, E. and Boscolo, M., 2021. Improving cellulosic ethanol production using ozonolysis and acid as a sugarcane biomass pretreatment in mild conditions. *Bioresource Technology Reports*, 13, pp.100628.

Pica, M., 2021. Treatment of wastewaters with zirconium phosphate based materials: efficient systems for the removal of heavy metal and dye water pollutants. *Molecules*, 26(8), pp.2392.

Qiu, J., Li, M., Yang, L. and Yao, J., 2019. Facile construction of three-dimensional netted ZnIn_2S_4 by cellulose nanofibrils for efficiently photocatalytic reduction of Cr(VI). *Chemical Engineering Journal*, 375, pp.121990.

RanguMagar, A.B., Chhetri, B.P., Parnell, C.M., Parameswaran-Thankam, A., Watanabe, F., Mustafa, T., Biris, A.S. and Ghosh, A., 2019. Removal of nitrophenols from water using cellulose derived nitrogen doped graphitic carbon material containing titanium dioxide. *Particulate Science and Technology*, 37(4), pp.440–448.

Rasheed, M., Jawaid, M., Karim, Z. and Abdullah, L.C., 2020. Morphological, physiochemical and thermal properties of microcrystalline cellulose (MCC) extracted from bamboo fiber. *Molecules*, 25(12), pp.2824.

Rubio, N.R., Xiang, N. and Kaplan, D.L., 2020. Plant-based and cell-based approaches to meat production. *Nature Communications*, 11, pp.1–12.

Saravanan, R., Gracia, F. and Stephen, A., 2017. *Basic principles, mechanism, and challenges of photocatalysis*. Berlin: Springer.

Serna-Loaiza, S., Zikeli, F., Adamcyk, J. and Friedl, A., 2021. Towards a wheat straw biorefinery: Combination of organosolv and liquid hot water for the improved production of sugars from hemicellulose and lignin hydrolysis. *Bioresource Technology Reports*, 14, pp.100667.

Shaikh, H.M., Anis, A., Poulouse, A.M., Al-Zahrani, S.M., Madhar, N.A., Alhamidi, A. and Alam, M.A., 2021. Isolation and characterization of alpha and nanocrystalline cellulose from date palm (*Phoenix dactylifera* L.) trunk mesh. *Polymers*, 13(11), pp.1893.

Sharma, H.K., Xu, C. and Qin, W., 2017. Biological pretreatment of lignocellulosic biomass for biofuels and bioproducts: an overview. *Waste and Biomass Valorization*, 10(2), pp.235–251.

- Sharma, V., Nargotra, P. and Bajaj, B.K., 2019. Ultrasound and surfactant assisted ionic liquid pretreatment of sugarcane bagasse for enhancing saccharification using enzymes from an ionic liquid tolerant *Aspergillus assiutensis* VS34. *Bioresource Technology*, 285, pp.121319.
- Shen, D., Liu, J., Gan, L., Huang, N. and Long, M., 2018. Green synthesis of Fe₃O₄/cellulose/polyvinyl alcohol hybride aerogel and its application for dye removal. *Journal of Polymers and the Environment*, 26(6), pp.2234–2242.
- Shuai, L. and Luterbacher, J., 2016. Organic solvent effects in biomass conversion reactions. *ChemSusChem*, 9(2), pp.133–155.
- Sikora, E., Katona, K.K., Muránszky, G., Bánhidi, O., Kristály, F., Szabó, J.T., Windisch, M., Fiser, B. and Vanyorek, L., 2021. Cellulose-based catalyst design for efficient chlorate reduction. *Arabian Journal of Chemistry*, 14(7), pp.103202.
- Silva, J.P., Ticona, A.R.P., Hamann, P.R. V and Quirino, B.F., 2021. Deconstruction of lignin: from enzymes to microorganisms. *Molecules*, 26, pp.2299.
- Smith, A., 2021. Plant synthesis: getting to the (plant-based) meat of the matter. *Natural Foods Merchandiser*, 42 (2), pp.10-14.
- Snyder, H., 2019. Literature review as a research methodology: An overview and guidelines. *Journal of Business Research*, 104, pp.333–339.
- Sousa, É., Rocha, L., Jaria, G., Gil, M. V., Otero, M., Esteves, V.I. and Calisto, V., 2021. Optimizing microwave-assisted production of waste-based activated carbons for the removal of antibiotics from water. *Science of the Total Environment*, 752, pp.141662.
- Steinbach, D., Wüst, D., Zielonka, S., Krümpel, J., Munder, S., Pagel, M. and Kruse, A., 2019. Steam explosion conditions highly influence the biogas yield of rice straw. *Molecules*, 24(19), pp.1–15.
- Sukyai, P., Anongjanya, P., Bunyahwuthakul, N., Kongsin, K., Harnkarnsujarit, N., Sukatta, U., Sothornvit, R. and Chollakup, R., 2018. Effect of cellulose nanocrystals from sugarcane bagasse on whey protein isolate-based films. *Food Research International*, 107, pp.528–535.
- Tahazadeh, S., Mohammadi, T., Tofighy, M.A., Khanlari, S., Karimi, H. and Motejadded Emrooz, H.B., 2021. Development of cellulose acetate/metal-organic framework derived porous carbon adsorptive membrane for dye removal applications. *Journal of Membrane Science*, 638(7), pp.119692.
- Tanaka, A., Teramura, K., Hosokawa, S., Kominami, H. and Tanaka, T., 2017. Visible light-induced water splitting in an aqueous suspension of a plasmonic Au/TiO₂ photocatalyst with metal co-catalysts. *Chemical Science*, 8(4), pp.2574–2580.

- Thanaraj, C., Priya Dharsini, G.R., Ananthan, N. and Velladurai, R., 2019. Facile route for the synthesis and cytotoxic effect of 2-amino-4H-benzo[b]pyran derivatives in aqueous media using copper oxide nanoparticles decorated on cellulose nanocrystals as heterogeneous catalyst. *Inorganic and Nano-Metal Chemistry*, 49(9), pp.313–321.
- Tavker, N. and Sharma, M., 2020. Fruit rinds extracted cellulose and its utility in fabricating visible light tin sulfide photocatalyst for the treatment of dye, pharmaceutical and textile effluents. *Journal of Cleaner Production*, 271, pp.122510.
- Tavker, N., Gaur, U.K. and Sharma, M., 2020. Agro-waste extracted cellulose supported silver phosphate nanostructures as a green photocatalyst for improved photodegradation of RhB dye and industrial fertilizer effluents. *Nanoscale Advances*, 2(7), pp.2870–2884.
- Tsapekos, P., Kougias, P.G., Egelund, H., Larsen, U., Pedersen, J., Trénel, P. and Angelidaki, I., 2017. Mechanical pretreatment at harvesting increases the bioenergy output from marginal land grasses. *Renewable Energy*, 111, pp.914–921.
- Tsegaye, B., Balomajumder, C. and Roy, P., 2019. Microbial delignification and hydrolysis of lignocellulosic biomass to enhance biofuel production: an overview and future prospect. *Bulletin of the National Research Centre*, 43(1), pp.1–16.
- Tupciauskas, R., Rizhikovs, J., Brazdauskas, P., Fridrihsone, V. and Andzs, M., 2021. Influence of steam explosion pre-treatment conditions on binder-less boards from hemp shives and wheat straw. *Industrial Crops and Products*, 170, pp.113717.
- United Nations Educational, Scientific and Cultural Organization (UNESCO), 2017. *Wastewater - the untapped resource. the United Nations world water development report 2017*. [online] Available at: <<https://unesdoc.unesco.org/ark:/48223/pf0000247553/PDF/247553eng.pdf.multi>> [Accessed 14 June 2021].
- World Health Organisation (WHO), 2019. *Drinking water*. [online] Available at: <<https://www.who.int/news-room/fact-sheets/detail/drinking-water>> [Accessed 14 June 2021].
- Wu, H., Zhou, Z., Yang, Y. and Meng, Q., 2020. Effect of steam explosion of oil palm frond and empty fruit bunch on nutrient composition and ruminal fermentation characteristics. *Tropical Animal Health and Production*, 52(3), pp.1223–1228.
- Xiong, Q., Bai, Q., Li, C., He, Y., Shen, Y. and Uyama, H., 2018. A cellulose acetate/ *Amygdalus pedunculata* shell-derived activated carbon composite monolith for phenol adsorption. *RSC Advances*, 8(14), pp.7599–7605.
- Yang, H., Zhu, Y., Jin, Y., Lei, F., Shi, Z. and Yang, J., 2021. Pseudo-lignin retarded bioconversion of sugarcane bagasse holocellulose after liquid hot water and acid. *BioResources*, 16(2), pp.4052–4063.

Yılmaz, Ş., Zengin, A. and Şahan, T., 2021. Effective utilization of Fe(III)-based metal organic framework-coated cellulose paper for highly efficient elimination from the liquid phase of paracetamol as a pharmaceutical pollutant. *Environmental Technology and Innovation*, 24, pp.101799.

Yu, F., Wan, N., Zheng, Q., Li, Y.H., Yang, M. and Wu, Z.F., 2020. Effects of ultrasound and microwave pretreatments on hydrodistillation extraction of essential oils from Kumquat peel. *Food Science & Nutrition*, 9(5), pp.2372-2380.

Yu, Y., Jin, T.Z. and Xiao, G., 2017. Effects of pulsed electric fields pretreatment and drying method on drying characteristics and nutritive quality of blueberries. *Journal of Food Processing and Preservation*, 41(6), pp.1-10.

ZabihiSahebi, A., Koushkbaghi, S., Pishnamazi, M., Askari, A., Khosravi, R. and Irani, M., 2019. Synthesis of cellulose acetate/chitosan/SWCNT/Fe₃O₄/TiO₂ composite nanofibers for the removal of Cr(VI), As(V), methylene blue and congo red from aqueous solutions. *International Journal of Biological Macromolecules*, 140, pp.1296–1304.

Zare, E. and Rafiee, Z., 2020. Cellulose stabilized Fe₃O₄ and carboxylate-imidazole and Co-based MOF growth as an exceptional catalyst for the Knoevenagel reaction. *Applied Organometallic Chemistry*, 34(4), pp.1–10.

Zeng, Z.K., Jang, J.C., Shurson, G.C., Thakral, S. and Urriola, P.E., 2021. Ammonia fiber expansion increases in vitro digestibility and fermentability of corn distillers dried grains with solubles with or without carbohydrases. *Animal Feed Science and Technology*, 273, pp.114824.

Zhang, D., Cong, T., Xia, L. and Pan, L., 2019. Growth of black TiO₂ nanowire/carbon fiber composites with dendritic structure for efficient visible-light-driven photocatalytic degradation of methylene blue. *Journal of Materials Science*, 54(10), pp.7576–7588.

Zhang, D., Zhang, G., Wang, Q. and Zhang, L., 2017. Dual-functional catalytic materials: magnetically hollow porous Ni-manganese oxides microspheres/cotton cellulose fiber. *Journal of the Taiwan Institute of Chemical Engineers*, 77, pp.311–320.

Zhang, H.D., Fan, M.S., Li, X., Zhang, A.P. and Xie, J., 2018. Enhancing enzymatic hydrolysis of sugarcane bagasse by ferric chloride catalyzed organosolv pretreatment and Tween 80. *Bioresource Technology*, 258, pp.295-301.

Zhang, X., Liu, P., Duan, Y., Jiang, M. and Zhang, J., 2017. Graphene/cellulose nanocrystals hybrid aerogel with tunable mechanical strength and hydrophilicity fabricated by ambient pressure drying technique. *RSC Advances*, 7(27), pp.16467–16473.

Zhang, Y., Lei, H., Yang, Z., Qian, K. and Villota, E., 2018. Renewable high-purity mono-phenol production from catalytic microwave-induced pyrolysis of cellulose over biomass-derived activated carbon catalyst. *ACS Sustainable Chemistry and Engineering*, 6(4), pp.5349–5357.

Zhang, Y., Zhou, Z., Yuan, K., Wen, F., Tan, J., Hu, C. and Wang, H., 2017. Fabrication of a modified straw cellulose and cerium oxide nanocomposite and its visible-light photocatalytic reduction activity. *Journal of Environmental Chemical Engineering*, 5(4), pp.3734–3740.

Zhang, Z., Nie, M., Xiao, Y., Zhu, L., Gao, R., Zhou, C., Li, D., Xu, Y. and Dai, Z., 2021. Positive effects of ultrasound pretreatment on the bioaccessibility and cellular uptake of bioactive compounds from broccoli: Effect on cell wall, cellular matrix and digesta. *Lwt – Food Science and Technology*, 149, pp.112052.

Zhu, G., Xing, X., Wang, J. and Zhang, X., 2017. Effect of acid and hydrothermal treatments on the dye adsorption properties of biomass-derived activated carbon. *Journal of Materials Science*, 52(13), pp.7664–7676.

Zianor Azrina, Z.A., Beg, M.D.H., Rosli, M.Y., Ramli, R., Junadi, N. and Alam, A.K.M.M., 2017. Spherical nanocrystalline cellulose (NCC) from oil palm empty fruit bunch pulp via ultrasound assisted hydrolysis. *Carbohydrate Polymers*, 162, pp.115–120.

Zik, N.A.F.A., Sulaiman, S. and Jamal, P., 2020. Biodiesel production from waste cooking oil using calcium oxide/nanocrystal cellulose/polyvinyl alcohol catalyst in a packed bed reactor. *Renewable Energy*, 155, pp.267–277.

Zirak, M., Abdollahiyan, A., Eftekhari-Sis, B. and Saraei, M., 2018. Carboxymethyl cellulose coated $\text{Fe}_3\text{O}_4@ \text{SiO}_2$ core-shell magnetic nanoparticles for methylene blue removal: equilibrium, kinetic, and thermodynamic studies. *Cellulose*, 25(1), pp.503–515.

Zou, Z., Yang, X., Zhang, P., Zhang, Y., Yan, X., Zhou, R., Liu, D., Xu, L. and Gui, J., 2019. Trace carbon-hybridized ZnS/ZnO hollow nanospheres with multi-enhanced visible-light photocatalytic performance. *Journal of Alloys and Compounds*, 775, pp.481–489.